DISS. ETH NO. 24966

ARCHITECTED CORE-SHELL BEAMS FOR STIFF, STRONG, AND TOUGH CELLULAR STRUCTURES

A dissertation submitted to attain the degree of

DOCTOR OF SCIENCES of ETH ZURICH
(Dr. sc. ETH Zurich)

presented by

JOCHEN MUELLER

M.Sc. Imperial College London
B.Eng. Albstadt-Sigmaringen University

born on April 24, 1987
citizen of Germany

accepted on the recommendation of

Prof. Dr. Kristina A. Shea, examiner
Prof. Dr. Jennifer A. Lewis, co-examiner
Prof. Dr. Dennis M. Kochmann, co-examiner
Prof. Dr. Ralph Spolenak, co-examiner

2018

Jochen Mueller: *Architected Core-Shell Beams for Stiff, Strong, and Tough Cellular Structures,* © 2018

ABSTRACT

Despite recent advances in fabrication technologies, the ability to create stiff and strong lightweight structures that are also tough remains an elusive goal, as these properties are typically mutually exclusive. Nature overcomes these limitations by combining complex mechanisms that span across multiple length scales. However, synthetic replications of these structures are confined to specific geometries, highly anisotropic, or limited in build volume.

Taking inspiration from nature, this thesis takes an alternative approach to the design of cellular structures that are lightweight and simultaneously possess high stiffness, strength, and toughness. Conventionally, the best compromise between these properties is found by varying the unit cell type and material. Here, the focus is on the intermediate hierarchy level – the struts. Specifically, three architectural design principles are introduced and evaluated.

Strain in a bending beam or strut increases from the neutral axis to the outside. As a result, when the failure strain is reached, the material is not fully strained on the inside and hence inefficiently used. Principle I replaces the core with layers of more brittle materials tuned to local strains. Due to the mutual exclusivity, these materials possess higher stiffness and strength, maximizing the effective toughness without reducing the maximum deflection.

The stiffness of a strut exhibits a strong power law dependence on the diameter. Consequently, the core has little effect and hollow struts are commonly used as they perform better relative to the density. However, similar failure strains apply in these typically brittle structures. Principle II replaces the core with a flexible material that continues to provide toughness when the shell fails. To overcome fabrication constraints, a printhead is developed for the direct ink writing process that enables fabrication of multicore-shell struts from arbitrary materials.

When the fracture strain in a conventional strut is reached, a crack forms and propagates through the strut. Due to stress concentration, the bulk of the material is only strained locally with minimal contribution to the toughness. Principle III prevents crack propagation by adding radial interfacial layers. This allows each layer to fail when its own failure strain is

reached, rather than when the outermost layer fails. Consequently, the inner layers fail later and the effective failure strain and toughness are increased.

The design principles differ fundamentally in the mechanism, efficiency, and application. Increases in toughness ranging from 50% to 4000% are found with no negative effects on the stiffness, strength, and failure strains. The principles are complementary to existing approaches, scale-independent, and extendible to geometries other than struts. As a result, they can have a substantial effect on the safety, cost, and environmental impact in volume and weight restricted applications, such as aircrafts, helmets or packaging.

ZUSAMMENFASSUNG

Trotz kontinuierlicher Fortschritte in der Entwicklung von neuartigen Fertigungstechnologien ist es noch immer nahezu unmöglich, steife, feste und gleichzeitig widerstandsfähige Leichtbaustrukturen herzustellen, da sich diese strukturellen Eigenschaften meist gegenseitig ausschließen. In der Natur werden diese Einschränkungen überwunden, indem komplexe Topologien und Mechanismen kombiniert werden, die sich über mehrere Größenordnungen erstrecken. Künstliche Nachbildungen sind jedoch auf wenige bestimmte Formen begrenzt, stark anisotrop oder auf kleine Bauvolumen beschränkt.

Inspiriert von Strukturen aus der Natur verfolgt die vorliegende Arbeit einen alternativen Ansatz um Gitterstrukturen zu entwickeln, die leicht sind und dabei gleichzeitig eine hohe Steifigkeit, Festigkeit und Widerstandsfähigkeit aufweisen. Bisher wird dabei ein Kompromiss zwischen diesen Eigenschaften erreicht, indem der Typ der Einheitszelle und das Material selbst variiert werden. In dieser Arbeit liegt der Fokus auf der Hierarchieebene dazwischen - den Streben. Dabei werden drei architektonische Konstruktionsparadigmen vorgestellt und untersucht.

In einem Biegebalken oder einer Strebe nehmen die Dehnungen von der neutralen Achse nach außen hin zu. Dementsprechend wird das Material bei Erreichen der Bruchdehnung im Inneren nicht vollständig gedehnt und daher nicht effizient genutzt. Paradigma I ersetzt den Kern durch Schichten spröderer Materialien, die für die lokalen Dehnungen optimiert sind. Aufgrund der Gegensätzlichkeit der jeweiligen Materialeigenschaften weisen diese Strukturen eine höhere Steifigkeit und Festigkeit auf, wodurch die effektive Widerstandsfähigkeit insgesamt maximiert wird, ohne dabei die maximale Durchbiegung zu reduzieren.

Die Steifigkeit einer Strebe erhöht sich quartisch mit dem Durchmesser, weshalb der Kern nur einen geringen Einfluss hat. In der Praxis werden deshalb oft Hohlstreben eingesetzt, welche jedoch ähnlich niedrige Bruchdehnungen wie volle Streben haben. Paradigma II ersetzt den Kern einer Strebe durch ein flexibles Material, das auch nach einem Versagen der Schale noch eine gewisse Widerstandsfähigkeit der Gesamtstruktur garantiert. Um trotz der

Einschränkungen momentaner Fertigungsverfahren die Herstellung dieser mehrkernigen Streben aus beliebigen Materialien zu ermöglichen, wird als ein zusätzlicher Teil der Arbeit ein Druckkopf für den Direct Ink Writing Prozess entwickelt.

Wenn die Bruchdehnung des Materials in einer homogenen Strebe erreicht wird, bildet sich ein Riss, der sich ausbreitet bis die Strebe bricht. Aufgrund von Spannungskonzentrationen wird ein Großteil des Materials im Inneren nur lokal belastet. Dieser Materialanteil hat deshalb, global betrachtet, nur einen geringen Einfluss auf die Widerstandsfähigkeit der Struktur, jedoch dieselbe Dichte wie das vollständig gedehnte Material. Paradigma III trennt den Stab in verschiedene Lagen, die die Rissausbreitung verhindern. Dies ermöglicht, dass jede Lage erst dann versagt, wenn ihre eigene Bruchdehnung erreicht wird und nicht, wenn die maximale Bruchdehnung in der äußersten Lage erreicht ist. Dementsprechend versagen die inneren Lagen später, sodass die effektive Bruchdehnung und damit Widerstandsfähigkeit der Gesamtstruktur erhöht wird.

Die vorgestellten Konstruktionsparadigmen unterscheiden sich grundlegend in ihrer jeweiligen Wirkungsweise, Effizienz und Anwendung. Es wurden Anstiege in der Widerstandsfähigkeit im Bereich von 50% bis 4000% gefunden, ohne dass negative Auswirkungen auf die Steifheit, Festigkeit und Bruchdehnung festgestellt werden konnten. Die Paradigmen sind komplementär zu bestehenden Ansätzen, unabhängig von der Baugröße und erweiterbar auf andere Geometrien. Dies kann erhebliche Auswirkungen auf die Sicherheit, Kosten und Umweltauswirkungen in Strukturen mit begrenztem Volumen und Gewicht haben, zum Beispiel in Fahrzeugen, Helmen oder Verpackungen.

ACKNOWLEDGEMENTS

I would like to express my sincere gratitude to all of those who have supported me in one way or another and thereby contributed to the accomplishments reported herein.

I am deeply grateful to my doctoral advisor, Prof. Kristina Shea, who gave me the opportunity to pursue this dream and for providing an optimized environment to follow my ideas, develop a better, scientific understanding, and for giving me the chance to thrive in something I never considered work.

The same gratitude goes to Prof. Jennifer Lewis, who accommodated me in her lab and is far more than just a scientific advisor, collaborator, and co-examiner. The opportunity to work with and learn from her has been an inspiration and invaluable on so many ends.

Thank you to my collaborators and committee members, Prof. Dennis Kochmann and Prof. Ralph Spolenak, whose talent and personalities I deeply admire. Both contributed substantially to numerous projects, directly and indirectly through everything I learned from them.

I could not be more grateful to Prof. Jordan Raney, who is simply a wonderful collaborator and friend, and who sparked the idea of the core-shell approach that turned out to be the core (and the shell) of this work.

Thank you to Prof. Paolo Ermanni, who introduced me to ETH Zurich and continued supporting me by sharing his labs and expertise. In the same breath, I want to thank Andrea Bergamini for being the best advisor one can imagine both professionally and personally. Thank you to Prof. Chiara Daraio for the guidance and support in our project and beyond. It is always an inspiration talking with you. Thank you to Prof. Kathryn Matlack for being a fantastic collaborator and source of inspiration.

I want to thank all past and present members of the Engineering Design and Computing group at ETH Zurich: Allie Blösch-Paidosh, Merel van Diepen, Paul Egan, Cosima du Pasquier, Corinna Königseder, Benjamin Kruse, Bettina Melberg, Clemens Münzer, Eugen Rigger, Martin Schütz, Jonas Schwarz, Fritz Stöckli, Jung-Chew Tse, Marius Wagner, Zhiyang Yu, Luca

Zimmermann, and, in particular, Tino Stanković, Tim Chen, and Thomas Lumpe, with whom I had the pleasure and honor to collaborate on multiple research and leisure projects.

A big thank you to the whole Lewis group at Harvard, including the current and former members Bok Yeop Ahn, John Ahrens, Dahlia Amato, Michael Bell, Nicole Black, J. William Boley, Alex Chortos, Bradley Duncan, Daniele Foresti, Sydney Gladman, Kimberly Homan, David Kolesky, Arda Kotikian, Katharina Kroll, Armand Kurum, Jack Minardi, Thomas Ober, Lori Sanders, Scott Slimmer, Ryan Truby, and Alexander Valentine. A very special thank you to Benito Román-Manso, Joseph Muth, Mark Skylar-Scott, Claas Visser, Teng-Sing Wei, and Nanjia Zhou, who are the most talented coworkers and wonderful friends. Thank you to James Weaver, who, after some poking, produces the most beautiful research images.

I would like to thank all the members of the Laboratory of Composite Materials and Adaptive Structures, with whom I continued to interact beyond my time in the group, in particular, Emian Furger, Gerald Kress, Christian Loosli, Gulio Molinari, Claudia Thurnherr, and Falk Runkel.

All this would not have been possible without the generous support from Prof. Johann Schimonyi during and past my Bachelor's. I conducted my first internship at the University of Calgary, where Prof. Simon Park sparked my interest in research. The time in (and outside) his lab was not just an incredible experience, but a major stepping stone. The very same is true for my time at Monash University, where Prof. Adrian Neild invited me to work on my Bachelor's thesis, which eventually turned into my first journal article. I also want to thank Tuncay Alan, who played a major role in this project. Without your combined support, I would not be the person I am today and I will always be grateful for that.

Thank you to Prof. Roger Fenner, who believed in me and supported my endeavors at Imperial College London. Thank you to Ambrose Taylor and Prof. Anthony Kinloch, for their intellect and input during my Master's thesis, which was the best preparation for this next step.

Most importantly, I want to express my utmost gratitude to my parents, Rolf and Vera, to my brothers, Christoph and Patrick, to my extended family and friends, and to everyone else involved, for their love and support and for all the wonderful moments we have shared.

CONTENTS

1 INTRODUCTION 1

1.1 Background and problem statement . . . 1

1.2 Scope of the thesis . . . 11

1.2.1 Core-shell type I: brittle core, flexible shell . . . 12

1.2.2 Core-shell type II: flexible core, brittle shell . . . 13

1.2.3 Core-shell type III: brittle core, brittle shell . . . 14

1.2.4 Research objectives . . . 15

1.3 Thesis outline . . . 16

1.4 Summary . . . 18

2 INTERFACES AND MULTI-MATERIAL MIXING IN MATERIAL JETTING 19

2.1 Introduction . . . 19

2.2 Methods . . . 21

2.2.1 Sample fabrication and preparation . . . 22

2.2.2 Light microscopy and nanoindentation . . . 23

2.3 Results . . . 24

2.3.1 Single-material interfaces . . . 24

2.3.2 Material mixing . . . 26

2.3.3 Multi-material interfaces . . . 27

2.4 Discussion . . . 29

2.4.1 Single-material interfaces . . . 29

2.4.2 Material mixing . . . 31

2.4.3 Multi-material interfaces . . . 32

2.5 Conclusions . . . 32

2.6 Summary . . . 33

3 CORE-SHELL TYPE I: BRITTLE CORE, FLEXIBLE SHELL 35

3.1 Introduction . . . 35

3.2 Methods . . . 38

3.2.1 Model . . . 38

3.2.2 Materials . . . 41
3.2.3 Fabrication . . . 42
3.2.4 Characterization . . . 42
3.3 Results . . . 43
3.3.1 Individual struts . . . 43
3.3.2 Unit cells . . . 47
3.3.3 Lattice structures . . . 47
3.4 Discussion . . . 50
3.4.1 Individual struts . . . 50
3.4.2 Unit cells and lattice structures . . . 51
3.5 Conclusions . . . 51
3.6 Summary . . . 52

4 CORE-SHELL TYPE II: FLEXIBLE CORE, BRITTLE SHELL 53
4.1 Introduction . . . 53
4.2 Methods . . . 57
4.2.1 Materials . . . 58
4.2.2 Fabrication of multicore-shell printheads . . . 60
4.2.3 Multicore–shell 3D printing . . . 61
4.2.4 Characterization . . . 61
4.3 Results . . . 62
4.3.1 Material optimization . . . 62
4.3.2 Individual struts . . . 63
4.3.3 Lattice structures . . . 67
4.4 Discussion . . . 68
4.4.1 Multicore-shell printhead design and fabrication . . . 69
4.4.2 Material optimization . . . 71
4.4.3 Individual struts . . . 71
4.4.4 Lattice structures . . . 72
4.5 Conclusions . . . 73
4.6 Summary . . . 73

5 CORE-SHELL TYPE III: BRITTLE CORE, BRITTLE SHELL 75
5.1 Introduction . . . 75
5.2 Methods . . . 78

5.2.1 Optimization . . . 80
5.2.2 Characterization . . . 82
5.3 Results . . . 82
5.3.1 Experimental validation of the model . . . 82
5.3.2 Effect of core-to-shell ratio, number of gaps, and gap width . . . 85
5.3.3 Effect of material . . . 86
5.4 Discussion . . . 89
5.4.1 Experimental validation of the model . . . 89
5.4.2 Effect of core-to-shell ratio, number of gaps, and gap width . . . 90
5.4.3 Effect of material . . . 92
5.5 Conclusions . . . 92
5.6 Summary . . . 93

6 DESIGN GUIDELINES FOR CORE-SHELL STRUCTURES 95
6.1 Characteristics and applications in comparison . . . 95
6.1.1 Core-shell type I: brittle core, flexible shell . . . 95
6.1.2 Core-shell type II: flexible core, brittle shell . . . 97
6.1.3 Core-shell type III: brittle core, brittle shell . . . 98
6.1.4 Conclusions for designers, engineers, and scientists . . . 99
6.2 Combination of different mechanisms . . . 99
6.3 Relative performance compared to literature . . . 102
6.4 Summary . . . 104

7 CONCLUSIONS AND OUTLOOK 105
7.1 Principal findings and contributions . . . 105
7.2 Challenges and opportunities . . . 108
7.2.1 Nodal effects . . . 108
7.2.2 Increasing the material space . . . 108
7.2.3 Interactions between struts, unit cells, and lattices . . . 110
7.2.4 Moving beyond mechanical properties . . . 111
7.3 Summary and conclusions . . . 112

BIBLIOGRAPHY 113

1

INTRODUCTION

Überall geht ein frühes Ahnen dem späteren Wissen voraus.

— Alexander von Humboldt

Stiffness, strength, toughness, and density are material properties that are critical for the performance of numerous engineering structures, such as bicycle helmets and packaging material. Due to their intrinsic nature, these properties are often mutually exclusive, making it virtually impossible to design and, in particular, fabricate materials or structures with these properties. This chapter introduces applications, elaborates the fundamental challenges, and reviews the state of the art as a precursor for the development of solutions that overcome the limitations. It will then define and outline how the problem is approached, with the goal to significantly advance the field of energy absorbing lightweight structures.

1.1 BACKGROUND AND PROBLEM STATEMENT

When a structure is subject to load, the resulting deformations cause strain energy to be stored. The total strain energy a material can store prior to rupture is the toughness, often referred to as energy absorption or modulus of toughness [1, 2]. It is important to differentiate between toughness and fracture toughness, which is the ability of a material to resist fracture [3–6].

In engineering materials, toughness is one of the most important material properties [7] and required in numerous applications [8, 9]. In particular, vehicles are a common example. Automotive engineers use energy-absorbing structures to improve the crashworthiness and hence safety in numerous parts of cars and affected counterparts, such as W-beam guide rail systems on highways [8]. In agriculture, construction, and mining, FOPS (falling object protective structures) and ROPS (roll-over protective structures) are two important concepts, as these machines typically work in hazardous environments or on sloped grounds [8]. Another important area is that of personal safety and protective devices. All types of helmets, such

as bicycle, football, and skiing helmets, hard hats, and bullet-proof jackets are required to possess the ability to absorb a sufficient amount of energy [8]. In addition to personal safety, packaging is essential to preserve and distribute goods during storage and transportation by protecting it from external damage.

Simplified, a tough material needs to simultaneously exhibit high stiffness, strength, and failure strain, as these properties determine the area under the load-displacement or stress-strain curve, which is equivalent to the toughness. Stiffness is a function of the material modulus and geometric shape, and determines the slope of the curve. Strength, which is the maximum stress a material can withstand before irrecoverable deformation or rupture, determines the height of the curve. The failure strain refers to the strain that experiences some sort of failure, such as the begin of plastic deformation. When the failure strain causes a rupture, it is also referred to as fracture strain. Stiffness and strength relate approximately linearly, indicating that some of the stiffest materials are also the strongest (Figure 1.1).

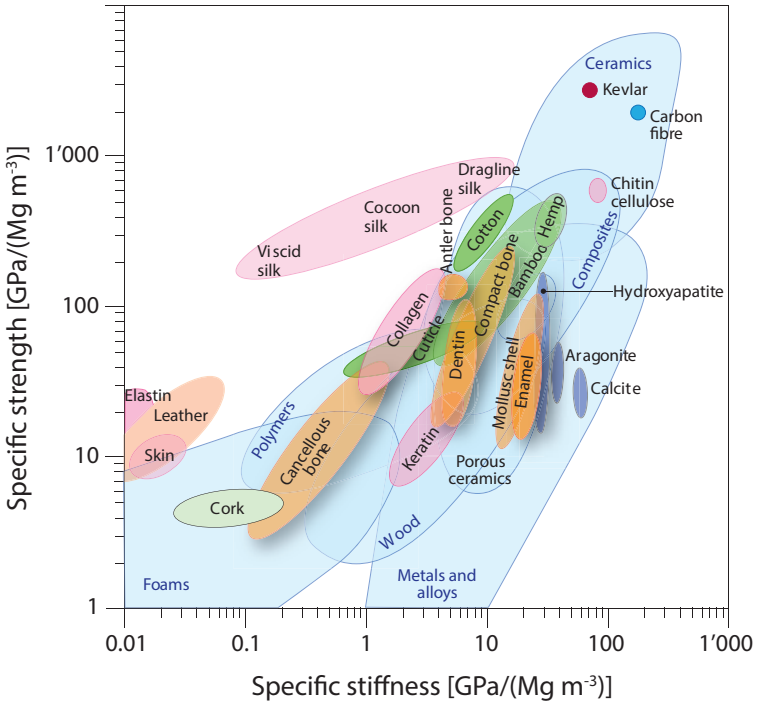

FIGURE 1.1: Relationship between specific strength and specific stiffness for different materials classes. With few exceptions, the properties scale linearly. Relatively weak classes, such as polymers, are typically also weaker, and strong materials, such as ceramics, also possess high stiffness. Figure adapted from [10].

However, stiffness or strength and failure strain, therefore toughness, are often mutually exclusive, making it hard to find stiff or strong and tough materials [6, 11–15]. In steel, this phenomenon is known as the strength–ductility trade-off [16–18]. For example, carbon steel

has the same modulus at different carbon contents [19]. At the same time, the carbon content has a strong effect on both the strength and failure strain in that high carbon content increases strength, but decreases failure strain, and vice versa [20]. The toughest carbon steel is fabricated with a medium amount of carbon [21]. The development of tough materials has therefore been an exercise in compromise between stiffness, strength, and failure strain [12, 22].

Nature found ways to overcome these limitations by a combination of mechanisms operating at different length scales [6, 23, 24]. The list of examples includes teeth [25, 26], horse hooves [27], corals [28], sea sponge skeletons [29, 30], sea urchin spines [28], feathers [31], shark skin [32], porcupine quills [33], and bird break interior [28]. One of the most prominent examples for stiff, strong, and tough structures is bone [34, 35].

Bone has a hierarchical structure of seven layers that spans over nine orders of magnitude (Figure 1.2) [36]. At the macro-scale, two types of bone exist: foam-like (cancellous) bone with strut sizes of the order of 100 μm, typically found at the inside of the bone, and compact (cortical) bone, found at the surface. Compact bone, which is structurally stronger, consists of osteons – cylindrical structures of 0.2 mm in diameter and several millimeters in length. Osteons are composed of radially aligned lamellae. Each lamella contains layers of fibers at the scale of 50 μm with alternating alignments. The fibers are an array of collagen fibrils at the scale of 10 μm, linked with an organic phase acting as an adhesive. Each fibril array is composed of mineralized collagen fibrils in the order of 1 μm. Collagen has a size of about 300 nm and is composed of amino acids in the order of 1 nm [12, 14].

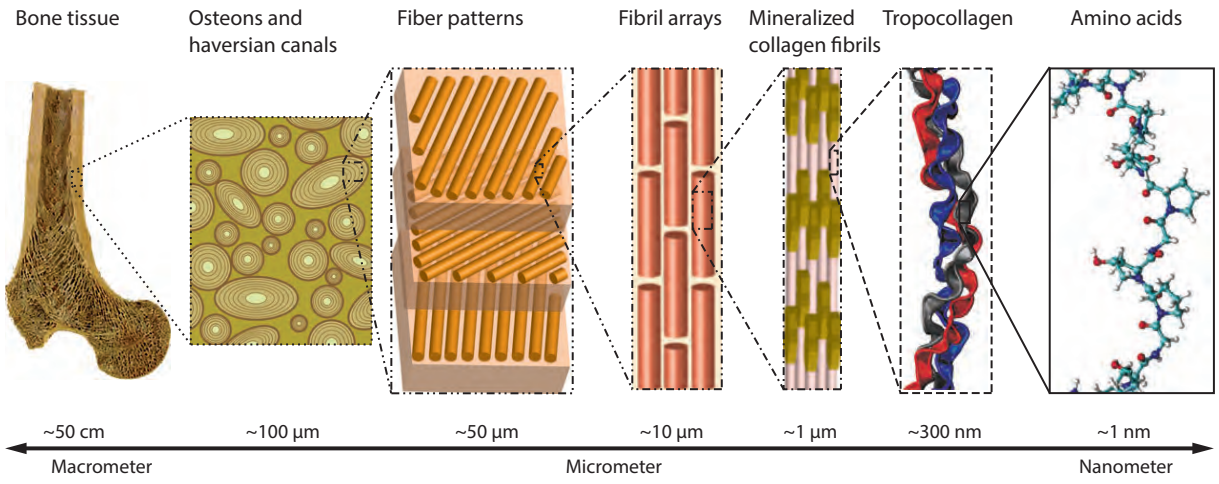

FIGURE 1.2: Hierarchies in foam-like (cancellous) bone spanning seven orders of magnitude, ranging from the macro-scale, to the micro-scale, to the nano-scale. Figure adapted from [14].

At small length scales, i.e. below 1 μm, plastic deformation, also referred to as intrinsic toughening [12], dominates the toughening mechanisms. Intrinsic mechanisms occur ahead of the crack tip and involve molecular uncoiling, fibrillar sliding and microcracking. Due to hardening of cortical bone with age, these effects become decreasingly effective [37]. Above 1 μm, extrinsic toughening, i.e. toughening behind the crack tip, prevails [12]. Breaking of sacrificial bonds, collagen-fibril bridging, uncracked ligament bridging, crack deflection, and crack bridging are the main mechanisms and act independently of age [12, 14]. Due to complexity and interaction effects between different mechanisms, replicating these properties in synthetic materials has proven difficult. To date, only individual features were replicated successfully.

In particular, the adaption of fibril or fiber reinforcement has been successful in, for example, reinforced concrete [38] and fiber-reinforced plastic (FRP) [39]. In both examples, a strong or ductile material is incorporated in a stiff material matrix, often in the shape of fibers [39, 40]. The resulting hybrid material maintains most of its stiffness, but significantly gains in strength or toughness [38, 39, 41]. Numerous adaptations exist, such as FRP layered in pre-impregnated composite fiber sheets ("prepreg") of different orientations [42], which allows a high degree of automation in the processing.

Various, global mechanical properties, $\mathcal{X}$, of a hybrid material, such as the elastic modulus, mass density, strength, and electrical and thermal conductivity, can be predicted with a model based on the properties, $\mathcal{X}_i$, and fractions, ϕ_i, of the constituents, i, – the general rule of mixtures (Equation 1.1) [28, 43].

$$\mathcal{X} = \sum \phi_i X_i. \tag{1.1}$$

The rule of mixtures is state of the art in fiber-reinforced polymer composites and confirms the mutual exclusivity. It also shows that the addition of fibers has great advantages, but is not sufficient to replicate the complex structure of natural examples to achieve similar, mechanical properties.

Another common example of a material with high strength and toughness is nacre. Nacre is an organic-inorganic composite material that is produced by some mollusks and forms their inner shell layer [44]. Nacre contains a brick-and-mortar structure consisting of 95 vol.% mineral aragonite platelets on the micro meter order with an organic biopolymer holding the

platelets together [45, 46]. Without the polymer, the structure would be inherently brittle with low toughness. The added polymer acts as a lubricant allowing limited movement between the plastics, introducing multiple toughening mechanisms, such as plastic deformation, micro-cracking, platelet pull-out, friction, and crack deflection [47, 48]. Similarly to bone, synthetic replication of nacre is complex. However, recent approaches have shown that the structure can be replicated with bulk ceramic materials using a freeze-casting technique that is infiltrated with polymethyl methacrylate (PMMA) [49, 50]. The resulting mechanical properties are comparable or even exceeding those of nacre (Figure 1.3) [13, 50].

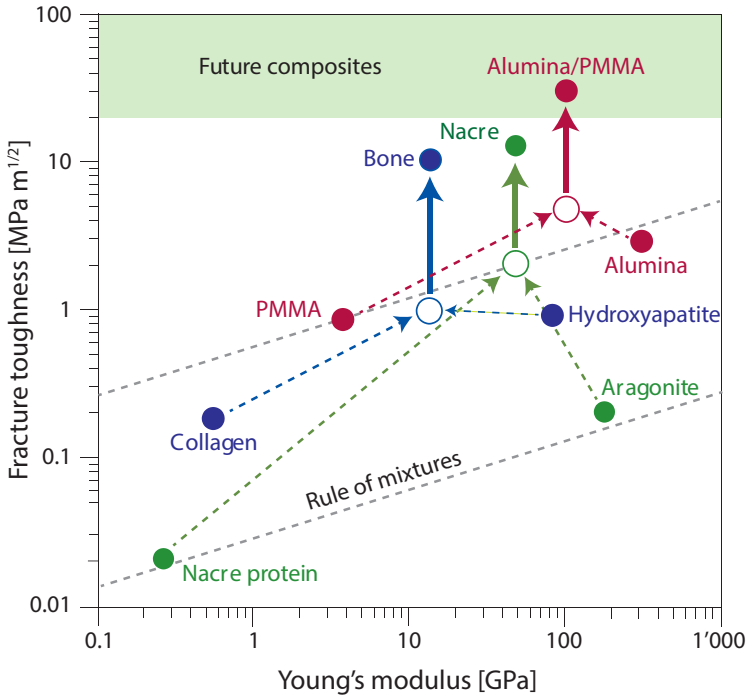

FIGURE 1.3: Relationship between fracture toughness and Young's modulus. In composite materials, it is possible to achieve an effective toughness that is higher than that of the constituents. This can be seen in nature, for example, with bone and nacre. Taking advantage of advanced fabrication methods, synthetic nacre (Alumina/PMMA) can be fabricated, which outperforms conventional nacre. Figure adapted from [10].

The example shows that it is generally possible to synthetically replicate natural materials. Interestingly, it also shows that it is possible to obtain composite properties that outperform the properties of the individual materials (Figure 1.3). This is typically only seen in biological materials, which do not always follow the rule of mixtures [28, 51, 52]. Though, with limitation to ceramic and polymer, synthetic nacre is rather specialized and the mechanism not widely applicable to other materials classes and combinations.

In addition to the mechanical properties, invariably, the volume and weight or density of a material are important in many energy absorbing structures. For example, in packaging, thinner wrapping allows transportation of more goods at the same time, decreasing cost and environmental impact [53]. Similarly, lighter vehicles consume less fuel, hence emit less carbon dioxide [54]. Reduction of weight and volume can also complement each other. For example, in race cars, lower weight enables faster acceleration and smaller volume improves the aerodynamics through reduced air drag to maximize speed [55]. It is therefore also important for a stiff, strong, and tough material to have a low density. However, density correlates linearly with the mechanical properties in that stronger materials or structures are also heavier [56–58]. This adds another variable to the already complex system and, even in nature, such materials are scarce [29].

The mutual exclusivity between these properties sets a physical limit to the available material options for the constituents. However, taking inspiration again from nature, one will almost certainly find a solution for this, too. Indeed, there are examples of lightweight materials that possess outstanding mechanical properties and multifunctionality, including the aforementioned bone [36], diatom shells [59], and sponges [29, 30].

In such structures, weight is often lowered by removing material in inefficient locations, creating pores. These materials are referred to as cellular materials or structures. Due to the reduced mass, the performance of these cellular materials is often lower than that of bulk materials. However, the rate at which the mechanical properties decrease is smaller than that of the density, which effectively increases the relative properties [57, 60]. In bone, for example, the density is much higher on the outside than it is at the inside [36]. In pure tension or compression, this does not make a big difference. In bending, however, it makes use of the second moment of area, I. The second moment of area scales $I \propto d^4$ with the diameter, d [1]. This means that a doubling of the diameter results in a second moment of area or stiffness that is 16 times higher, which greatly increases the relative stiffness.

Conventionally, cellular materials are generated stochastically and, in this form, also termed foams [61–64]. Cellular materials are ubiquitous in both nature and technology, and come in either open or closed cell configurations [57]. Applications exist for both types, such as load bearing structures, insulations [65], filters [66], and biomedical implants in tissue engineer-

ing [67]. Depending on the connectivity at the nodes, i.e. the number of connecting struts, cellular materials exhibit either bending or stretching dominated behavior [68].

Stretching dominated structures have no intrinsic mechanism that allows for bending, which leads to high stiffness and strength. They are considered more efficient in terms of density [68, 69]. The stiffness, E, and (yield) strength, σ_y, scale linearly with the relative density, $\bar{\rho}$, as $E \sim \bar{\rho}$ and $\sigma_y \sim \bar{\rho}$ [70]. Stretching dominated structures can contain a stiffness and strength ten and three times higher, respectively, when compared to bending dominated structures of the same relative density [68].

Bending dominated architectures are more attractive for energy absorption, as they provide a more favorable combination of stiffness, strength, and failure strain [68, 71]. In bending dominated structures, the stiffness scales as $E \sim \bar{\rho}^2$ for periodic cellular structures and $E \sim \bar{\rho}^3$ for stochastic cellular structures [72].

Fabrication of periodic cellular materials is often complex, especially on a small scale, as it requires a process that can arbitrarily place or remove material in a three-dimensional (3D) space [73–75]. The added control, however, allows tuning to specific requirements, which can render the materials more efficient. A typical example of a conventionally fabricated periodic, cellular material is a 2.5D honeycomb. These honeycombs are highly efficient and state of the art in various industries, such as aerospace [76, 77]. Fabrication of complex 3D lattices gained significant popularity with the advent of additive manufacturing (AM), also called 3D printing [78].

Within the regime of AM, there are numerous processes and the amount of processes increases constantly (Figure 1.4), but only certain types are capable of fabricating complex 3D lattices [78]. In particular, overhangs are a problem. In classes, such as binder jetting and powder bed fusion (e.g. selective laser sintering and selective laser melting), powder acts as model material and support at the same time [79–81]. As long as the powder can be removed post printing, as is the case in open-cell, but not in closed-cell structures, the processes can fabricate arbitrary shapes. Other classes, such as material jetting (e.g. polyjet and inkjet 3D printing), material extrusion (e.g. direct ink writing and fused deposition modeling), and vat photopolymerization (e.g. stereolithography and two-photon polymerization) require an additional support structure for overhangs above a certain angle, which needs to be removed in

a cumbersome way [82–88]. Promising efforts are undertaken by developing soluble support material [89, 90] or by curing the material on the fly, removing the need for support [91–93].

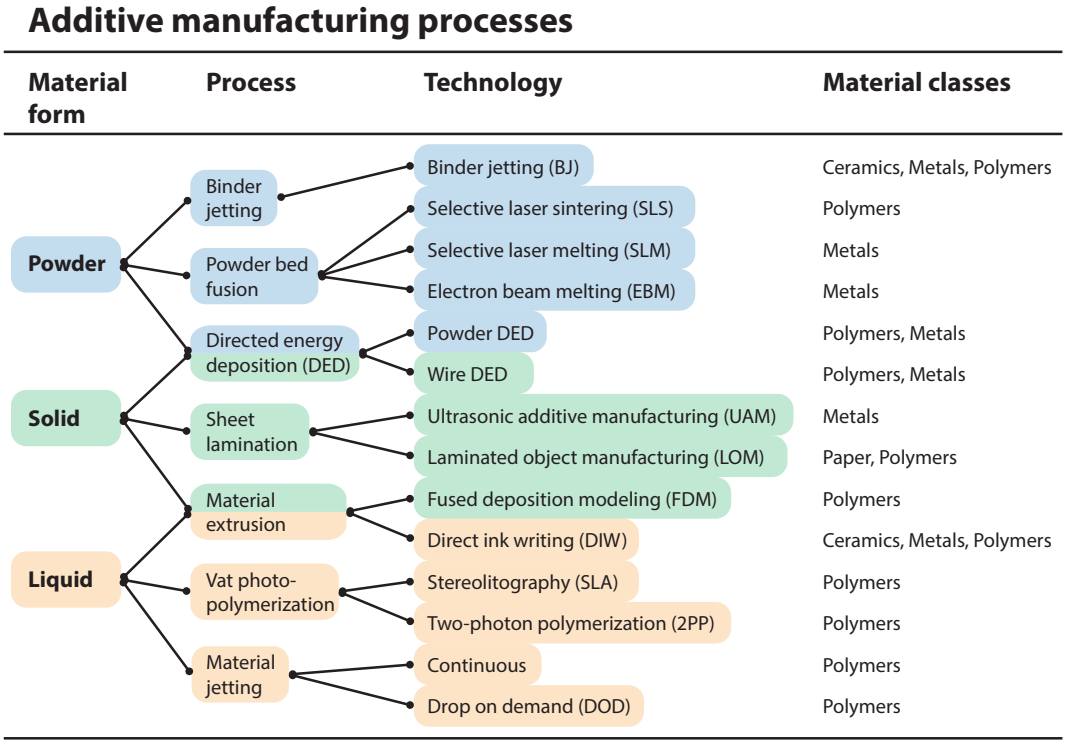

FIGURE 1.4: State of the art in additive manufacturing processes. The processes can be categorized by the material form the raw materials come in, i.e. powder, solid, or liquid. Currently, seven process categories exist according to the ASTM F2792-12a (note that the standard has been withdrawn in 2015 with no replacement). The process, technology, and material landscapes are constantly shifting as more processes and sub-processes become available. The material classes show the most common materials printed with the respective processes, but specialized processes and adaptations to print other materials may exist.

Overhangs and supports are not the only factors that determine the printability of cellular structures. Due to non-uniform curing or the inclusion of voids, almost all 3D printing processes yield structures with different degrees of anisotropy [94–98]. For complex, bioinspired 3D lattices, materials are particularly important. The methods are also limited to the specific material groups they can process, for example, thermoplastics (FDM) or photopolymers (stereolithography) [81, 82, 86]. As opposed to prototypes, this becomes an issue in engineering structures, where the absolute properties matter. Further, many processes can only print single-material structures, as often seen in the group of vat photopolymerization, or have difficulties printing multi-material structures, such as when locally replacing powder in powder bed fusion [86, 99–101]. The biggest issue, however, is scale. While it is possible to 3D print at scales ranging from nanometers to centimeters, no one individual process can span multiple orders of magnitude without significant drawbacks, such as periodicity [87, 102–106]. Please

note that this overview is by no means comprehensive and that specialized approaches exist, which address and sometimes overcome individual drawbacks mentioned herein.

When trying to fabricate a specific structure, the limitations narrow the large number of available processes down to a small number of feasible processes, if lucky. Nevertheless, existing processes already achieved staggering results and researchers are highly creative when it comes to improving methods or developing new ones, as seen by an increasing number of issued patents and publications in recent years [107].

In particular, two photon polymerization is capable of fabricating highly complex lattice geometries that exhibit outstanding mechanical properties [108]. These properties are mainly enabled through the strut architecture, where the density of the struts increases from the inside to the outside, often resulting in hollow cores. In combination with high strength materials, such as nano ceramics [109–111] and nano composites [112], these structures can possess high stiffness and strength, but still suffer from brittle, catastrophic failure [109, 113]. At nanoscale, scale effects can add flaw tolerance [114, 115] and ductility [116, 117], but efforts to toughen brittle base materials by using composites [13, 118] or micro structural features to impede crack motion [119] have seen limited success [113]. Other processes, such as direct ink writing [83], support a wider range of materials, but are limited in geometric complexity [91, 120].

In summary, it has been shown that it is possible to fabricate materials with outstanding mechanical properties using specialized processes, often inspired by biological materials. These synthetic materials (partially) overcome the mutual exclusivity of different mechanical properties, such as strength and toughness. In addition, these materials can significantly outperform their constituents. Further, it has been described that complex geometries can be created through 3D printing, which is important when considering the lightweight aspect. With this, many individual pieces of the puzzle are solved. However, a combination of existing materials with current approaches, to complete the puzzle, is often neither possible nor meaningful in a structural sense. For example, synthetic nacre cannot be 3D printed, but even if it could, its anisotropy would not match that required by lattice struts (Figure 1.5).

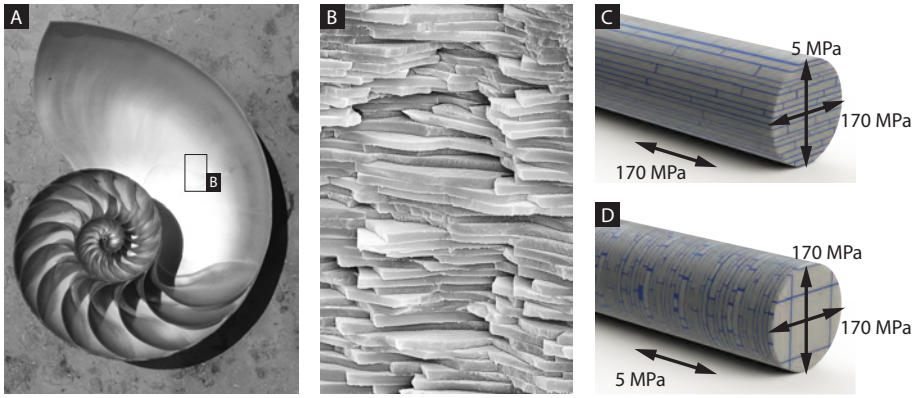

FIGURE 1.5: (a) Nacre inside a nautilus shell. Image credit: Wikipedia. (b) Scanning electron microscope image of a fractured nacre surface from a pearl oyster (pinctada). Image credit: Antony Tomsia. (c) A strut formed from synthetic nacre provides high strength along the strut. The asymmetrical alignment in the cross section suggests that the mechanical properties vary around different bending axes. (d) A symmetric alignment in the cross section is possible, but provides the weakest properties along the axis. All values refer to the tensile strength of nacre as measured by [121]. Similar trends apply for compression.

1.2 SCOPE OF THE THESIS

The scope of this thesis is to design, fabricate, and characterize stiff, strong, and tough lattice structures. In particular, the focus is on the strut level, which bridges the material and unit cell hierarchies (Figure 1.6). Previously, struts have been mostly fabricated from single or composite materials [120, 122, 123]. In this work, multi-material systems are considered and combined with geometric features to establish commonly applicable architectural principles.

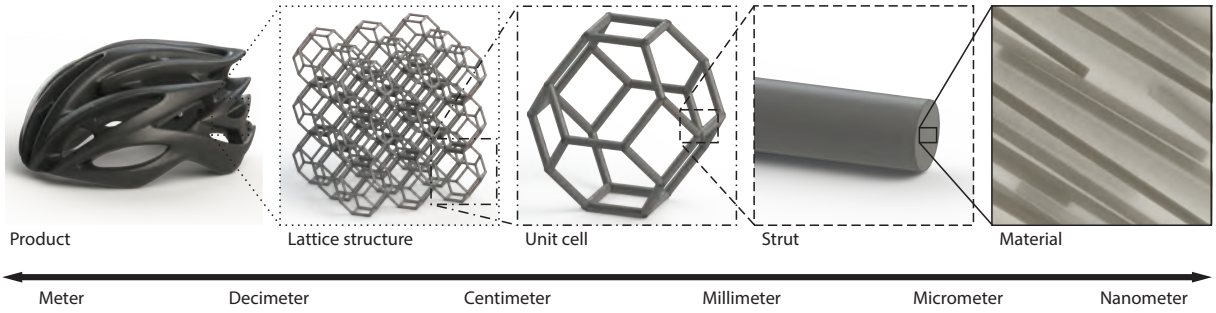

FIGURE 1.6: Hierarchies in lattice structures. Products are placed in the (super)meter-scale and can be composed of lattice structures. The lattice structures are composed of unit cells, which typically range from centimeter to (sub)millimeter-scale. The unit cells are composed of struts and formed from materials. Different combinations and subcategories exist. For example, the struts can be formed of lattice structures themselves or the material can be a composite material that contains complex features of even smaller scales.

Optimally, the principles are complementary with existing approaches and materials, and widely applicable, i.e. independent of the application, load case, scale, and material. As these

expectations vary widely and are sometimes contradictory, different routes are explored. The design rules and requirements are defined as follows.

First, to maintain comparability, the physical design space is restricted to that of a conventional strut, i.e. the same diameter and length.

Second, the load case is assumed to be in bending. Bending is the most common failure mode in bending dominated lattices, which are typically used in energy absorbing applications [68]. As buckling can be considered a sub-category of bending, this assumption also holds, within limits, for stretching dominated unit cells.

Third, as the basic requirement for the struts is to provide some degree of stiffness, at least one relatively brittle material needs to be used.

Fourth, other materials, such as flexible or ductile materials, may be added and arranged arbitrarily within the design space.

Fifth, geometric features, such as gaps between similar or dissimilar materials, may be added.

Sixth, the materials and geometric features may be aligned in a way such that the strut's cross section exhibits point symmetry with respect to the neutral axis. This ensures that the strut can equip any unit cell type without being affected by its rotation.

Application of the rules yields three feasible options. Each of these core-shell architectures which has its own characteristics, yielding different advantages and applications (Figure 1.7). The options are introduced in detail as follows.

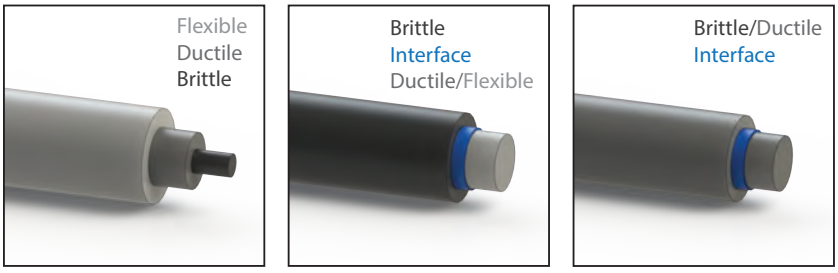

FIGURE 1.7: The focus of this work is on the strut level, which spans the gap between materials and unit cells. To maintain symmetry, the struts are radially layered. Each type contains a brittle material to provide stiffness and strength. In type I and type II, flexible material layers are added to add failure strain, hence toughness. Type III contains interfaces that allow the different layers to fail separately.

1.2.1 *Core-shell type I: brittle core, flexible shell*

Core-shell type I is based on the fact that the strain in a strut under bending increases (linearly) from the inside, i.e. the neutral axis or plane, to the outside. Typically, when designing beams or lattice struts, a material is chosen that has a failure strain larger than the maximum strain that occurs in the strut. This is usually furthest away from the neutral axis or plane, i.e. at the outside of the strut. A large portion of the material is, therefore, not strained to the maximum, hence inefficiently used. Core-shell type I replaces the material at the inside of the strut with stiffer and stronger materials. As these materials typically have a smaller failure strain, they are now efficiently used and add toughness without decreasing the effective failure strain of the strut (Figure 1.8). In the optimal case, all material layers fail at the same, predefined deflection. Failure in this core-shell type can be defined at any point on the stress-strain curve, such as plastic failure, brittle failure, or complete rupture. Gradient materials have also shown to increase the fracture toughness post failure [124–128]. In addition to the toughness, the stiffness and strength are expected to increase.

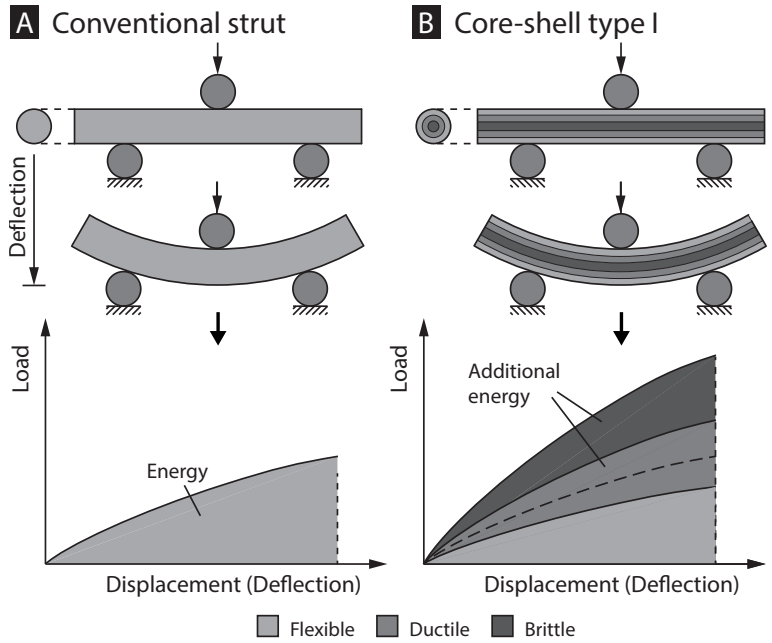

FIGURE 1.8: Core-shell type I. A conventional, single-material strut typically fails when the maximum failure strain of the material is reached (a). As the strain increases from the inside to the outside, a large portion of the material is not fully strained, hence not efficiently used. Core-shell type I replaces the core material with stiffer and stronger materials to increase toughness (b). The layers can be tuned such that all layers fail simultaneously at the desired strain.

1.2.2 *Core-shell type II: flexible core, brittle shell*

As opposed to type I, type II has a flexible core and a brittle shell (Figure 1.9). The priority of this type is to maintain stiffness by placing brittle material at the outside, where it has the largest effect, as the stiffness of a beam scales with the diameter to the power of four [1]. The core, which is less important for the stiffness, is replaced with a flexible material that is supposed to remain intact upon failure of the shell, continuing to maintain load and absorb energy. In the extreme case of a core that is orders of magnitudes less stiff than the shell, the core will not provide a meaningful load bearing capacity. It is therefore important to design the core material as flexible as necessary and as stiff as possible.

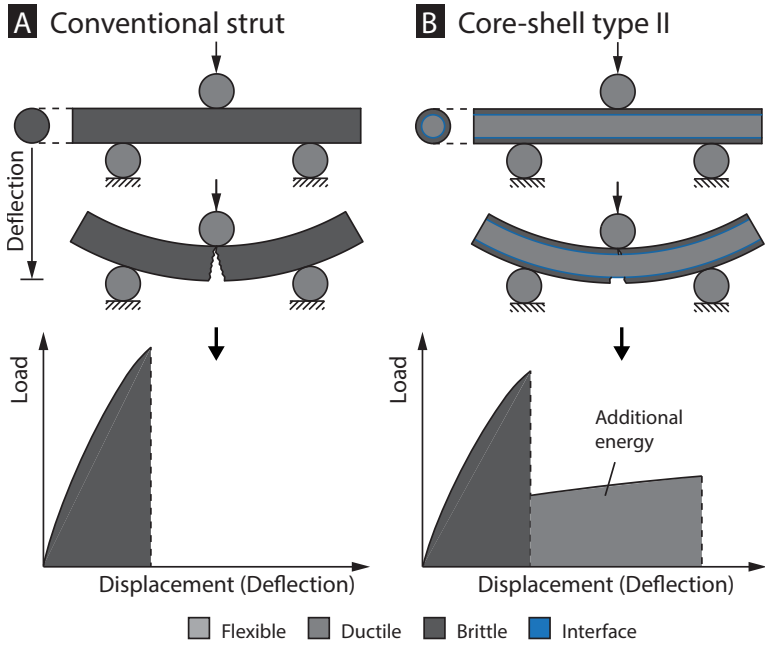

FIGURE 1.9: Core-shell type II. The stiffness of a beam increases exponentially with the diameter. Hence, the core does not significantly contribute to the stiffness. Core-shell type II replaces the core with a flexible material that prevents catastrophic failure, which adds failure strain, hence energy absorption. Optionally, an interfacial layer can be added to prevent cracks from propagating from the shell into the core.

When a crack forms in the shell, where typically the highest strain occurs, it propagates to the inside. If the core and shell materials are in direct contact, i.e. bonded, the crack propagates directly into the core. Depending on the size and material properties of the core, the core may be able to halt the crack. However, even if this is the case, the core's cross section and hence stiffness are reduced. Alternatively, by introducing an interfacial layer, the core can be separated from the shell. The interfacial layer will likely introduce a weak spot, which lowers

the stiffness, but might stop crack propagation. Both cases are investigated to find the best trade-off.

1.2.3 *Core-shell type III: brittle core, brittle shell*

Similarly to type I, advantage is taken from the increase in strain from the neutral axis to the outside. Instead of distributing different materials in a way that all fail at the same displacement, type III aims for gradual failure (Figure 1.10). Interfacial layers are introduced to separate the strut into multiple, radially aligned layers. These interfacial layers allow the carrying layers to fail when their own respective failure strains are reached, rather than observing complete rupture when the failure strain in the outermost part is achieved. As the interfaces allow each layer to fail at different deflections, the material is more efficiently used, substantially adding to the effective failure strain, hence energy absorption. As the neutral axis remains at the same position for each layer, the effective stiffness of the new strut only depends on the width and material of the interfacial layer. If the layer width is effectively zero, the strut stiffness and strength remain unaffected.

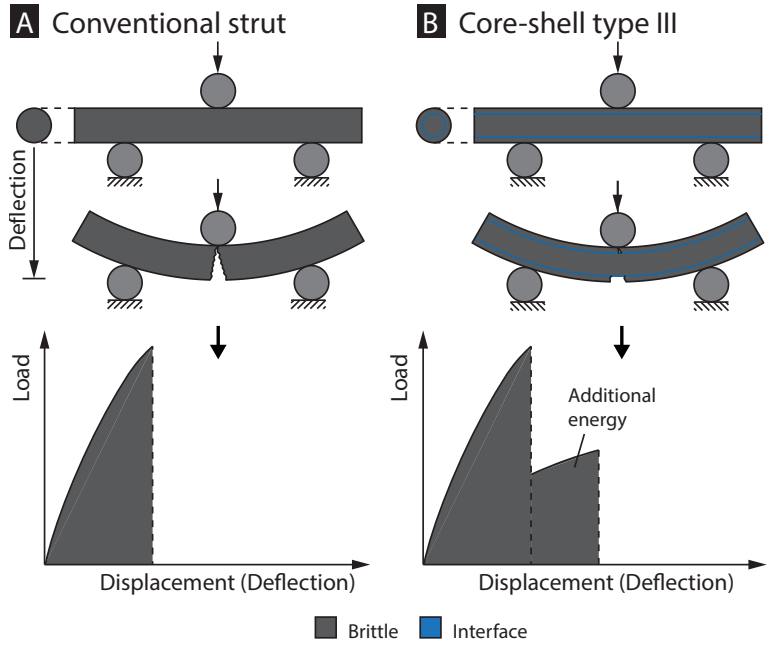

FIGURE 1.10: Core-shell type III. Similarly to type I, type III takes advantage of the strain increase from the neutral axis to the outside of a strut. The strut is split into radial layers. This prevents cracks from propagating and allows each layer to fail when its own failure strain is reached, rather than when the outermost failure strain is reached. Therefore, each layer is strained to its maximum, adding additional toughness to the system.

1.2.4 *Research objectives*

Based on the problem statement derived in Section 1.1 and further elaborated above, the main research question of this dissertation is formulated as follows.

> **Main research question:** *How can the toughness of cellular lightweight structures be increased without negatively affecting stiffness and strength?*

The main research question is addressed by investigating two main research hypotheses, H_1 and H_2.

> **Hypothesis H_1:** *The toughness of beams or struts can be increased through the addition of architectural and multi-material features without reducing stiffness and strength.*

> **Hypothesis H_2:** *The toughness of cellular structures can be increased by increasing the toughness of their struts.*

Consequently, the main contribution expected from this work is to *provide a novel design framework for the development of stiff, strong, and tough materials that are tailored to cellular lightweight structures*. As part of this, the following sub-contributions are expected.

1. The analysis of single and multi-material interfaces fabricated with the material jetting process.
2. The investigation of the mixing behavior of digital materials in the material jetting process.
3. The analysis of multi-material interfaces fabricated with the direct ink writing process.
4. The development of a novel printhead that allows extrusion of core-shell filaments. When compared to existing core-shell printheads, the developed printhead is expected to be more accurate, easy to fabricate, enable more complexity, decouple the number of layers from the filament diameter, and allow to change the core-to-shell ratios on the fly.
5. Provide design guidelines for the selection process of the different core-shell types.

The expected contributions may change in the course of the project and additional contributions and findings may appear.

1.3 THESIS OUTLINE

Das Ergebnis habe ich schon, jetzt brauche ich nur noch den Weg, der zu ihm führt.

— Carl Friedrich Gauß

Following the introduction in **Chapter 1**, **Chapter 2** investigates in detail the material jetting process for its ability to fabricate core-shell struts, as it is the most straight-forward way to create complex, multi-material structures at a high resolution. Specifically, the material mixing ability and interfaces are investigated visually via light and scanning electron microscopy and mechanically via nanoindentation. This includes single-material interfaces created through the nozzles of the printhead and layers, and multi-material interfaces between different model materials.

Chapter 3 investigates core-shell type I, where the material in the less strained core of a strut is replaced with a more brittle material. As material jetting is the most versatile process, it is used to fabricate the struts and experimentally validate the model that optimizes the material distribution in the strut. Material jetting is also the only available process that enables the fabrication of arbitrarily complex, multi-material lattice geometries with the required strut composition. Chapter 3, therefore, also investigates Hypothesis H_2, which implies that improving the energy absorption in a strut has a similar effect on the lattice as a whole.

In **Chapter 4**, the opposite strut composition as in Chapter 3 is investigated: core-shell type II with a brittle shell and a flexible core that adds toughness by continuing to sustain load when the shell fails. Two approaches are considered. In one, the core is bonded to the shell and supposed to slow down and eventually halt crack propagation. In the other approach, the core is separated from the shell through an interfacial layer that prevents cracks from propagating. The interfacial layer must be thin and not bond to either material, to reduce the weakening effect. As material jetting is not capable of complying with these requirements, direct ink writing is chosen. A novel nozzle is designed to fabricate multi-material multicore-shell struts and the performance is compared to conventional single-material struts.

Chapter 5 describes core-shell type III, which consists of brittle material layers only, where the interface is, again, critical. More layers as in type II are expected, hence the interfacial layers need to be even thinner, which makes it infeasible to be fabricated with currently available

additive manufacturing processes. As the effect of the struts on the lattice is already known from Chapters 3 and 4, struts of type III are manually assembled, which enables an interfacial layer thickness of effectively zero.

Due to their fundamental differences in the approach and fabrication, Chapters 2-5 are self-contained. In addition to the introduction provided in Chapter 1, they describe the specific challenges, related work, and methods in more detail.

In **Chapter 6**, the results of the three core-shell types are summarized and compared to each other and to literature. Their advantages and disadvantages for different applications are outlined and design guidelines are established.

Chapter 7 summarizes and concludes the thesis and provides an outlook on meaningful next steps for future work on this topic.

1.4 SUMMARY

Nature reveals promising guidelines to design stiff, strong, tough, and lightweight structures. Due to complex scaling and multi-material effects, technology has struggled to replicate them. In this work, three architectural design principles are introduced that focus on the strut hierarchy level. Each principle is investigated in detail and appropriate fabrication methods are explored to validate the theories experimentally.

2

INTERFACES AND MULTI-MATERIAL MIXING IN MATERIAL JETTING

Willst du dich am Ganzen erquicken, so mußt du das Ganze im Kleinen erblicken.

— Johann Wolfgang von Goethe

This chapter has been adapted from a manuscript published in *3D Printing and Additive Manufacturing*:

Mueller, J., Courty, D., Spielhofer, M., Spolenak, R. & Shea, K. Mechanical Properties of Interfaces in Inkjet 3D Printed Single- and Multi-Material Parts. *3D Printing and Additive Manufacturing* **4**, 185 (2017).

2.1 INTRODUCTION

For a range of applications, the multi-material capability is a highly desired feature in additive manufacturing (AM). It enables the fabrication of parts that cannot be fabricated in any other way, but makes the process more complex [81, 129]. Printing multiple materials simultaneously can increase the costs and print time, and decrease the accuracy and mechanical properties of produced parts [81]. Multi-material printing is also limited to specific processes, of which the most widely used is material jetting, commonly referred to as (inkjet) 3D printing [81, 130]. In material jetting, droplets down to a diameter of 16 μm are jetted onto a surface, which is then cured by UV light, usually mounted on the print head, before the next layer is deposited (Figure 2.1a) [131].

With the Objet500 Connex3, Stratasys presented a multi-material printer based on the inkjet technology that is capable of printing up to three different materials to cover a range of mechanical, optical, and thermal properties [131]. Besides parts that consist of one or more materials, the printer also allows on the fly mixing of base materials to form graded, mixed materials (also referred to as digital materials). It is, therefore, a suitable representation of

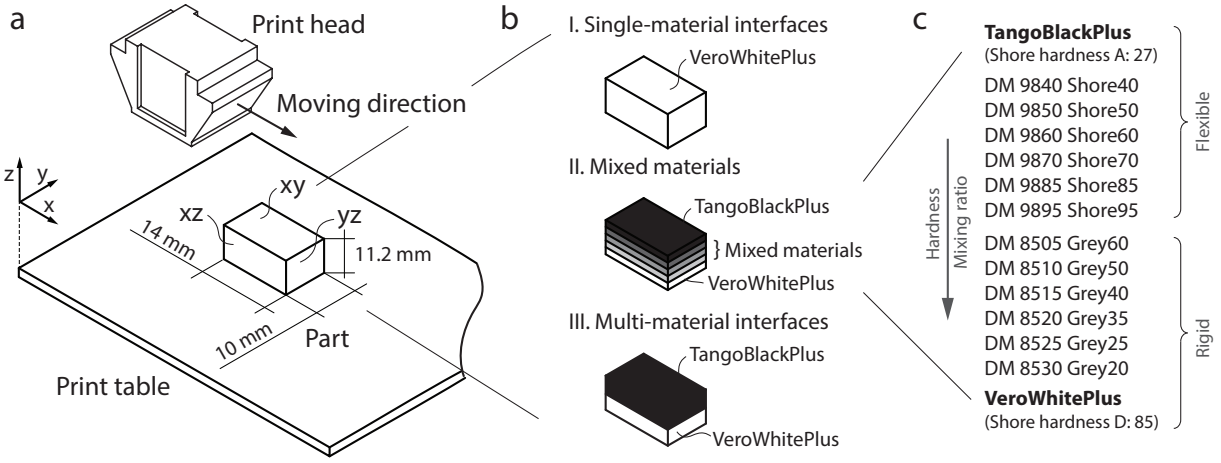

FIGURE 2.1: Setup of the printed parts with the investigated planes indicated as XY, XZ, and YZ (a). The height has been chosen to be a multiple of the printer's resolution, to prevent aliasing effects. To deposit material, the print head moves back and forth in X before it moves in Y, if the part width exceeds the print head width. The print table is lowered after each layer is finished. (b) three types of specimens are investigated: I. intersections between layers and nozzles in single-material parts, II. the mixing behavior of mixed materials, and III. intersections between two materials. The materials can be mixed with different ratios (c) to provide increasing shore-hardnesses, ranging from that of TB to VW.

state of the art material jetting processes and multi-material printing in general. The range of material combination options is depicted in Figure 2.1b, and is how this chapter is sectioned.

The first part addresses single-material parts. Material jetting allows for a high resolution and provides stiffness and strength values comparable to conventional processes, but induces a high anisotropy [96, 97, 132, 133]. Multiple researchers investigated this phenomenon and found that the weakest mechanical properties are found when loads are applied perpendicular to the layers [97, 132, 134]. As only load directions along the printer's main axes X, Y, and Z were investigated, this initial research is inconclusive. Mueller and Shea [96] looked into all the possible load orientations and found the weakest mechanical properties when the part is oriented at angles between 45^o and 60^o with respect to the axes. The reason for the anisotropy is suspected to be due to three types of interfaces: interfaces between layers, nozzle outlets, and neighboring print head passes [97]. However, all previous research has in common that it describes the macroscopic properties. No work has been found on the local, microscopic properties. It is, therefore, still unknown how the individual layers adhere to each other and how the stiffness and strength vary across the layers and their interfaces.

Material jetting also allows mixing of different materials. The user interface of the Connex3 discretizes the space into 14 increments (Figure 2.1c), but manual configuration enables any combination to yield a continuous transition between two base materials. This feature is par-

ticularly interesting for design and structural optimization, which can greatly enhance a part's performance. Further, it enables optimization methods that require continuous material properties as inputs [131, 135, 136]. Stanković *et al.* [135, 137] mechanically tested all the possible material mixtures for two fundamentally different base materials: a strong, ABS-like and a flexible, rubber-like material. They found that the mechanical properties of mixed materials are bi-modally distributed around the base materials, rather than equally splitting the space in between the base material's mechanical properties. It is, however, unknown what the reason for this phenomenon is, how exactly the material mixes, and what effect the mixing has on the mechanical properties. The second part of this work addresses the mixed materials with the aim to find an explanation for these effects.

In the third part, the interfaces of parts built from materials of opposite spectra of the elastic moduli are investigated, i.e. a stiff and a rubber-like material. On a macro-scale, Bass *et al.* [138, 139] studied variations in mechanical properties of such parts tested in tension. Vu *et al.* [140] explored the interfacial strength of parts printed with two discrete materials on double cantilever beam specimens, and so did Kumar and Alvaro [127] on single-lap joints. Lin *et al.* [141] characterized the shear strength of multi-material interfaces in dogbone specimens. Moore and Williams [142] looked into the fatigue properties of multi-material interfaces. As before, no-one looked into the local properties, which could differ significantly from the global properties that can include voids and other types of flaws.

2.2 METHODS

All specimen types are investigated visually and mechanically. Visually through a light microscope and scanning electron microscope (SEM), the printed cross sections of single-material blocks of VeroWhitePlus (VW) are investigated for each plane, XY, XZ, and YZ, where the former provides insight into the in-plane, and the two latter into the out-of-plane behavior. The results are then compared to blocks of TangoBlackPlus (TB). VW behaves like ABS and is one of the strongest commercially available materials for the material jetting process, while TB is soft and rubbery, and one of the most flexible printing materials available [131]. Those materials have been chosen to cover the largest possible range in terms of elastic modulus and hardness. Further, mixed materials of a VW primary material are investigated for all possible

mixing ratios. With nanoindentation, each of the three cross section planes is investigated on single-material blocks to test whether areas close to the interfaces provide considerably different material properties when compared to areas further away. Nanoindentation is also used to measure interfaces between blocks of TB and VW.

2.2.1 *Sample fabrication and preparation*

The test specimens are fabricated on a Stratasys Objet500 Connex3. The printer contains eight parallel print heads, of which six are allocated to three base materials, and two to a gel-like support material. Each print head contains 100 nozzles, linearly aligned along the Y axis and equally spaced. To deposit the material and cover the printable space, the assembly moves back and forth in X direction before it moves in Y (Figure 2.1a). Rollers and UV lights mounted on either side of the print head flatten the printed surface to form a smooth substrate for the next layer and immediately cure the photocurable material. Three specimens of each of the three types are fabricated in analogy to Figure 2.1b.

I. For both base materials, i.e. VW and TB, three homogeneous blocks of size 14 x 12 x 10 mm^3 are printed to analyze the layers of a single-material and their geometrical constitution – one block for each spatial direction X, Y, and Z.

II. Blocks with material gradients are printed for each base-material group. The sub-block thicknesses are chosen to be multiples of the printer's minimum layer thickness, yielding block dimensions of 14 x 10 x 11.2 mm^3. The 11.2 mm consist of 7 blocks of 100 layers, each with a thickness of 16 μm.

III. Two-material blocks of which one-half consists of VW and the other half of TB. Three specimens are printed to have the interfacial plane aligned with each of the three planes in the coordinate system, i.e. XY, XZ, and YZ.

Each specimen has been printed in a separate print job in the x_{min}/y_{min} corner of the platform with identical print parameters to prevent uncontrolled effects. The samples for the nanoindentation tests are post-processed using a standard metallurgical sample preparation procedure. For better handling, the samples are cold embedded in Demotec 35, a self-compacting and low-temperature cured polymer. Then, the surface is ground with silicon

carbide (SiC) abrasive papers in decreasing roughnesses (grids 500/1200/2500/4000) on a grinding machine (Struers RotoPol-21). A polishing step with a suspension of alumina particles (50 nm) on a polishing disk follows until no visual scratches remain. Due to the softness of TB, the preferable grinding and polishing direction is parallel to the layers and interfaces, to prevent material dragging across the interfaces. This is also true for the stiffer VW, although not as critical. For all materials, the temperature during the grinding and polishing steps must be kept below the glass transition temperature to prevent softening, which would increase the aforementioned effect and other effects that might (thermally) alter the properties.

2.2.2 *Light microscopy and nanoindentation*

The surface quality is inspected under a light microscope (Polyvar Met from Reichert) after polishing. A scanning electron microscope (SEM; Vega3 from Tescan) is used to visualize the surface of the samples. The SEM samples are coated with a thin gold layer and fixed on a sample holder with a double-sided adhesive copper band to ensure conductivity.

The nanoindentation measurements are carried out on an Ultra Nanoindentation Tester (UNHT) from Anton Paar TriTec (Figure 2.2).

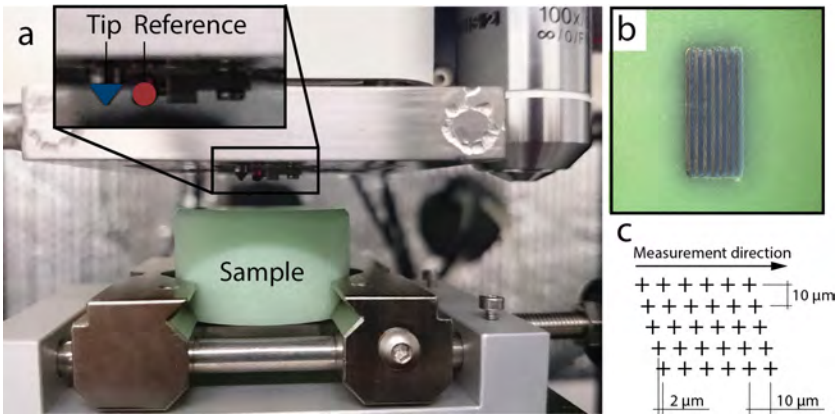

FIGURE 2.2: Measurement procedure. (a) shows the Nanoindentation set-up with the reference system. An exemplary, embedded sample is shown in (b). By shifting the alignment of the Nanoindenter's measurement profile after each line by 2 μm, an overlapping of the individual indents is prevented (c), which increases the overall resolution in the desired direction.

The distance between the reference ball and the tip is 3 mm. The reference and tip can be individually adjusted in height, so that the reference is always first in contact with the sample. Because of the small contact area and simple data processing, a pyramidal shaped Berkovich

tip is used in the experiments. For all tests, the Oliver-Pharr method is applied [143]. As the polymer material has a very low hardness, only small forces can be used. To ensure an accurate measurement, the contact force is set to 5 μN for the tip and 50 μN for the reference. The maximum indentation force is set to 200 μN, with a loading rate of 500 μN/min and an unloading rate of 5000 μN/min. In the soft materials, a 30 s hold segment is introduced at the maximum load to get reliable stress-strain curves. The distance between two measurements is 50 μm if not stated otherwise. Further, a profile is recorded to investigate the properties over a larger length scale and especially over the interface. Therefore, the distance between two indents is decreased to 10 μm to increase the resolution (Figure 2.2c). The resolution is further increased by measuring in parallel and slightly shifted lines. The shift in measurement direction is 2 μm, i.e. a property profile with a resolution of 2 μm is recorded.

2.3 RESULTS

The metallurgical sample preparation yielded a smooth and shiny surface, indicating a surface roughness much smaller than the tip size of the nanoindenter for both the soft (TB) and the hard (VW) material. Based on this outcome, experimental tests have been conducted and are discussed as follows.

2.3.1 *Single-material interfaces*

For the first part of the results, three different orientations of a pure VW sample in as-printed and polished state are shown (Figure 2.3). No significant trends are observed on the top, in-plane surface (XY) in the non-polished state (Figure 2.3a). The polished image of the XY surface is smooth with wavy features of an average amplitude of 1.4 mm (Figure 2.3b).

The non-polished XZ side is smooth and shows signs of layers in Z direction (Figure 2.3c). The layers become more obvious when polished, where they are constant in thickness and average 16 μm – the thickness set in the 3D printer (Figure 2.3d). The front view shows a bumpy surface with bumps of average diameters of 40 μm (Figure 2.3d). The bumps disappear

in the polished state (Figure 2.3f), which shows a surface with layers similar to those on the XZ surface.

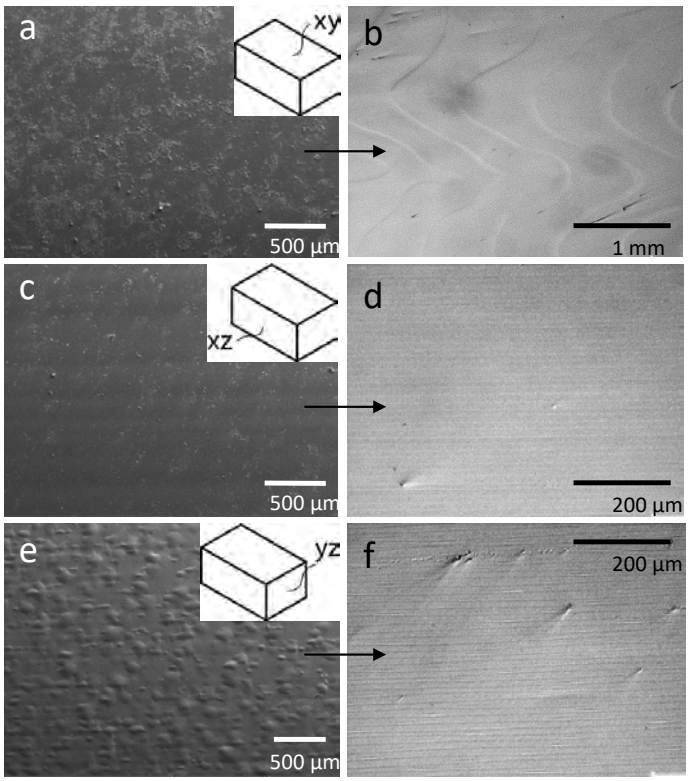

FIGURE 2.3: Interfaces in single-material parts. As-printed surfaces (a, c, e; SEM) and the final, polished cross sections that are used for the nanoindentation (b, d, f; light microscope) of the XY (a, b), XZ (c, d), and YZ (e, f) planes of a VW sample.

A comparison of the side view between TB and VW layers is shown at a higher magnification in Figure 2.4. When compared to VW, the TB layers show a higher non-uniformity and deviation, but yield the same average thickness of 16 μm. In all cases, no defects in the form of holes are seen.

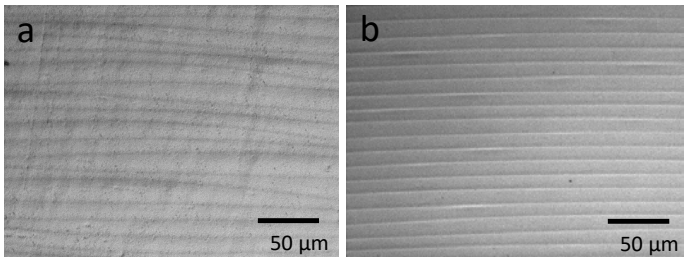

FIGURE 2.4: Interfaces in single-material parts. A further magnification is shown for TB (a) and VW (b), where the former shows clear deviations from the average thickness along the length.

To get the local, mechanical properties for all three spatial planes, XY, XZ, and YZ, the hardness and stiffness profiles of pure VW blocks are measured by nanoindentation (Figure 2.5). For both the hardness and the stiffness, the means (magnitudes) are well within the

deviations (amplitudes). Specifically, the hardnesses average 269 ± 19 MPa (XZ), $278 \pm 16 MPa$ (XZ), and 270 ± 18 MPa (YZ) among the planes, and the moduli average 4121 ± 143 MPa (XY), 4254 ± 174 MPa (XZ), and 4230 ± 122 MPa (YZ).

None of the graphs show distinct trends within the length or peaks at a distance of the respective printer resolution, i.e. 600 dpi in-plane and 1600 dpi out-of-plane. This is confirmed by a fast Fourier transform analysis, which does not show any peaks at the expected distance, suggesting that the mechanical properties are uniform across the layers. In addition, no delamination of the layers is observed during the tests, indicating that the resulting material is homogeneous.

2.3.2 *Material mixing*

An additional level of complexity is added with multi-material printing. The finely dispersed nozzles of the printer in combination with the print heads that are aligned in parallel behind each other deposit the secondary material into the material matrix formed by the primary material. Light microscope images of all the possible VW based mixtures are shown in Figure 2.6.

Starting with pure VW on the left, the TB ratio increases from layers one to seven. Elongated features of about 5 μm width and 70 μm length appear and increase in number with increasing TB amount.

Figure 2.7 shows property profiles of VW and TB. It starts with pure VW on the left of Figure 2.7a, and continues with an increasing ratio of TB towards the right until pure TB is reached on the right of Figure 2.7b. The distance between two indents is 50 μm. In both cases, the hardness and stiffness values are relatively constant with no statistically significant trend, rather than decreasing, as one would suspect. The values of the TB based materials show a higher standard deviation from the mean.

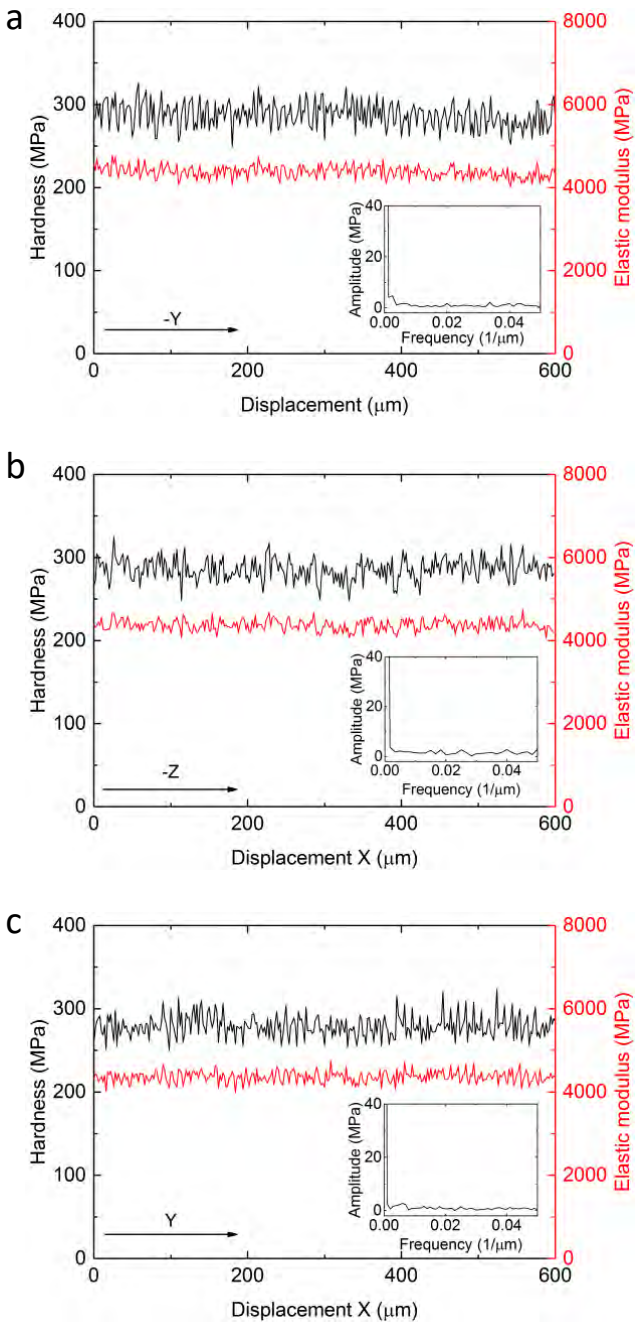

FIGURE 2.5: Interfaces in single-material parts. Hardness and elastic modulus profiles of a VW sample for each cross sectional plane are shown in i (XY), j (xz), and k (yz). It cannot be distinguished between peaks in a distance of the printer's resolution and noise. Fast Fourier transform analyses of the hardness profiles are shown in the insets and confirm the observation.

2.3.3 *Multi-material interfaces*

The results of the analysis across the interface of VW and TB are shown in Figure 2.8, where Figure 2.8a shows the actual surface as seen by a light microscope.

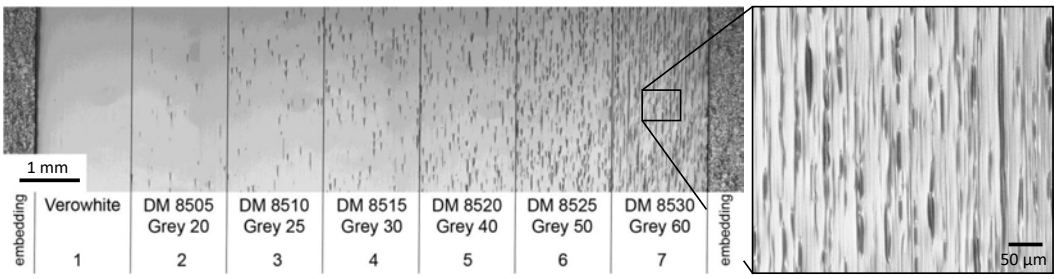

FIGURE 2.6: Mixed materials. Cross section of pure VW (left) with increasing TB ratio towards the right. The dark shades are inclusions of the second material phase, in this case, TB. With an increasing mixing ratio, the number, and size of the inclusions increases. The main material remains dominant, even for the highest mixing ratio, indicating that one dominant material phase is required and an equal mixing not achievable.

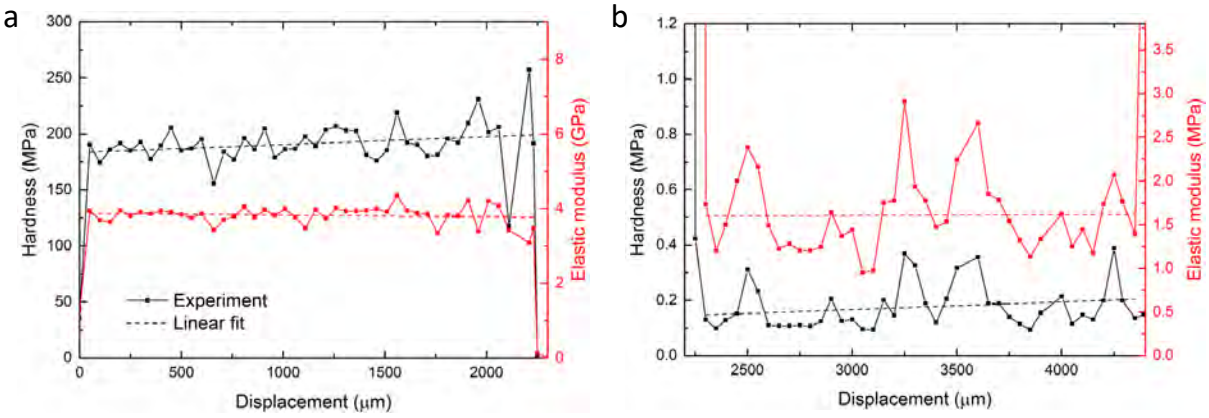

FIGURE 2.7: Mixed materials. (a,b) property profile of a continuous sample with discrete steps of increasing TB ratio. (a) VW base material, (b) TB base material. The material to the left of (a) is pure VW and the material to the right of (b) is pure TB. The values in between increase their mixing ratios accordingly.

Visual observations show that the indents are small on VW and larger at the interface. The indents on the TB side are deeper and partially overlap with the VW, which is seen by the shifted indents on the interface. This can also be seen when looking at the mechanical properties, which decrease continuously from one phase into the other (Figure 2.8b). The mean elastic modulus and hardness for the pure materials are found to be 1.081 MPa and 0.095 MPa for TB, and 4463 MPa and 285.2 MPa for VW, respectively – more than three orders of magnitude in difference (Figure 2.9). No delamination between different materials is observed in any of the tests.

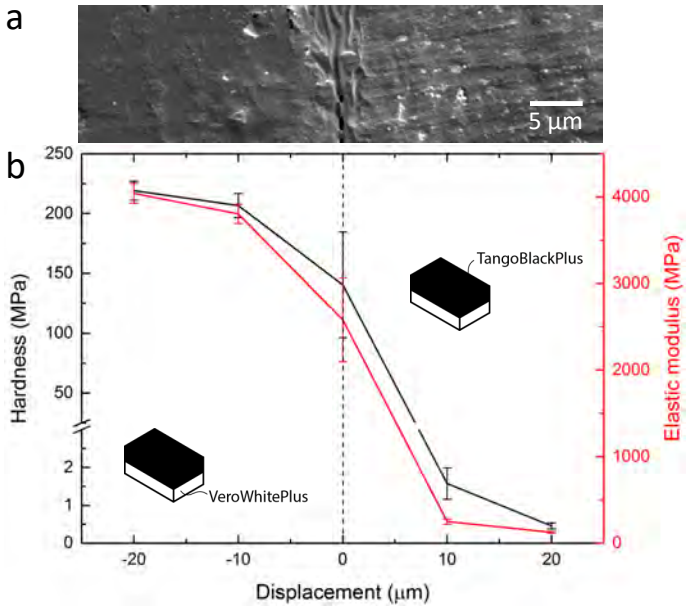

FIGURE 2.8: Multi-material interfaces. (a and b) Profile of the intersection between VW (left) and TB (right). (a) Light microscope and (b) nanoindentation results. Due to the indent size in the TB material, the indenter overlaps with VW in all measurements. No delamination has been observed in any of the measurements.

	VeroWhitePlus	TangoBlackPlus
Hardness (MPa)	285.2 ± 10.9	0.095 ± 0.027
Stiffness (MPa)	4463 ± 154	1.081 ± 0.165
Indent depth h_c (nm)	187 ± 4	9744 ± 1395
Indent length (µm)	≈ 1.2	≈ 63

FIGURE 2.9: Multi-material interfaces. Mechanical properties of pure VW and TB obtained further away from the interface.

2.4 DISCUSSION

The metallurgical sample preparation has proven to be applicable to the tested polymer samples. This is particularly important due to the large discrepancy in hardness and modulus between the TB and VW materials, which are combined in the same samples. In the following paragraphs, the results of the different interfaces and material mixing are discussed.

2.4.1 *Single-material interfaces*

The smooth yet wavy in-plane surface likely originates from a combination of imperfections in the printing process and a small misorientation in the embedding and grinding (Figure 2.3a,b). To minimize this visual effect, a deviation in parallelism of the layers and the machining table

much smaller than the layer thickness is required. Further, the rollers of the print heads flatten each layer after being deposited, either for both a better surface finish and to provide a smooth deposition surface for the forthcoming layer. This process postulates that material is being dragged along the moving direction of the print head. Even small deviations of the mean height across the print head's nozzles (Y direction) yield a waviness.

A layered structure is visible on both out-of-plane surfaces (Figure 2.3c-f). The thickness of the sublayers is 16 μm and constant over the length in the XZ direction; the YZ direction shows higher variations, but yields the same mean thickness. This is due to the layer-wise approach, that deposits, flattens and hardens each layer before depositing the next layer. Since the cured layers below the current layer are magnitudes stiffer than the liquid ink, the layers keep their shape even if the deposited material distribution is non-uniform, forcing the excess material to squeeze out on the sides. This can be seen in the images showing the samples' non-treated outside-surface (Figure 2.3e).

Variations in layer thickness along the Y directions can be explained with deformation happening during the deposition process. While VW yields layers of uniform thickness in the out-of-plane orientations, the layers of TB are non-uniform in thickness, but yield the same average of 16 μm. This is due to the stiffness of TB being orders of magnitudes lower than of VW, even in the cured state. The rollers, mechanically flattening the layers, therefore experience less resistance when spreading the material across the surface, potentially deforming the formerly printed layers to a larger extent. As the outer dimensions of the parts are not affected by these effects, there are no design considerations to account for.

The absence of holes and defects shows that a very low porosity is achieved, which is often considered a measure of quality in 3D printed parts, where porosity can lower the mechanical properties, such as stiffness and strength [144]. Porosity can also induce a higher degree of anisotropy.

Nanoindentation tests in the three planes show no distinct trends within the length or peaks at a distance of the respective printer resolution. In addition, no delamination of the layers is observed during the tests. This suggests that the mechanical properties are uniform across the layers and planes, hence that the parts are homogeneous and isotropic.

2.4.2 *Material mixing*

The elongated features' shape seen in Figure 2.6 reminds of fibers or whiskers and is suspected to be created due to a combination of factors. First, the relatively fast movement of the print heads does not allow a punctual deposition. Second, the deposited droplets are dragged behind due to the rheology of the ink. Third, due to the rollers being mounted on both sides of the print head, the surface is flattened for the next layer. As opposed to conventional composite materials, where the inclusions typically strengthen or stiffen a given base material, in material jetting they can also be used to achieve the opposite, e.g. a softer and more flexible material [145]. An increased mixing ratio yields more inclusions, and the inclusions' characteristic sizes are limited to the inner nozzle diameter or resolution of the printer.

Nanoindentation measurements of mixed materials show relatively constant trends for both the hardness and the modulus (Figure 2.7), rather than decreasing trends with increasing TB ratio, as one would suspect. This is due to the particles being randomly dispersed and, therefore, only randomly hit by the indenter, as verified visually. As the ratios are relatively low, even in the case of the highest mixing ratio, the chances are high that the indenter mostly hits the matrix material. Further, especially in the case of TB, where the hard (VW) particles are supported by a soft matrix, the indenter is likely to move the whole particle rather than purely measuring its local properties. The latter argument is strengthened by the fact that the indentation depth in TB needs to be much higher to measure the same force as in VW, reaching almost 63 μm in the pure TB case.

These findings suggest that design guidelines similar to conventional, (short-)fiber-reinforced composite materials apply [146]. In particular, that the size of the designed parts or features needs to be much larger than the inclusion size of about 5 μm to 70 μm. Typically, a rule of thumb is that the minimum part size needs to be ten times larger than the maximum feature size of the inclusions.

2.4.3 *Multi-material interfaces*

The absence of delamination between any of the tested materials indicates the bonding is stronger or at least as strong as the weaker material. Those results are in accordance with the findings of Libonati *et al.* [147], who reported a perfect bond on macro-scale tests. In terms of the mechanical properties measured through standardized tensile tests, Stanković *et al.* [135] found similar moduli for the TB, but smaller moduli for the VW material (0.989 MPa and 3085 MPa, respectively) when compared to this study. Similar values are reported by Stratasys, i.e. 0.8 MPa to 1.5 MPa for the TB, and 2000 MPa to 3000 MPa for the VW material [131]. Measurements on the micro-scale, as used in this work, investigate purely the local and actual material properties, whereas macro-scale tests average over everything, including local imperfections and flaws that can act as stress concentrations. This also explains the larger discrepancy of the stiffer VW material (3085 MPa to 4463 MPa, i.e. 31%), which is much more prone to such stress concentrations than the softer TB (0.989 MPa to 1.081 MPa, i.e. 9%).

The findings suggest that the interface is not a weak spot. In addition, the higher moduli found on the micro-scale when compared to the reported values are in accordance with what has been reported in literature. and do, therefore, not imply a need for specific consideration in the design process [113, 148].

2.5 CONCLUSIONS

Rather than molecular mixing, the mixing of materials in material jetting is found to be comparable to the mixing in conventional composite materials, where stiff fibers are embedded in a soft material matrix or vice versa. This has multiple consequences. First, it is not possible to achieve a continuous material distribution, even if the supplier software allowed users to set user-defined ratios. Second, a local anisotropy is introduced that differs from the global anisotropy introduced by the printer. Third, the composite effect of the mixed materials is only effective if the size of the part or feature is much larger (i.e. one order of magnitude) than the inclusion size, which ranges from 5 μm to 70 μm. It is hence inapplicable to use mixed materials for parts and features smaller than 700 μm. In terms of single-material in-

terfaces, hard materials produce layers of uniform height, which is opposed to soft materials. No deviation in the elastic modulus or hardness is found when comparing regions near the interface to regions away from it, which suggests that the macroscopic anisotropy found in previous research [96–98, 135, 137, 149] is due to flaws and imperfections. Metallurgical specimen preparation generally proved to be appropriate for inkjet 3D printed polymeric parts, even for the soft material. In multi-material interfaces, no evidence has been found that the bonding of the interface is weaker than the bonding within the base materials.

The implications on the design of 3D printed parts using this AM process are twofold. For single-material parts and parts consisting of blocks of materials, designers can use the properties of the selected materials with a high certainty that they are valid, even for small parts and features. This is due to the negligible effect of the interfaces in the experiments. For mixed material parts, however, the threshold above which the composite effect comes into play needs to be found and likely varies among different material combinations, load directions, and mixing ratios.

The implications for printing core-shell architectures are as follows. Core-shell type I requires layers of materials with different stiffnesses and no interfacial layers between them. Material jetting can be used for the core-shell type I, given that layer thicknesses of mixed material layers are not smaller than 700 μm. This minimum layer thickness also applies to interfacial layers, as required by core-shell types II and III. Due to the material being liquid when jetted onto the substrate, it is hardly possible to prevent bonding between different materials and no material combinations are offered that do not bond. Proprietary development of new materials is not possible on the commercial printer, leaving support material with effectively zero strength as the only option. The interfacial layer would, therefore, introduce significant weakening of the cross section, making the material jetting process infeasible for core-shell types II and III.

2.6 SUMMARY

Material jetting, commonly referred to as (inkjet) 3D printing, of polymers offers multiple advantages over other processes, such as a high resolution and multi-material capability. Most published research investigates the macroscopic properties of inkjet printed parts [96–98, 130,

134, 138, 139]. This work studies the mechanical properties on the micro-scale, in which metallurgical sample preparation and nanoindentation have proven to be appropriate tools for investigating parts with stiffnesses ranging over three orders of magnitude.

First, interfaces in single-material parts that are created through jetting of material in layers and through nozzles, are investigated. Visual inspections of the samples show a uniform layer thickness for rigid materials and irregular layers for flexible materials. The hardness and modulus near the layer interfaces show similar values to those further away, indicating a uniform curing throughout the layers. Second, the on the fly material mixing of the printer is investigated and shows a dominating base material with elongated features induced from the secondary material. This reveals that the mixing is an introduction of particles, rather than molecular mixing. As a consequence, the local material characteristics differ strongly from the global properties of printed structures. Third, interfaces of dissimilar materials are investigated and show a smooth transition in the mechanical properties from one material to another.

In agreement with interface investigations on a macro scale [150], the findings give rise to the assumption that core-shell type I can be fabricated using the material jetting process, which offers the most straight forward way to validate the proposed theories. The lack of non-bonding and structural materials in combination with a minimum layer thickness of 700 μm makes the process infeasible for core-shell types II and III.

3

CORE-SHELL TYPE I: BRITTLE CORE, FLEXIBLE SHELL

Discovery consists of seeing what everybody has seen, and thinking what nobody has thought.

— Albert Szent-Gyorgyi

This chapter has been adapted from a manuscript under review:

Mueller, J. & Shea, K. Multi-Material Multicore-Shell Struts for Maximized Energy Absorption in Cellular Lightweight Structures. *(Under review)*.

3.1 INTRODUCTION

Increasing the energy absorption capability or toughness of lightweight structures without reducing stiffness or strength has been a long-standing challenge as numerous applications exist with potentially great impact. Particularly, in volume or weight restricted environments, such as cars, helmets or packaging, the performance, safety, cost, and environmental impact is substantially affected. However, these properties are also typically mutually exclusive [12].

Discrete, open-cell lattices is an emerging class of materials that addresses these challenges. They offer superior advantages over solid materials or closed-cell foams, such as high permeability, light weight, and direct control over the local architecture. This control can be exploited to increase the structure's efficiency by optimizing the material distribution inside the volume [135, 137, 149]. Depending on the application or load case, typically, a unit cell is tessellated in a periodic or random manner to form a cellular network. Bending dominated unit cells are preferred for toughness, as they provide the best trade-off among stiffness, strength, and failure strain [68]. Each of these properties needs to be as high as possible as they define the area under the stress strain curve, hence toughness, of a system [151, 152].

To improve the efficiency further, the unit cell density, material, and type can be varied across the lattice [135, 137, 149, 153–156]. A unit cell consists of struts that significantly affect the lattice's properties (Figure 3.1). Dependent on the nodal connectivity and type, i.e. fixed

(beam) or free in rotation (truss), the struts fail from yielding, buckling, or bending [68]. In either case, stiffness and strength significantly depend on the strut's radius, i.e. the larger the radius, the stiffer and stronger the underlying structure.

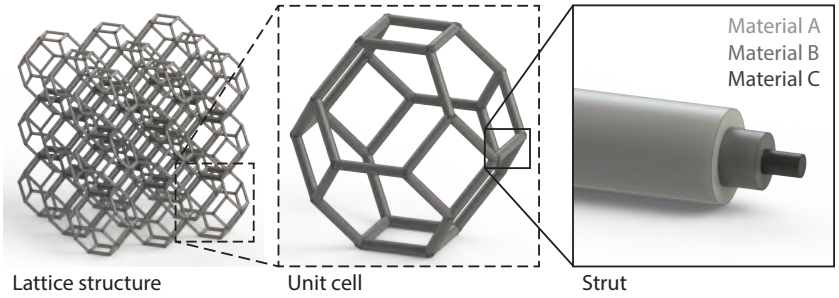

FIGURE 3.1: Different hierarchies of a lattice, where the strut is the focus of this work.

When a strut is bent, the strain increases linearly from the neutral axis to the outside [157]. Upon reaching the failure strain of the material, a crack forms, reduces the effective cross section, and creates a stress concentration. Depending on the material characteristics, the stress concentration allows the crack to travel rapidly through the strut causing (catastrophic) failure [158]. At the time of failure, the material's maximum strain is reached at the outside of the strut only. The material on the inside is not fully strained, hence less efficiently used.

Removing material from the inside of a strut ensures a more efficient use of the weight and takes advantage of the fourth order increase in stiffness with diameter. Resultingly, the weight of the structure is reduced more than the mechanical properties, increasing the relative mechanical properties. This procedure is well known and widely used in structural elements, such as tubes or I-beams [157]. It has also been shown that lattices with hollow or foam-filled struts perform significantly better than solid struts when related to the structure's mass or volume [109, 110, 151, 156, 159–162].

An alternative approach replaces the core with a tougher material that does not fail upon crack inset [158]. The approach can double the toughness of a strut, with only minor reduction in stiffness and strength. To minimize crack propagation in stiff lattices, layered struts have been proposed, where each layer fails when its respective failure strain is reached, rather than when the outermost layer fails [163]. Many of these approaches require significant (plastic) deformation or fracture for the mechanism to set in and are hard to fabricate into complex structures [158, 163].

In this work, a new, architectural paradigm is proposed that significantly increases the stiffness, strength, and energy absorption of a beam before failure or fracture. Traditionally, if failure is undesired, a material with a failure strain marginally higher than the maximum strain that occurs in the structure is chosen. This assures maximum stiffness and strength, which are often additional requirements, and which help to increase the energy absorption. Instead of creating hollow or foam-filled struts, the material on the inside is replaced with stiffer and stronger materials (Figure 3.2c,d). To be independent of the load case, the materials are radially layered (Figure 3.2d), but could be in any other shape. The layer diameters depend on the maximum deflection and available materials. They are calculated such that the material's failure strain is identical to the maximum failure strain that occurs in the layer at the desired deformation (Figure 3.2d). Due to the mutual exclusivity, this allows one to select materials that have a smaller failure strain than the material on the outside and therefore higher stiffness and strength [12]. The stiffness, strength and failure strain of the strut are optimized for a given deflection to maximize the energy absorption (Figure 3.2e-f).

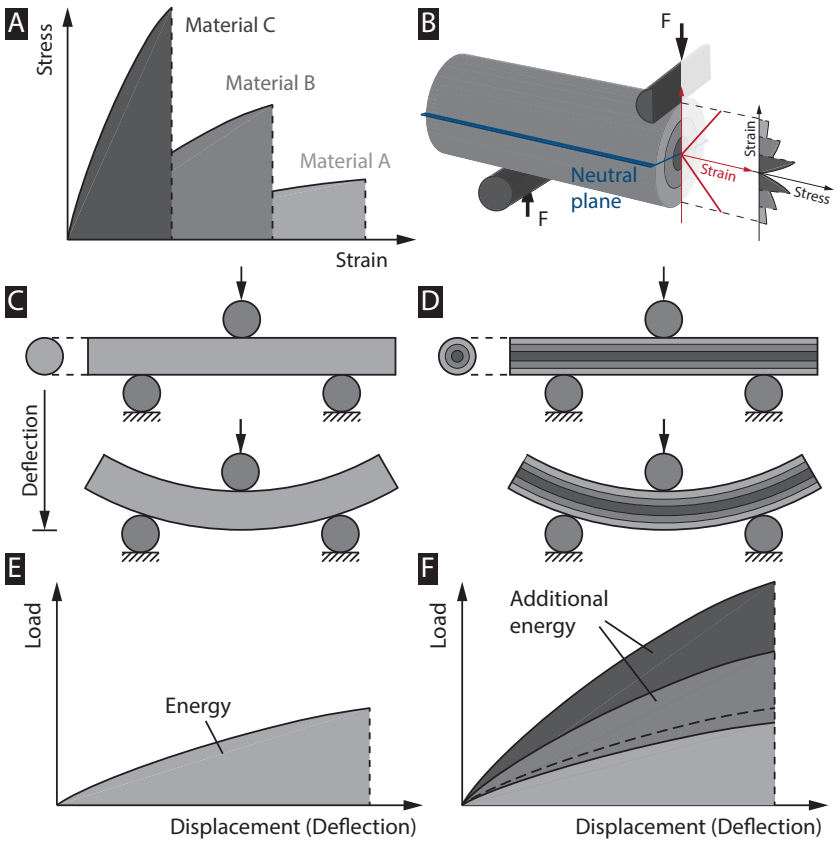

FIGURE 3.2: Struts consist of layers of different materials (a), chosen according to the maximum strain in the bent cross section of the strut, such that all layers sustain the prescribed strain (b). Hence, under bending, the single and multi-material struts can deflect the same distance (c,d). The load-displacement curves reveal that the multi-material strut has the potential to absorb significantly more energy (e,f).

First, a model is developed that predicts the load-displacement diagram of a beam in three point bending, from which the energy absorption can be obtained, based on the material's actual stress-strain data. The model takes into account both large deflections and non-linear material models, which consider plastic deformation and failure. Second, the model is experimentally validated for a range of different parameters. Specifically, on single-material rods with different diameters and on two-material struts with different core-to-shell ratios, defined as the ratio of the core diameter to the outer (shell) diameter. Third, the model is used to investigate the effect of more than two layers and the effect of different materials. To cover all options, typical engineering materials (polymers) are selected ranging from brittle, to ductile, to flexible. Fourth, the hypothesis that increasing the energy absorption in a strut also increases the energy absorption in a unit cell and lattice is experimentally validated.

3.2 METHODS

A model is introduced to calculate the load-displacement curve from a three point bending test for various materials. Specifically, the model is able to read arbitrary stress-strain data in numerical form, as obtained from mechanical tests. The model is validated experimentally on struts of different configurations, fabricated with material jetting. This allows expansion of the model to different classes of engineering materials and an arbitrary number of layers. The methods section also describes the design, printing, and testing of unit cells and lattice structures.

3.2.1 *Model*

The modeled system consists of a beam with a circular cross section that is loaded in three point bending. Simplistically, the beam can fail in tension on the bottom face, compression on the top face, by shear, or by some interaction of these stresses [164]. The mode of failure depends strongly on the span-to-depth ratio, L/D. Short beams usually fail in shear and long beams by tension or compression [165]. For L/D ratios > 16:1, where deflections in excess of 10% of the support span occur, ASTM D790 offers a correction factor to reasonably

approximate the stress in the outer face of a simple beam [166, 167]. The recommendation is based on non-linear beam theory, which distinguishes two cases. In the first case, the edges are constrained from moving in the lateral direction (constrained edges). The beam length increases and an additional tensile force is produced in the beam. In the second case, one edge can move horizontally, effectively decreasing the span length (unconstrained edges). Both theories account for initially vertical forces that change direction as the beam rotates around the supports [168]. In this work, non-linear (Euler–Bernoulli) beam theory is adapted to fixed supports, on which the beam can freely move and rotate.

Non-linear beam theory considers linear-elastic material properties only, but models for non-linear material models exist, such as the simple plastic theory [169, 170]. In the most basic forms, these theories are applied to calculate plastic hinging and use elastic-perfectly plastic material models as an input [157]. This is not sufficient for the arbitrary material models used in this work.

Herbert [164] found that both the tension and compression stress-strain curves of a material can be determined with a single bending specimen. His theory has been adapted and extended by Allen, Aveston *et al.* [171, 172], and others [173–177]. One established method is the elliptic approach by Bisshopp and Drucker [178], which is still widely used [179, 180]. The problem has also been examined numerically through iterative shooting techniques [181–183] and incremental finite element or finite difference methods with Newton-Rhapson iteration techniques [184, 185]. The drawbacks of these numerical models are their applicability, complexity, and stability [177]. Instead of calculating the stress-strain data from load-displacement curves, in this work, the problem is inverted and a model (in the following referred to as "the model") is proposed that calculates the load-displacement curve from arbitrarily complex stress-strain data.

The following assumptions apply. The strain distribution is taken to be linear following Timoshenko's assumption of plane sections remaining plane before and after bending [186]. A constant cross section is assumed throughout the displacement. If required, cross sectional changes at large strains (often considered > 5%) can be compensated for [174]. Three-dimensional effects (e.g. through Poisson's ratio) can be neglected when the length of the beam is larger than the thickness of the perpendicular cross section and this is shorter than

the curvature radius of the beam [187]. Further, the deflection due to self-weight is assumed to be zero, implying a massless beam [187].

Instead of a linear elastic or linear-perfectly plastic distribution of the stress from the neutral axis/plane to the outer bottom/top faces, as is the case in the linear and non-linear beam theories, the stress distribution in this work can be arbitrary. The curve is described numerically in the form of stress-strain pairs (Figure 3.2d). The bending moment of the beam is calculated with the load, F, and the span length, L (Figure 3.2d) [1].

$$M = \frac{FL}{4}. \tag{3.1}$$

In the cross section, the moment is calculated by integrating the forces, dF, across the area with their respective distances from the neutral axis, y.

$$M = \int_A y dF = \int_A y\sigma_{(y)} dA. \tag{3.2}$$

Since dF is equal to the product of the stress, σ_y, and area, dA, the stress distribution results in the total moment. The area can be expressed as a function of the chord length, c_y, of the circular cross section, which depends on the distance from the neutral plane, y [1]. The relationship can also distinguish between tension and compression asymmetry on the two sides of the neutral axis.

$$c_{(y)} = 2\sqrt{r^2 - y^2}. \tag{3.3}$$

Integrating the chord length over the height, which is defined by two coordinates normal to the neutral axis, y_1 and y_2,

$$dA = \int_{y_1}^{y_2} c_{(y)} dy \tag{3.4}$$

the area of a ring is calculated by subtracting the chord of the inner circle from the total. By combining Equation 3.2 and Equation 3.4, the moment is expressed as

$$M = \int_A y\sigma_{(y)} dA = \int_{-y_{max}}^{y_{max}} y\sigma_{(y)} c_{(y)} dy. \tag{3.5}$$

Substituting Equation 3.1 yields the flexural load-displacement curve as a function of the given stress-strain curve of the material,

$$F = \frac{4}{L} \int_{-y_{max}}^{y_{max}} y\sigma_{(y)} c_{(y)} dy. \tag{3.6}$$

By integrating Equation 3.6 over the displacement, δ, the total energy required to deform the strut, U, is calculated.

$$U = \int_0^{\delta_{max}} F d\delta = \frac{4}{L} \int_0^{\delta_{max}} \int_{-y_{max}}^{y_{max}} y\sigma_{(y,\delta)} c_{(y)} dy d\delta \tag{3.7}$$

The total modulus of the strut is calculated as

$$E_{tot} = \frac{I_1 E_1 + I_2 E_2 + \cdots + I_n E_n}{I_{tot}}, \tag{3.8}$$

with the total second moment of area, I_{tot}, of a circle

$$I_{tot} = \frac{\pi}{4} \left(\frac{d}{2} \right)^4. \tag{3.9}$$

where d is the diameter of the beam.

3.2.2 *Materials*

For the single-material struts and cores, a rigid high temperature material with a flexural strength of 110-130 MPa, a flexural modulus of 3200-3500 MPa, and a failure strain of 10-15% is used (RGD525, Stratasys Ltd. Eden Prairie, Minnesota, United States) [131]. For the shell, a flexible, rubber-like material with a strength of 9-12 MPa and a failure strain of 27-40% is used (FLX9695, Stratasys Ltd. Eden Prairie, Minnesota, United States). FLX9695 is a digital material, i.e. a mixture of RGD525 and TangoBlackPlus model material.

3.2.3 *Fabrication*

The specimens are fabricated on a Stratasys Objet500 Connex3 printer using the "matte" option, which covers all sides in a soluble support material (SUP706) to assure a smooth and uniform surface finish. All struts are aligned in X direction during printing while keeping all other parameters constant. The struts are immediately removed from the printer, cleaned from support material, and tested within six hours to reduce side effects [96–98].

The single-material struts are 100 mm in length and have diameters ranging from 1 mm to 8 mm. The core-shell struts have the same length, an outer diameter of 8 mm, and core diameters ranging from 1 mm to 8 mm. The unit cells and lattices are composed of struts with an outer diameter of 4 mm and, if applicable, core diameter, of 2.5 mm. The cell size of the individual unit cells is 60.57 mm in length, width and height. The lattices, composed of 3x3x3 unit cells with 32.28 mm cell size, has outer dimensions of 88.75 mm in length, width and height. This yields a relative volume of 12%.

All parts are printed in an air-conditioned room at a temperature of 21+/-0.5°C.

3.2.4 *Characterization*

The model accuracy is validated through three point bending tests on single-material struts with diameters ranging from 1 mm to 8 mm and on multi-material core-shell struts with an outer diameter of 8 mm and inner diameters of 0 mm to 8 mm (Figure 3.3). The experiments are conducted on a Zwick/Roell Z005 universal testing machine equipped with a 5 kN load cell and a three point bending test rig with revolving roller diameters of 8 mm and a span length of L = 50 mm at a test speed of 20 mm/min. The unit cell and lattice experiments are conducted on the same machine in compression with a test speed of 10 mm/min, using polished steel plates with a diameter of 86 mm.

All tests are conducted in an air-conditioned room at a temperature of 21+/-0.5°C.

3.3 RESULTS

Experimental results are presented individually for single struts, unit cells, and lattices. For the single struts, results are also shown for the analytical and numerical model, and compared to those of the experiments.

3.3.1 *Individual struts*

The results from the experimental tests of individual struts are presented and used to validate the model. The model is then expanded to typical engineering materials and a larger number of layers to draw more general conclusions.

3.3.1.1 *Experimental validation of the model*

To validate the model, three point bending tests are conducted on struts of different configurations. Specifically, single-material struts are fabricated from brittle material (Figure 3.3a) and two-material struts are fabricated with a brittle core and flexible shell (Figure 3.3b).

The load-displacement diagram for the single-material struts shows a gradual decrease in the maximum load from 350 N for the 8 mm diameter to 1 N for the 1 mm diameter sample (Figure 3.3c). A similar trend is observed for the stiffness and failure strain. The core-shell curves look similar for the 8 mm core diameter, which is equivalent to the single-material version, and move increasingly towards higher loads with increasing core diameter, due to the added effect of the shell (Figure 3.3d). Compared to the single-material struts, curves of the core-shell struts with a small core diameter are closer to the pure flexible material. Figure 3.3c and Figure 3.3d also show the computed curves, with little deviation from the tested struts.

3.3.1.2 *Expansion of the model*

Next, the core-to-shell ratio is individually optimized for maximum energy absorption for every displacement from 0.1 mm to 30 mm in increments of 0.1 mm, taking the pure flexible and the pure brittle material as inputs (Figure 3.3e, top/center). The optimization variables are

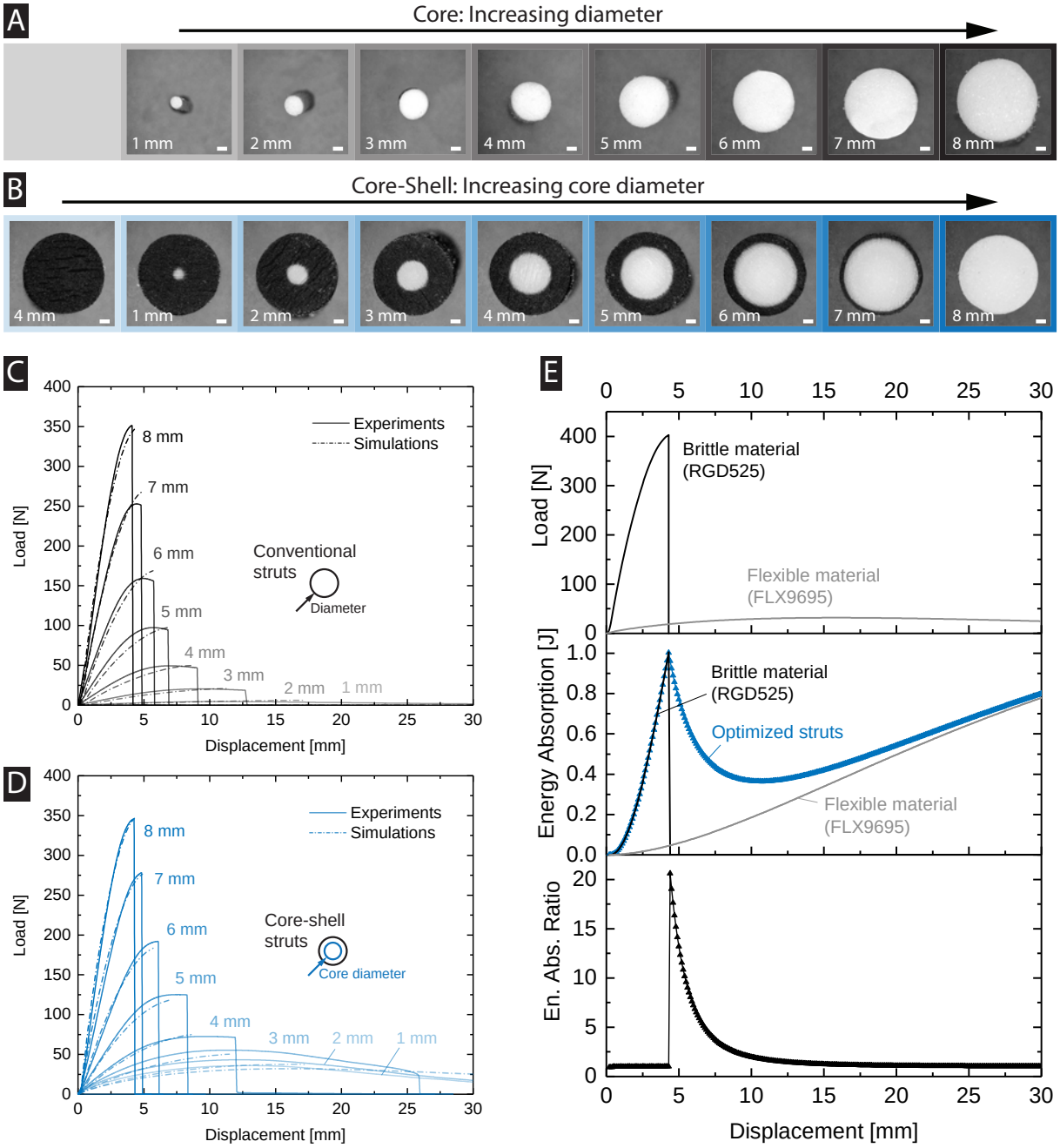

FIGURE 3.3: Struts – experiments and model validation. Struts in different configurations are 3D printed and tested: single-material with diameters ranging from 1 mm to 8 mm (a) and two material core-shell struts with an outer diameter of 8 mm and the same inner diameters as the single-material struts (b). In both cases, a larger (core) diameter yields a higher load and a smaller displacement at failure (c,d). These results show good agreement with the model. The core-shell structures at smaller core-to-shell ratios, however, fail significantly later than their single-material counterparts (d). The model is also used to find the optimized core-to-shell ratio, hence the maximum energy absorption, for a given displacement, and to compute the optimized strut for every displacement up to 30 mm in 0.1 mm increments (e). It reveals that the optimized struts provide significantly higher energy absorption past displacements of 4 mm, where they reach a factor of 20 when compared to conventional single-material struts. [Scale bars = 1 mm.]

the materials and layer diameters. For displacements smaller than 4 mm, the energy required to deform the strut is the same for the brittle and optimized core-shell struts (Figure 3.3e, center). Past displacements of 4 mm, the energy absorption of the brittle strut rapidly drops to 0 J, indicating catastrophic failure. The energy absorption of the optimized strut starts dropping at 4 mm, eventually reaching 0.4 J at a displacement of 10 mm, and turning upward past that point, approaching the continuously increasing energy absorption of the flexible strut. The ratio of the optimized strut's energy absorption to the energy absorption of the best-performing single-material strut (En. Abs. Ratio) peaks at 4 mm, right after failure of the brittle strut (Figure 3.3d, bottom). At this displacement, the optimized strut absorbs 20 times more energy than the flexible strut, which is the only option that does not fail. The energy absorption ratio approaches one as the core-diameter of the optimized strut drops to 0 mm towards larger displacements.

The model is also applied to typical engineering materials with brittle, ductile, and flexible characteristics (Figure 3.4a). Similarly to Figure 3.3e, the energy absorption of single-material struts composed of these materials is plotted and compared to that of the optimized struts (Figure 3.4a, top/center). As before, there is no difference between the optimized and most brittle struts (FR Epoxy) at displacements <1 mm. This is also seen in the energy absorption ratio plot (Figure 3.4a, bottom). At a displacement of 1 mm, the curve has a local maximum, and falls past 1 mm to approach the next most brittle material's curve. This trend repeats with each added material, showing that more materials are advantageous for the energy absorption. The amount of added energy absorption depends on the specific materials.

For a 4 mm outer diameter, two examples show what happens at displacements of 10 mm and 20 mm (Figure 3.4b and Figure 3.4c). For the 10 mm displacement, the best single-material option is PA12, as it absorbs the most energy among all materials that do not fail at this deflection. PA12 is ductile and often used in energy absorbing applications [188]. FR Epoxy, PEEK, PC, and POM possess failure strains smaller than required for the 4 mm outer diameter, but absorb more energy at smaller deflections. They can therefore be used as core layers with smaller diameters to increase the total energy absorption (Figure 3.4b). The energy absorptions of the PA12 and optimized strut relate to 0.19 J and 0.28 J, respectively, which is a factor of 1.5 more for the optimized strut. For the 20 mm displacement, the only material option that does not fail is a flexible thermoplastic polyurethane (TPU). In this case, optimizing the material

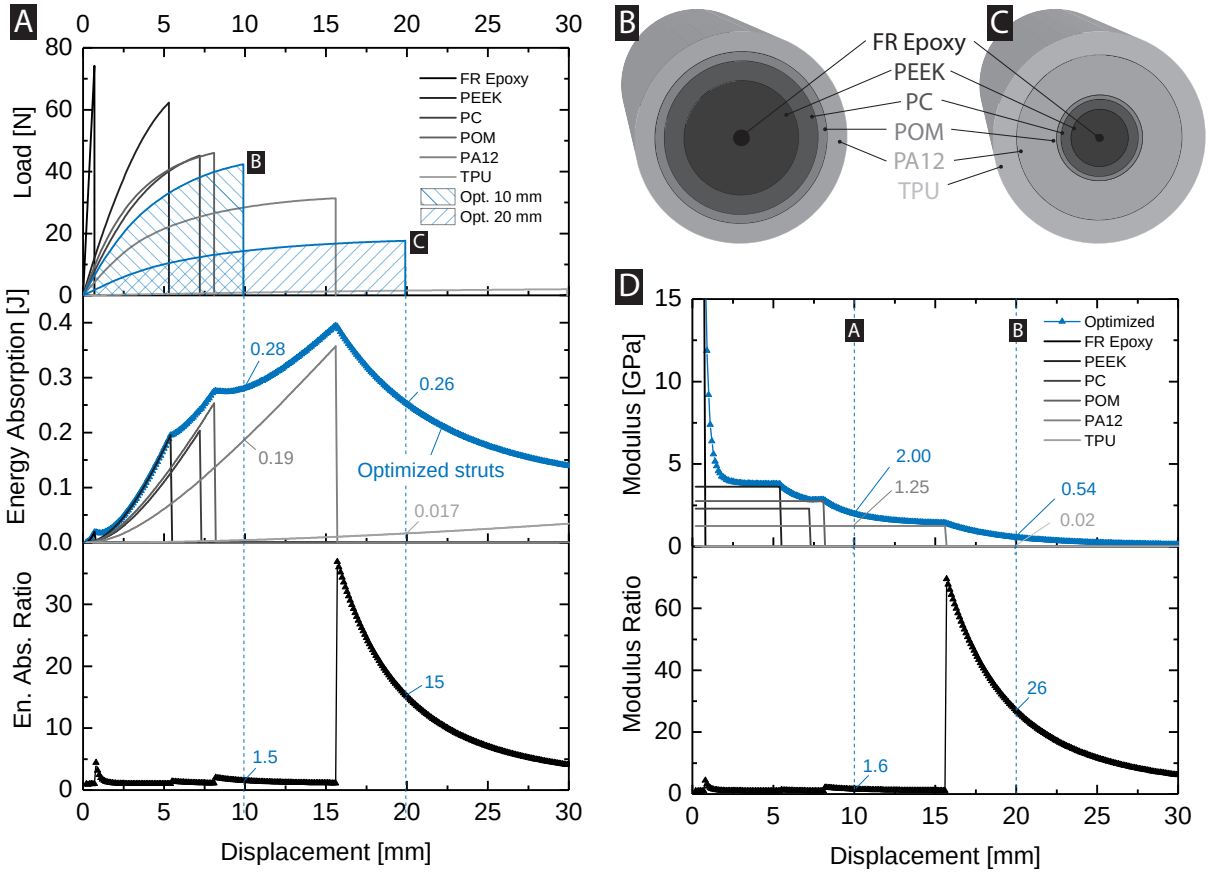

FIGURE 3.4: Struts – Expansion of the design space. Typical engineering materials are chosen to demonstrate the capability of the presented mechanism. Similarly to the two-material struts, the model is used to compute the optimized strut for every 0.1 mm displacement increment, up to a displacement of 30 mm (a). A significantly higher energy absorption can be reached when compared to the best single-material option. Two examples, optimized for displacements of 10 mm (b) and 20 mm (c), show that the increase strongly depends on the desired displacement, but is significant even when a single-material option exists that possesses exactly the required strain. The mechanism also increases the modulus up to 70 times when compared to the conventional strut (d). The outer strut diameters are 4 mm.

distribution to maximize the energy absorption yields a factor of 15. In the extreme case of the strut optimized for a displacement of 16 mm, the factor goes up to 42. Comparing the moduli of the single-material struts to the optimized struts, the difference is even larger (Figure 3.4d). At the given examples of 10 mm and 20 mm deflection, moduli ratios of 1.6 and 26 are reached, respectively. The modulus ratio peaks at a displacement of 16 mm reaching 70.

3.3.2 *Unit cells*

Next, bending dominated unit cells are fabricated from flexible (Figure 3.5a), core-shell (Figure 3.5b), and brittle struts (Figure 3.5c). The core-to-shell ratio for maximum energy absorption for an example displacement of 8 mm is computed to be 0.6. When tested in compression, the flexible cell deforms to the maximum set displacement without fracturing (Figure 3.5d). As predicted, the core-shell cell shows an initial failure at 8 mm, but continues sustaining load until the maximum displacement is reached (Figure 3.5e). The brittle cell shows an initial failure at 2.1 mm displacement and fails catastrophically at 3.6 mm. This behavior is also reflected in the load-displacement diagrams of the tests (Figure 3.5g). The brittle cell is the stiffest and strongest, reaching a load of 220 N, but fails catastrophically at 3.6 mm. Up to this displacement, it absorbs the most energy (0.47 J). The core-shell cell does not fracture and absorbs 0.38 J energy in total, which is slightly lower than that of the brittle cell, but 38 times more than the flexible cell, which absorbs 0.01 J, and which is the only option in this set-up that does not fail before the required displacement is achieved. When increasing the range to the total displacement of 45 mm, the introduced mechanism continues to work past the first failure at 8 mm (Figure 3.5h). The core-shell cell absorbs 1.64 J in total, which is 3.5 and 8.2 times more than the energy absorptions of the brittle (0.47 J) and flexible cells (0.20 J), respectively.

3.3.3 *Lattice structures*

Similarly, lattice structures composed of 3x3x3 unit cells are fabricated and tested in compression (Figure 3.6a-f). The unit cells in the lattice are half the size of the individually tested ones and have similar strut dimensions. With the same core-to-shell ratio, initial failure is expected at 4 mm. The flexible lattice deforms uniformly to the maximum deflection of 60 mm without noticeable failure (Figure 3.6d). First failure in the core-shell lattice occurs between 0 mm and 15 mm, starting at the bottom layer. The remaining layers fail consecutively and the lattice maintains the load across a broad range of displacements. In the brittle lattice, each layer fails catastrophically, creating a temporary gap between the cross head and the lattice. This is also observed in the load-displacement graphs (Figure 3.6g,h), where multiple peaks occur with

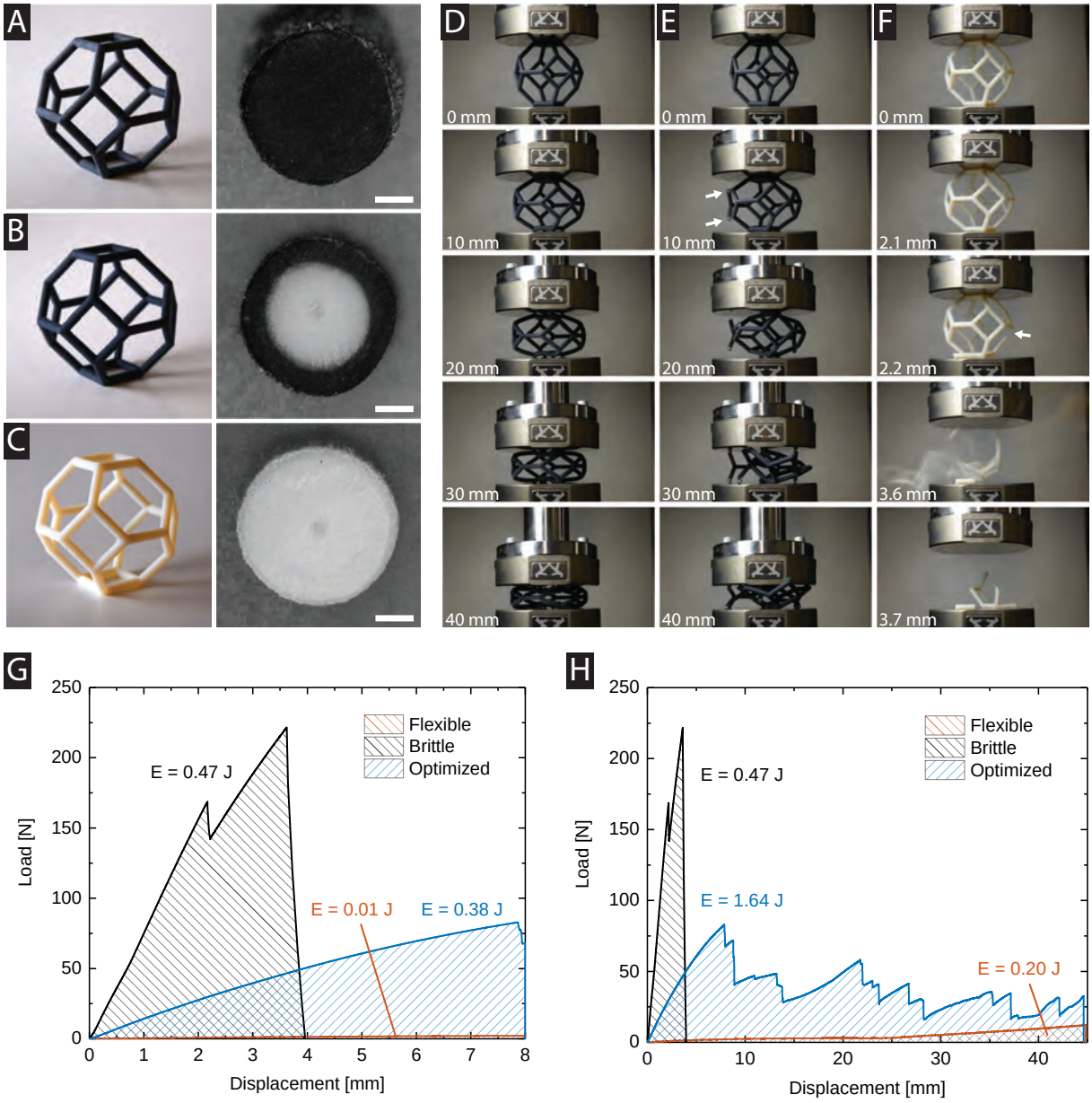

FIGURE 3.5: Unit cells. Experiments are conducted to examine the applicability and performance of struts in a unit cell. Bending dominated Voronoi unit cells [189] with core-shell struts of 4 mm diameter, designed for a maximum deflection of 8 mm, are compared to brittle and flexible single-material unit cells (a,b,c). Visual inspection shows that the flexible cell deflects up to 40 mm without fracturing (d). The core-shell begins to fail at 7.9 mm (e), whereas the brittle fails at 2 mm (f). The same can be seen in the load-displacement graphs, where the core-shell unit cell absorbs significantly more energy than the flexible strut cell, which is the only single-material option that can deflect this far (g). The core-shell cell does not fail catastrophically, which is the case for the brittle unit cell, and continues to absorb significantly more energy than the flexible single-material option past failure (h). [Scale bars = 1 mm.]

zero loads in between. For the designed displacement of 4 mm, the brittle lattice absorbs 3.04 J, but fails at 1.9 mm, well before the required displacement (Figure 3.6g). The core-shell lattice fails at 4.1 mm and absorbs 3.38 J – 22.5 times more than the flexible with 0.15 J at this dis-

placement. Considering the total displacement, the core-shell absorbs 25.32 J, which is double that of either single-material strut (Figure 3.6h).

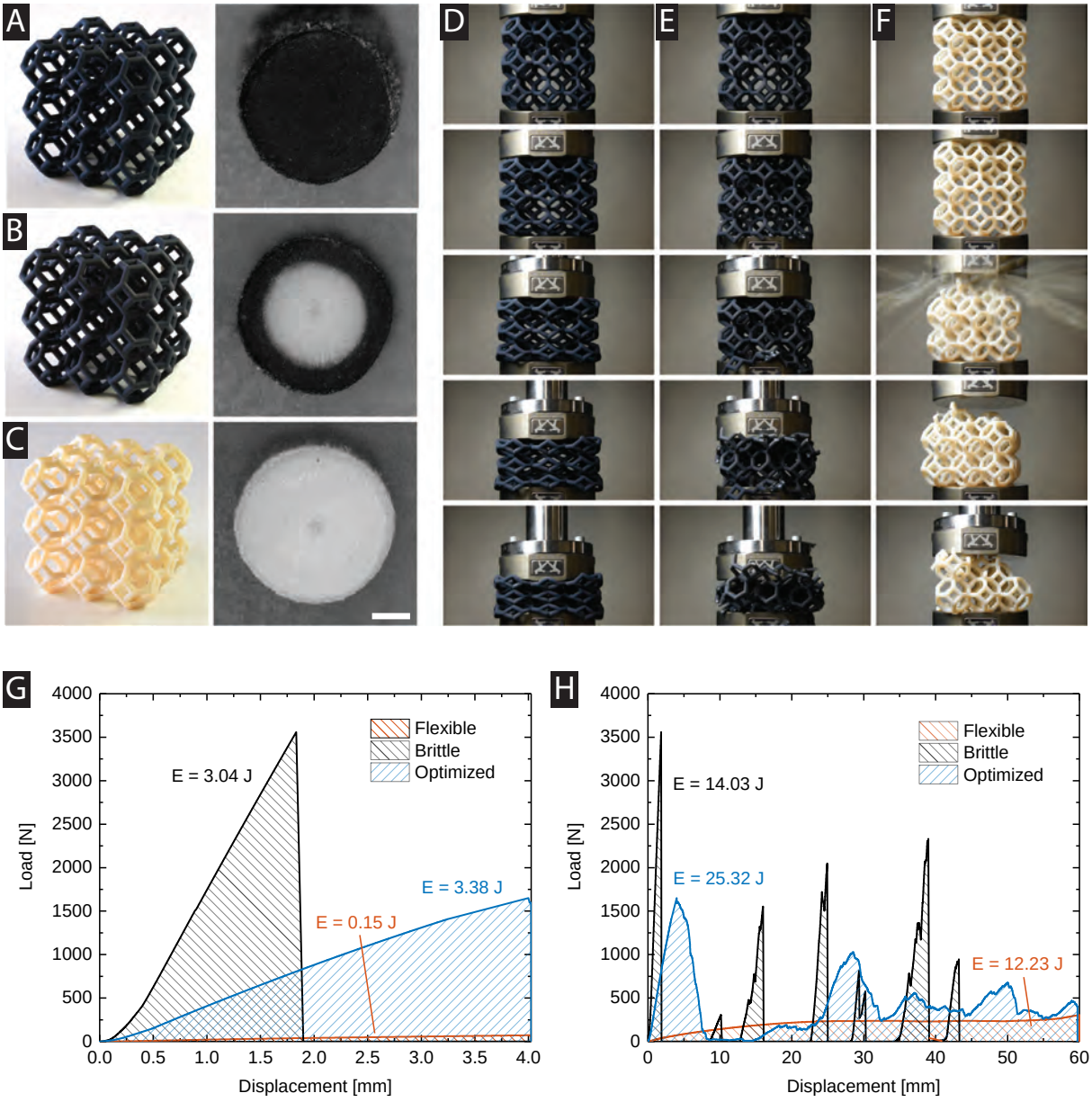

FIGURE 3.6: Lattice structures. Lattices designed for a displacement of 4 mm are assembled from the same struts as in Figure 3.5 (a,b,c). Visually, the flexible lattice shows no sign of failure (d). In the core-shell cell, first failure occurs at a displacement of 4 mm (e). The brittle lattice fails at 1.9 mm displacement (f). Quantitatively, the load displacement curves show a significantly higher energy absorption for both the designed displacement range (g) and the total range tested (h). [Scale bars = 1 mm.]

3.4 DISCUSSION

Similarly to the results, the discussion is sectioned into individual struts, unit cells, and lattices, which are presented in the same order.

3.4.1 *Individual struts*

Good agreement is found between the experiments and the model for both the single-material and core-shell struts. However, the model underestimates the failure strain for smaller core-to-shell ratios, i.e. they fail later than expected. This is surprising as the brittle core, which is assumed to be responsible for the failure, is geometrically identical to the single-material struts (Figure 3.3c). There is no drop in the load-displacement curve, indicating that the core stays intact beyond the prediction, rather than breaking and being carried on by the shell. The underestimation of the simulation values is advantageous from a safety and validity perspective, as the actual increases in energy absorption are likely to be higher than predicted.

As before, these results show that the core-shell struts can reach a significantly higher energy absorption than the single-material struts (Figure 3.3e, Figure 3.4d). The highest increase is reached at a displacement right after an available material disqualifies for a prescribed displacement. The increase is smaller, but still significant when a single-material is available that sustains exactly the required displacement. A larger number of available materials can only improve the result, but never worsen it. It is also favorable to have materials that are equally spaced in their fracture strains to create small gradient steps in the cross section.

The approach is also complementary to traditional systems, as the materials could now be optimized for each individual layer, rather than for a single-material strut. Another advantage is the independence of scale, as it is an architectural principle rather than a material property. The principle should also work for completely different architectures, where not all parts of the same material are equally strained, hence inefficiently used.

3.4.2 *Unit cells and lattice structures*

Both the unit cells and lattices show a similar trend as the struts, confirming that the hypothesis of scaling across hierarchies is valid. As different stress-strain states occur in the more complex structures, different struts fail at different displacements, even when in symmetry. This increases the complexity, but is also an advantage as it enables the structure to continue sustaining load past the initial failure. The degree and type of the failure are mostly governed by the core-to-shell ratio of the strut, ranging from no fracture at ratios of zero, to complete catastrophic failure at ratios of one. This allows the structures to be individually programmed for a specific application.

Depending on the load case, the struts can also be optimized individually for different parts of the unit cells or lattice, and the strut's material distribution can be tuned along the length, for example with a thicker shell near the nodes. However, the nodal requirements may vary individually and range from flexible nodes (pin joints) as used in truss networks, to rigid nodes. In addition, interaction effects exist between the material, strut, unit cell, and lattice. Unit cells are often chosen based on the requirement of a lattice's minimum stiffness or strength for a given material that withholds the desired deformation. With the proposed mechanism, these properties increase, allowing the designer to select a different unit cell, e.g. more bending dominated than previously, allowing the system to absorb more energy also on a unit cell level.

3.5 CONCLUSIONS

To conclude, the scale-independent, architectural paradigm introduced has demonstrated increases in stiffness, strength, and energy absorption in cellular structures by factors ranging from one to 42. Through the focus on the strut level, the approach is independent of the unit cell and lattice type, therefore highly versatile and applicable to a wide range of applications. Based on the requirements, the struts can be designed for both static and dynamic applications, structures that are allowed to fail with a single incident (e.g. ski and bicycle helmets), and structures that are not supposed to fail with a single incident (e.g. football helmets, cars, and airplanes). Particularly, in volume or weight restricted environments, such as helmets

or packaging, it could dramatically increase safety or reduce cost and environmental impact through material reduction.

3.6 SUMMARY

Increasing a structure's energy absorption capability without reducing its stiffness or strength has been a long-standing task as numerous, impactful applications await. Particularly, in volume or weight restricted environments, such as helmets or packaging, it can have a substantial effect on safety, cost, and environmental impact. However, on a materials level, it is virtually impossible, as these properties are mutually exclusive. Here, a new, cellular metamaterial is proposed that can simultaneously increase these properties by a multiple. Enabled by multi-material 3D printing, radially layered struts are fabricated, each of which experiences a different strain. The material in each layer is optimized for maximum toughness and the experiments are validated experimentally. The approach is independent of the unit cell and applicable to a wide range of structures under static and dynamic load, with and without fracture.

4

CORE-SHELL TYPE II: FLEXIBLE CORE, BRITTLE SHELL

I think we could build a better one.

— William Edward Boeing

This chapter has been adapted from a manuscript published in *Advanced Materials*:

Mueller, J., Raney, J. R., Shea, K. & Lewis, J. A. Architected Lattices with High Stiffness and Toughness via Multicore–Shell 3D Printing. *Advanced Materials* (2018).

4.1 INTRODUCTION

Despite recent advances in the design and fabrication of lightweight materials [64, 111, 113, 120, 190–192], the ability to create architectures that possess both high stiffness and toughness remains an elusive goal as these properties are often mutually exclusive [10]. Natural materials overcome such limitations by combining different toughening mechanisms across multiple length scales. In bone, for example, fibrillary sliding occurs on the nanometer-scale, [36, 193] while crack bridging and deflection happen at length scales ranging from tens to hundreds of micrometers [12, 14]. Architected materials are an emerging class of matter in which the distribution of multiple materials (including porosity) is engineered for mechanical performance [72, 135, 149, 194]. To date, several periodic lattices have been fabricated with high specific stiffness and strength [72, 113, 160, 195], including honeycombs [120], woodpiles with solid [190, 196] and foam struts [64, 197], and octet-trusses with solid [198, 199] and hollow struts [104, 111, 113, 151, 159].

To enhance fracture toughness, energy absorbing mechanisms that increase the length over which a critical crack must propagate prior to failure are needed [51, 114]. For example, nacre, a natural composite with a brick-and-mortar architecture, exhibits high fracture toughness that arises when cracks are deflected around rigid aragonite ”bricks”, while being bridged by thin, compliant organic ”mortar” [200]. However, it is difficult to introduce this type of mechanism

into lattice architectures, since complex struts are challenging to build [10, 201]. While hierarchical lattices ($\sim$1 mm^3) composed of an octet truss geometry with octet truss-based struts have recently been constructed using 2-photon polymerization [191], those architectures are unable to confer both high stiffness and toughness [64, 191, 197, 202].

Here, a new method is reported for creating architected lattices composed of core-shell struts that are both stiff and tough. Specifically, these lattices contain orthotropic struts with flexible epoxy core – brittle epoxy shell motifs in the absence and presence of an elastomeric silicone interfacial layer. The effects of strut composition, i.e., core-shell (C-S) versus core-interface-shell (C-I-S), core-to-shell ratio (d/D), and interface thickness on their stiffness, strength, and fracture toughness are explored. These structures are produced by direct ink writing [83], an extrusion-based 3D printing technique, in which viscoelastic epoxy inks are deposited through a given nozzle in a layerwise manner and subsequently cured. To pattern the desired structures, multicore-shell printheads for coextrusion of coaxially aligned epoxy and silicone resins are designed and fabricated (Figure 4.1). The tapered nozzles are created in a reproducible manner using stereolithography, which ensures uniform flow of these inks without clogging (Figure 4.1, Figure 4.2).

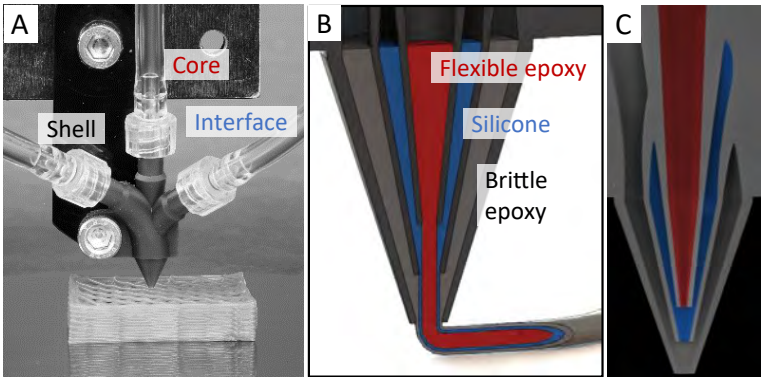

FIGURE 4.1: Multicore-shell nozzles. (a) Optical image of the coaxial printhead connected to the core, interface, and shell ink reservoirs. (b) Schematic cross sectional view of the core-shell printhead and (c) corresponding false-colored optical image of the core-shell nozzle from which the flexible epoxy core (red), elastomeric silicone interface (blue) and brittle epoxy shell (grey) inks are co-extruded.

The ink reservoirs are connected to the multicore-shell nozzle via a Luer lock that is directly fabricated with the nozzle. The inner channels of each printhead are retracted to decouple the minimum printable strut size from the number of input channels, therefore maximizing the feature resolution (Figure 4.3).

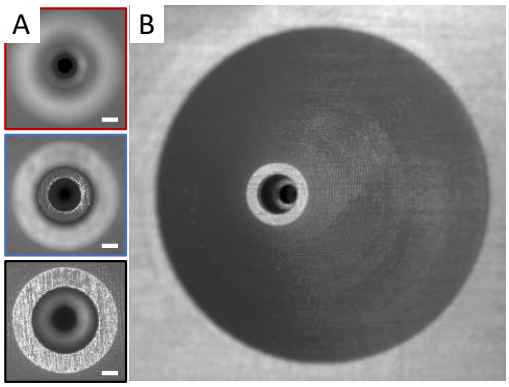

FIGURE 4.2: End-on views of the core-shell nozzles, in which the retracted inner channels enable higher resolution compared to conventional designs. [Scale bars = 200 μm.]

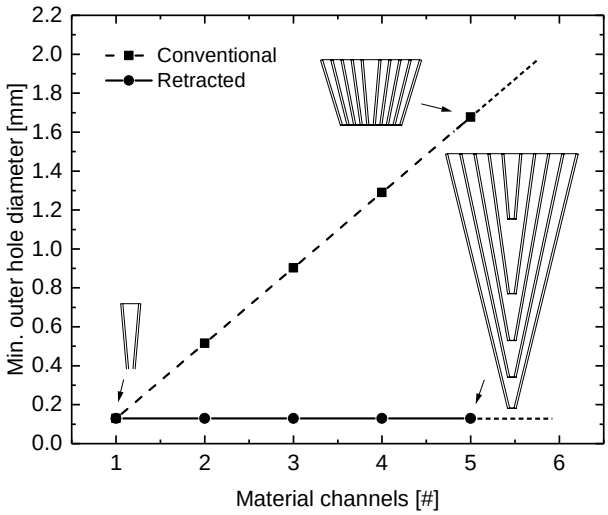

FIGURE 4.3: Outer nozzle diameter as a function of number of co-axial materials printed by these multi-core shell printheads, which demonstrates the advantage of the retracted design.

Importantly, the presented multicore-shell nozzles allow one to seamlessly switch individual input channels on and off, and thereby vary both the strut composition and geometry on demand, while maintaining a constant outer strut diameter (Figure 4.4).

Next, three viscoelastic inks based on flexible epoxy (core), brittle epoxy (shell) and silicone-based resins (interface) are developed for printing both individual architected struts as well as the desired 3D lattices. Each of these inks must exhibit shear thinning behavior to facilitate their flow through these nozzles under an applied pressure as well as an appropriate storage modulus, G', and shear yield stress, τ_y, to retain their extruded cylindrical shape after the C-S and C-I-S filamentary struts exit the nozzle. These requirements are identical for the single-material, C-S, and C-I-S struts. The flexible core ink is based on an epoxy resin (Epon 872) that contains both fumed silica (diameter < 1 μm, 18% by weight) and rubber particles

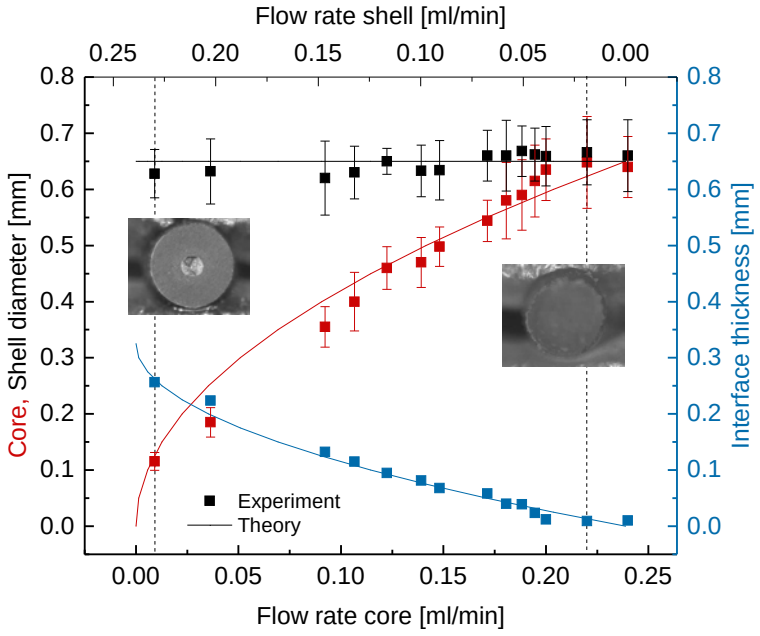

FIGURE 4.4: The multi-core shell printhead can systematically vary the core-to-shell ratio and interfacial layer thickness while maintaining the outer diameter of the printed filamentary struts.

(diameter = 150 nm, 4% by weight) that modify the ink rheology and increase the stiffness and fracture toughness after curing [203]. A difunctional primary amine (12% by weight) is used as the curing agent. The brittle shell ink is based on a different epoxy resin (Epon 826) that contains nano-clay platelets (10 nm length, 1 nm thickness, 45% by weight), which serve as a rheological modifier. In this ink, an imidazole-based ionic liquid (5% by weight) is used as a curing agent, which provides a long pot life (~30 days) [120]. Finally, the interfacial layer ink consists of a silicone elastomer (10:1 by weight ratio with the catalyst). The apparent viscosity and shear moduli of the core, shell, and interfacial layer inks are provided in Figure 4.5, respectively. Each ink is strongly shear thinning with an apparent viscosity of roughly 10^3 Pa·s at a shear rate of 1 sec^{-1}. Both epoxy-based inks exhibit nearly identical plateau storage moduli (G'~$2x10^4$ Pa) and shear yield stresses (τ_y~100 Pa), while the silicone-based ink exhibits G' and τ_y values that are roughly an order of magnitude higher. Importantly, the printed features remain structurally stable during initial curing at ~100°C for an extended time period (>15 h).

The stiff epoxy ink is confined to the outer shell, since the stiffness of these 3D printed lattices exhibits a strong power law dependence on strut diameter, $K \propto diameter^4$. The flexible epoxy ink is optimized such that the core exhibits both high energy absorption and compati-

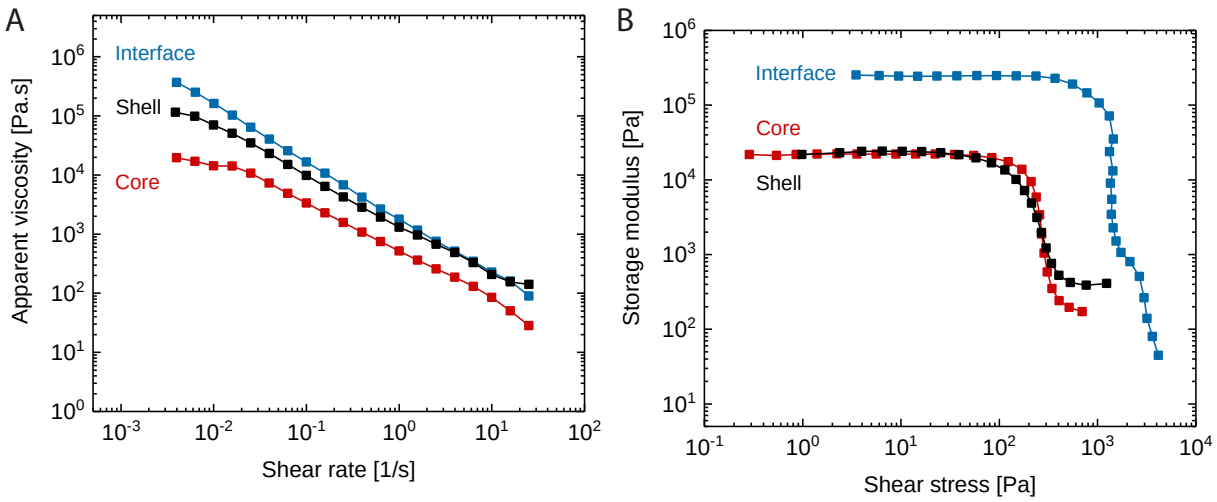

FIGURE 4.5: Log-log plot of apparent viscosity as a function of shear rate and storage modulus as a function of shear stress for the flexible epoxy core (red), elastomeric silicone interface (blue) and brittle epoxy shell (gray) inks, respectively.

bility with the shell material. To prevent catastrophic failure of the core, a fracture strain larger than the strain that occurs in every part of the structure is required (Figure 4.6a).

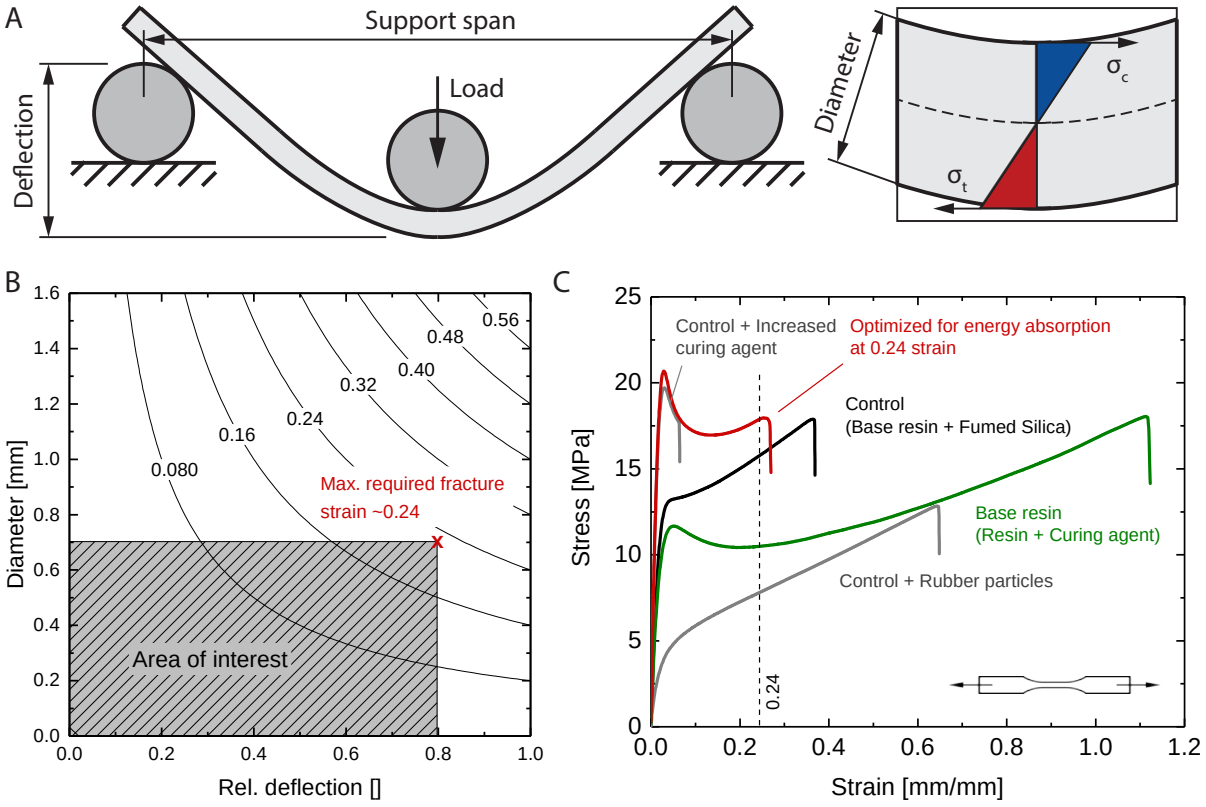

FIGURE 4.6: To prevent catastrophic failure, a specific fracture strain that is dependent on the diameter and deflection is required for the core material. (a) schematic view of three point bend test and corresponding stress profile across the strut. (b) calculated dependence of strut diameter on relative deflection for different values of fracture strain, which denotes that predicted value of maximum required fracture strain. (c) stress-strain behavior for different materials tested, including the optimized combination (denoted by the red curve) that maximizes the energy absorption for the computed strain of $\varepsilon = 0.24$.

However, the higher the fracture strain, the lower the stiffness and strength [12]. Hence, the fracture strain of the flexible epoxy core should only be marginally higher than the required minimum failure strain, ε_f. To determine this value, the maximum strut diameter, d, is fixed to 0.7 mm and uses a typical strut deflection, δ, in a bending dominated lattice of 80% of span length, L, before densification, as given by:

$$\varepsilon_f = \frac{6\delta d}{L^2}. \tag{4.1}$$

Since this equation does not consider non-linearities, the calculated minimum ε_f of 0.24 (Figure 4.6b) should be viewed solely as an approximation for the presented, experimental system.

4.2 METHODS

This section presents, in more detail, the procedure and experimental methods for the material development, the attainment of rheological data, the design and fabrication of multicore-shell printheads, the application of the printheads in direct ink writing, and the characterization of the resulting structures.

4.2.1 *Materials*

The flexible core and brittle shell epoxy inks are prepared by mixing batches of 10 g to 60 g of Epon 826 or Epon 872 (Momentive Performance Materials Inc., Waterford, NY, USA) with dimethyl methyl phosphonate or xylene (Sigma Aldrich, St. Louis, MO, USA) in "max 100" and "max 200" containers (FlakTek Ink, Landrum, SC, USA).

The nano-clay platelets (Nanocar 1.34 TN, Southern Clay Products, Inc., Gonzales, TX, USA), fumed silica (CAB-O-SIL TS-530, Cabot Corporation, Alpharetta, GA, USA), and rubber (Hypro 1300X8 CTBN Emerald Performance Materials, LLC, Vancouver, WA, USA) are added stepwise, followed by mixing in vacuum (20 Torr) in a DAC 600 VAC speed mixer after each step (90 sec at 800 rpm, 90 sec at 1600 rpm, and 120 sec at 2000 rpm, FlakTek). After allowing

the inks to cool to room temperature, the Basionics VS03 (BASF, Ludwigshafen, Germany) or Epikure 3230 curing agents (Momentive Performance Materials Inc.) are added and then mixed for 30 sec at 800 rpm, 30 sec at 1600 rpm, and 60 sec at 2000 rpm.

For the interfacial layer ink, SE1700 (Dow Corning, Midland, MI, USA) is mixed with the catalyst at a 10:1 ratio for 120 sec at 2000 rpm. A summary of the constituents used for each ink is provided in Table 4.1.

	Core	Interfacial layer	Shell
Epoxy resin (Epon 872)	100		
Untreated fumed silica	18		
Rubber particles	4		
Xylene	33		
Epikure 3230	12		
SE 1700		100	
SE 1700 Catalyst		10	
Epoxy resin (Epon 826)			100
Nanoclay			45
Dimethylmethylphosphonate			5
VS 03			5

TABLE 4.1: Composition of core, shell and interfacial layer inks.

The rheological properties of each ink are characterized under ambient conditions using a controlled-stress rheometer (Discovery HR3, TA Instruments, New Castle, DE, USA) equipped with a 40 mm flat parallel plate geometry. Prior to rheological characterization, all inks are prepared the same way as they are for printing and carefully placed on the plate using a spatula. For the flexible core and interfacial inks, a gap distance of 500 μm is used. For the brittle shell ink, a gap distance of 1 mm is used in addition to a solvent trap to prevent solvent loss. The rheological properties of both the base epoxy resins (Figure S3) and their corresponding ink formulations (Figure S4) are characterized by viscometry measurements, carried out over shear rates from 0.01 to 100 s^{-1}, and oscillatory measurements, carried out at a frequency of 1 Hz within the shear stress range of 0.1 to 3000 Pa.

4.2.2 *Fabrication of multicore-shell printheads*

The printheads are fabricated on an Aureus Plus 3D printer using HTM140 material (EnvisionTEC, Dearborn, MI, USA) with a layer height of 50 μm and an X-Y resolution of 43 μm

(Figure 4.7a). The size of the platform allows printing of up to six printheads simultaneously, drastically cutting down the fabrication time compared to manual fabrication and assembly (Figure 4.7b) [204].

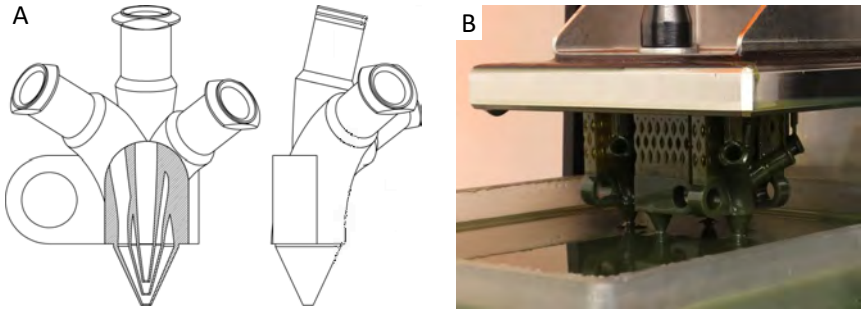

FIGURE 4.7: Schematic front and side views of the printhead design with a cut in the center (a). The dimensions of the outlets are 500 μm, 600 μm, and 800 μm for the core, interfacial layer, and shell, respectively. (b) These printheads are fabricated using stereolithography (SLA) and an acrylic based HTM140 resin (EnvisionTEC, Dearborn, MI, USA).

The printheads are also analyzed for minimum feature sizes by designing individual holes and walls similarly to those of the printhead (Figure 4.8). Hole diameters ranging from 86 μm to 301 μm in increments of the printer resolution, i.e. 43 μm, are fabricated (Figure 4.8a). The smallest hole is clogged, yielding a minimum printable hole diameter of 129 μm. The remaining holes show a positive, average deviation in measured diameter of 12 μm when compared to the designed diameters. In addition, wall thicknesses, mostly relevant for the inner channels, are fabricated in thicknesses ranging from 43 μm to 129 μm, in 21.5 μm increments, i.e. half the printer's resolution (Figure 4.8b). Walls with a thickness of 43 μm are not built, yielding a minimum wall thickness of 64.5 μm for all tested print angles. When compared to the designed values, the measured wall thicknesses are, on average, 30 μm smaller. The smallest wall thickness measured is 22 μm at a vertical angle of 0 deg. (Figure 4.8b). Note that the printer can only fabricate in its native resolution, but, in particular, for circular features, the aliasing process in the software has a major effect on which pixels are occupied.

4.2.3 *Multicore–shell 3D printing*

The core, shell, and interfacial inks are loaded into Luer lock syringe barrels of 10 ml or 30 ml (Nordson EFD, East Providence, RI, USA) and centrifuged for eight minutes at 2200 rpm to remove the bubbles from the ink. The multicore-shell printhead is mounted on an

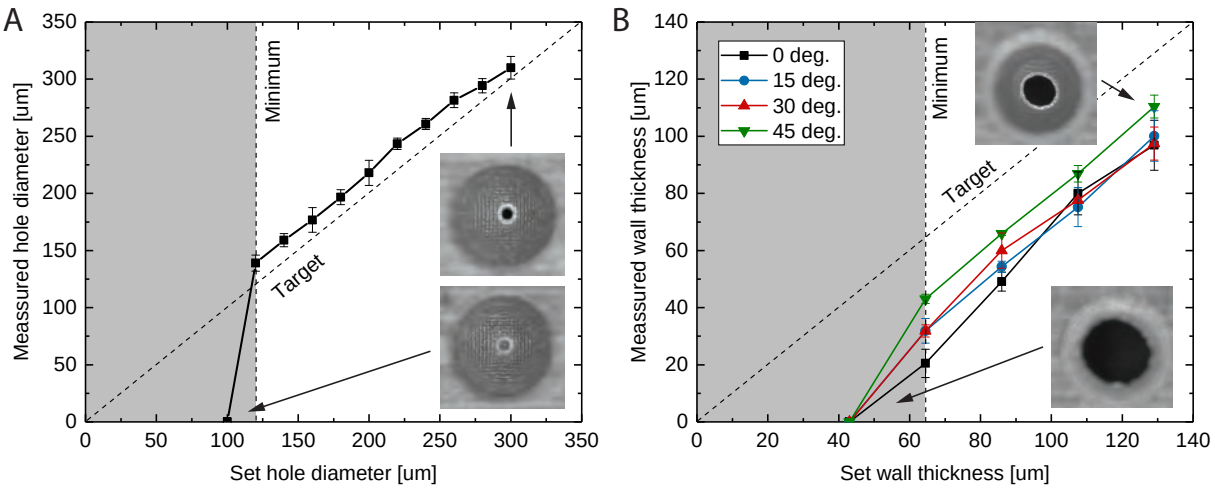

FIGURE 4.8: Minimum printable hole size (a) and wall thickness (b) that can be achieved. The dashed lines show the theoretically expected values.

Aerotech 3-axis stage (Aerotech, Inc., Pittsburgh, PA, USA), and connected to the loaded syringes through the Luer locks. Ink extrusion is controlled by an Ultimus V pressure pump (core, Nordson EFD), a PHD Ultra syringe pump (interfacial layer, Harvard Apparatus, Cambridge, MA, USA), and an Ultra 2800 positive displacement dispenser (shell, Nordson EFD). All printed and tested structures are cured sequentially for 1 h at 80^{o}C, 15 h at 100^{o}C, and 1 h at 220^{o}C.

4.2.4 *Characterization*

The dimensions of the printed structures are measured with a VHX-2000 optical microscope and a VH-Z20R 20x-200x optical zoom lens (Keyence, Osaka, Japan), which is calibrated before each session. The mechanical properties are measured on an Instron 5566 Universal Testing Machine with a constant crosshead speed of 10 mms-1 (Instron, High Wycombe, United Kingdom). For the struts, a 10 N static load cell is used, while a 1000 N static load cell is used for the lattice structures and tensile tests. The struts are tested in three point bending according to the ASTM D790-10 standard test method for flexural properties of unreinforced and reinforced plastics with a support span of 15 mm and support diameters of 2 mm, on a custom-built test rig. The lattices are tested in compression using polished steel plates to minimize friction. Tensile tests are performed on "Type V"-sized specimens according to the ASTM D638-10 standard test method for tensile properties of plastics. The displacement is

measured with an Advanced Video Extensometer (Instron). The reported properties represent a mean of at least three samples.

4.3 RESULTS

First, results are presented for the material optimization of the core. While the requirement on the shell material is simply to be as brittle as possible, the core material is optimized for maximum toughness at a given strain. Second, individual core-shell struts are printed, tested in three point bending, and compared to conventional struts of either base material. Third, core-shell lattices are fabricated and compared to conventional lattices of flexible and brittle materials.

4.3.1 *Material optimization*

The mechanical properties of the epoxy materials are quantified by fabricating dogbone specimens and subjecting them to tensile testing. The effects of a broad range of fillers on their mechanical performance are shown in Figure 4.6c. Specimens composed of the base resin (pure resin with curing agent) exhibit an elastic modulus of 0.6 GPa, a tensile strength of 12 MPa, and a fracture strain of 1.1. Upon adding fumed silica or increasing the curing agent, both their stiffness and strength is increased, while their fracture strain is reduced. By contrast, the addition of rubber particles reduces each of these properties. By adjusting the filler composition and relative ratios, a flexible epoxy ink is produced with the requisite fracture strain of 0.26, which maximizes the energy absorption through a (relatively) high stiffness and strength of 1.25 GPa and 22 MPa, respectively.

4.3.2 *Individual struts*

Individual struts are printed, composed of the brittle shell-flexible core epoxy in the absence and presence of the elastomeric interlayer. Their mechanical properties are characterized in three point bending to isolate boundary effects. The interfacial layer thickness (average value

= 34±18 μm) is kept as thin as possible while ensuring reliable separation of the core and shell. It is found that the C-S struts fail completely upon crack formation, while the C-I-S struts remain partially intact (Figure 4.9).

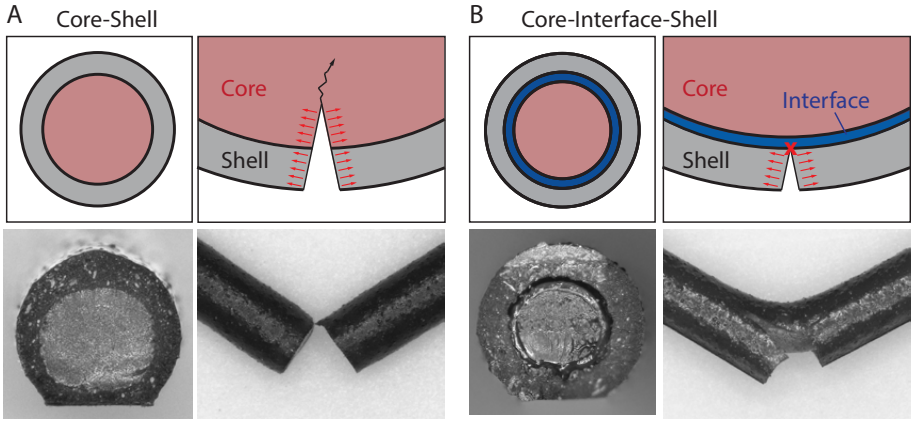

FIGURE 4.9: Schematic illustrations of the core-shell and core-interface-shell struts (cross sectional and side views), which shows that the elastomeric interfacial layer mitigates crack propagation from the brittle epoxy shell to the flexible epoxy core. [Scale bars = 200 μm.]

Next, C-S struts of varying core-to-shell ratios are fabricated and their mechanical behavior is compared to struts made from the individual epoxy materials as well as to the C-I-S struts (Figure 4.10a-c). It is found that both the pure brittle epoxy strut (d/D = 0) and the C-S struts fail completely (Figure 4.10a left, Figure 4.10b). By contrast, the flexible epoxy remains intact both in the pure flexible epoxy strut (d/D = 1, Figure 4.10a right) and C-I-S struts (Figure 4.10c). Importantly, the C-I-S struts fail in qualitatively different ways depending on the ratio d/D: e.g., when d/D = 0.4, the crack travels straight through the brittle material (Figure 4.10c left), while when d/D = 0.85, the crack is deflected and bifurcated multiple times (Figure 4.10c right, Figure 4.10d).

Since C-S struts are expected to have some interdiffusion between layers, nano-indentation is used to measure the transition region between the brittle and flexible phases (Figures 4.11). The brittle epoxy shell is mostly unaffected, while the flexible epoxy core exhibits an increased stiffness near the interface that linearly decreases towards the value of 1.3 GPa for the pure material at a distance of ∼400 μm from the interface.

Figure 4.12 highlights representative load-displacement curves obtained for individual struts of varying composition and core-shell (d/D) ratios, while Figure 4.13 shows the full set of effective modulus, ultimate tensile strength (UTS) and energy absorption data obtained

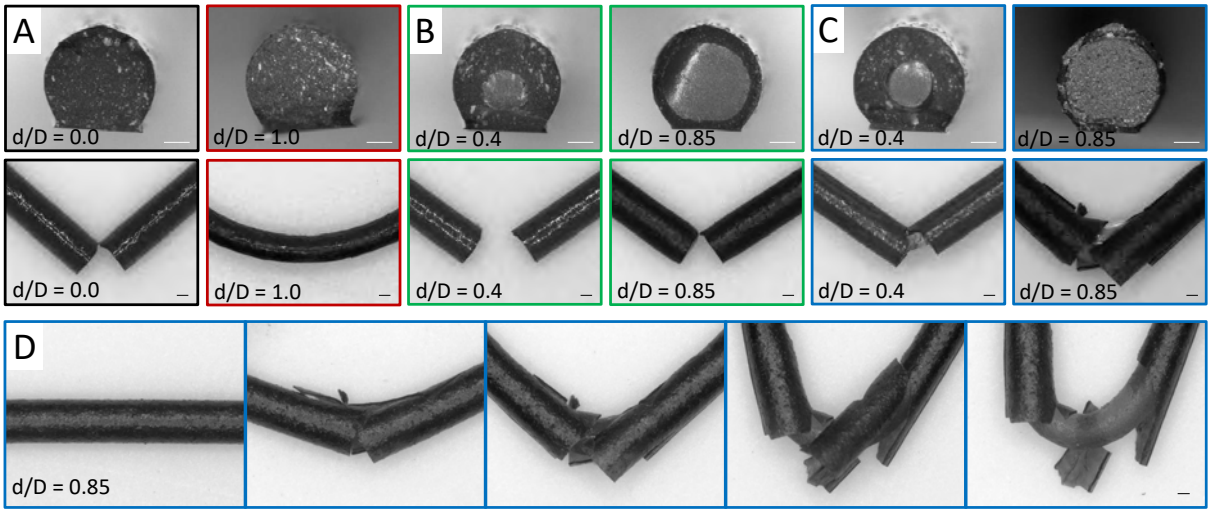

FIGURE 4.10: Fracture behavior of individual struts. (a) A brittle and elastic behavior is observed for struts composed solely of the shell and core materials, respectively. (b) While the core-shell (C-S) struts also fail from brittle fracture, (c) the core-interface-shell (C-I-S) struts are able to stop the crack propagation into their core. The shell layer of struts with a small core (left) fails completely, while those with a large core fail piecewise. (d) A sequence of the crack propagation in a C-I-S strut with increasing strain from left to right. [Scale bars = 200 μm.]

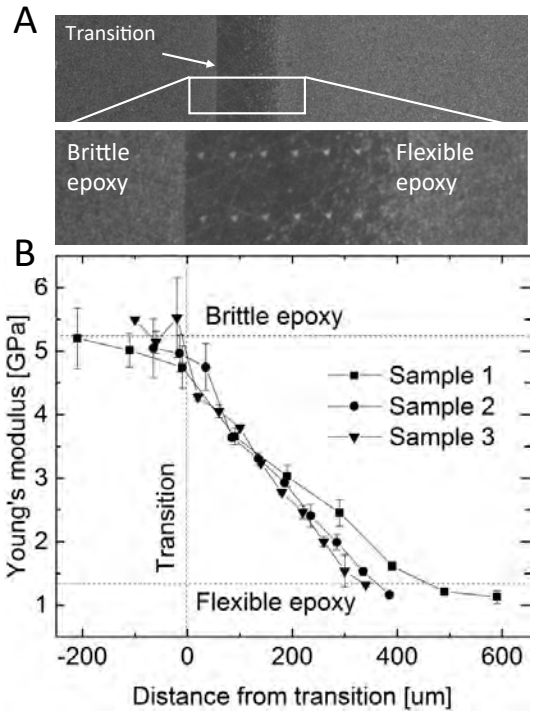

FIGURE 4.11: In the absence of the interfacial layer, diffusion occurs between the core-shell epoxy layers during printing and curing, as reflected by graded interfacial zone (~400 μm thick) and corresponding decrease in Young's modulus from the brittle epoxy shell to the flexible epoxy core.

for these struts with d/D values from zero to one, i.e., from purely brittle to purely flexible epoxy, respectively.

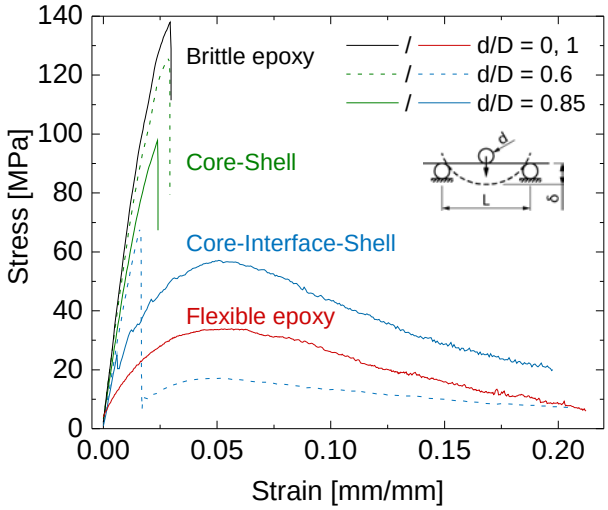

FIGURE 4.12: Load-displacement response for representative struts of varying composition and core-shell (d/D) ratio.

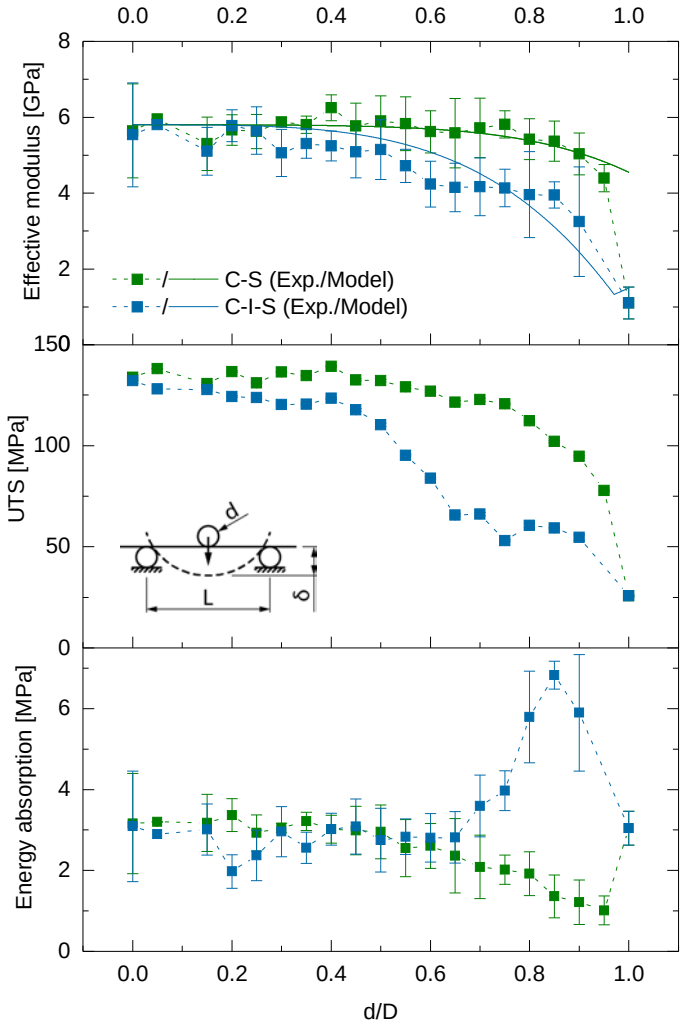

FIGURE 4.13: Plots of effective modulus, ultimate tensile strength (UTS) and energy absorption measured for individual C-S and C-I-S struts of varying d/D ratio, which reveals the pronounced rise in energy absorption for C-I-S struts with a d/D ~0.85.

The modulus, calculated by a least-squares fit of the initial slope of the stress-strain curves, for both the C-S and C-I-S struts initially plateaus at around 6 GPa, close to the value measured for the brittle epoxy. As d/D increases to ~0.85, the modulus of the C-S struts remains nearly constant, while that of the C-I-S struts decreases to approximately 4 GPa. Notably, as the d/D ratio increases, there is a concomitant increase in cross sectional area of the interfacial layer. Importantly, there is good agreement with the measured values, when these effects are included in the beam theory for the flexural modulus:

$$E_f = \frac{FL^3}{48\delta I} \tag{4.2}$$

where F is the load, L the span length, δ the deflection, and I the second moment of area of the cross section. In Equation 4.2, the second moment of area, I, for a rod with circular and ring cross sections of outer radius, R, and inner radius, r, is given by:

$$I_{circle} = \frac{\pi}{4}R^4, \quad I_{ring} = \frac{\pi}{4}(R^4 - r^4) \tag{4.3}$$

Using I for the core, shell, and the total filament allows one to calculate the combined Young's modulus for each core-to-shell ratio as given by:

$$E_{comb} = \frac{I_{core}E_{core} + I_{shell}E_{shell}}{I_{comb}} \tag{4.4}$$

The larger deviations observed for the C-I-S struts are due to additional measurement, analysis, and rounding errors. For the ultimate tensile strength (UTS), the trend is similar, i.e., the plateau value of both types of struts is ~135 MPa at d/D = 0, while values of ~100 MPa (C-S strut) and ~60 MPa (C-I-S strut) are observed at d/D = 0.85. The energy absorption of the C-S and C-I-S struts is affected by their respective modulus and UTS values at a given d/D. When $0 \leq d/D < 0.6$, there is little difference in energy absorption (~3 MPa) observed between the two types of struts. At d/D = 0.6, the energy absorption of the C-S and C-I-S struts is still similar, despite the lower stiffness and strength of the latter. When d/D > 0.6, the increasing influence of the flexible core reduces the total stiffness and strength of the C-S struts and hence their energy absorption. Upon initiation, the crack travels through the entire strut, even those with large cores (Figure 4.10b). By contrast, the opposite effect is observed for the C-I-S

struts at $d/D \geq 0.6$. Importantly, when $d/D \sim 0.85$, their energy absorption more than doubles above the base value of 3 MPa since their shell now fractures in a piecewise manner, as seen Figure 4.10c.

4.3.3 *Lattice structures*

To create 3D architected lattices, direct ink writing is used to produce bending dominated woodpile structures [205] composed of either spanning C-S and C-I-S struts. As controls, 3D lattices composed of pure brittle and flexible epoxy struts are printed (Figure 4.14).

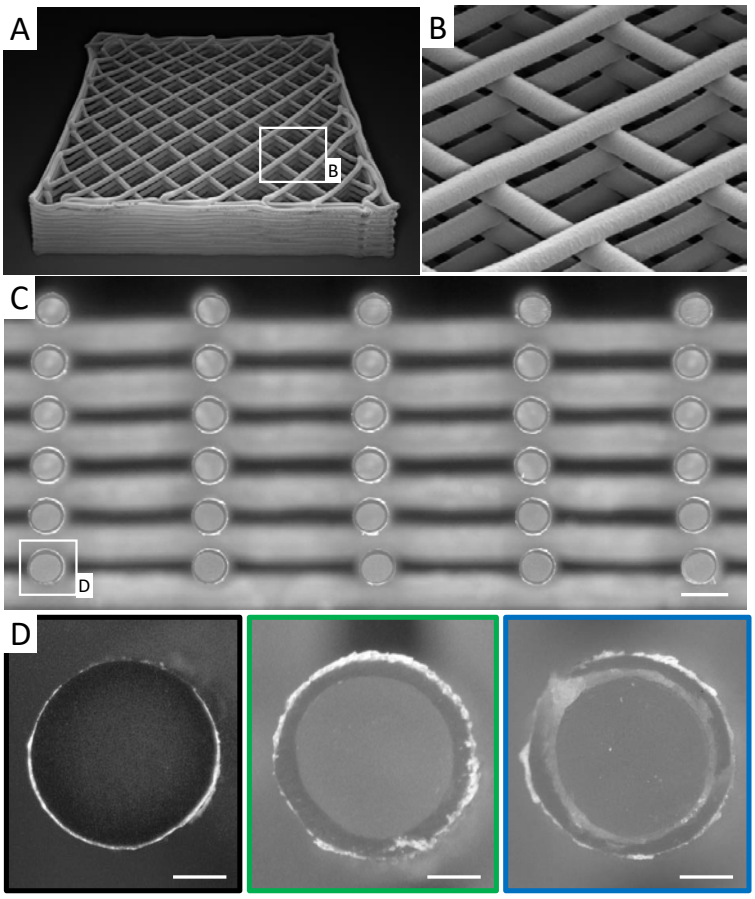

FIGURE 4.14: (a-c) optical images of a representative lattice fabricated by multi-core shell direct ink writing, where (a) tilted view of the entire lattice, (b) closer view of printed struts, which span gaps across underlying features within the lattice, and (c) cross sectional view of the lattice composed of C-I-S struts [scale bar = 1 mm]. (d) higher magnification images of exemplary brittle (black – left), C-S (green – center), and C-I-S (blue – right) struts [scale bars = 0.2 mm].

Solid walls are printed to provide structural stability during the printing and curing process. However, the walls are removed after curing to avoid boundary effects during mechanical

loading. All lattices are compressed and the results normalized by their relative density. In the C-I-S lattices, layers fail along one diagonal first, followed by the collapse of the inverse diagonal layers (Figure 4.15a). As before, the shells fracture into pieces while the core remains intact (Figure 4.15b). Unlike the C-I-S-based lattices, both the brittle epoxy and C-S lattices fully collapse (Figure 4.15c), releasing enough energy to catapult them out of the testing apparatus. By contrast, the flexible epoxy lattices do not fail catastrophically and exhibit global out-of-plane buckling when the $\varepsilon \geq 0.3$. Importantly, the C-I-S lattices demonstrate superior energy absorption capabilities. Similar to the data obtained for individual struts, the modulus of the C-I-S lattices is slightly lower relative to the brittle epoxy and C-S lattices, though significantly higher than that of the flexible epoxy lattices.

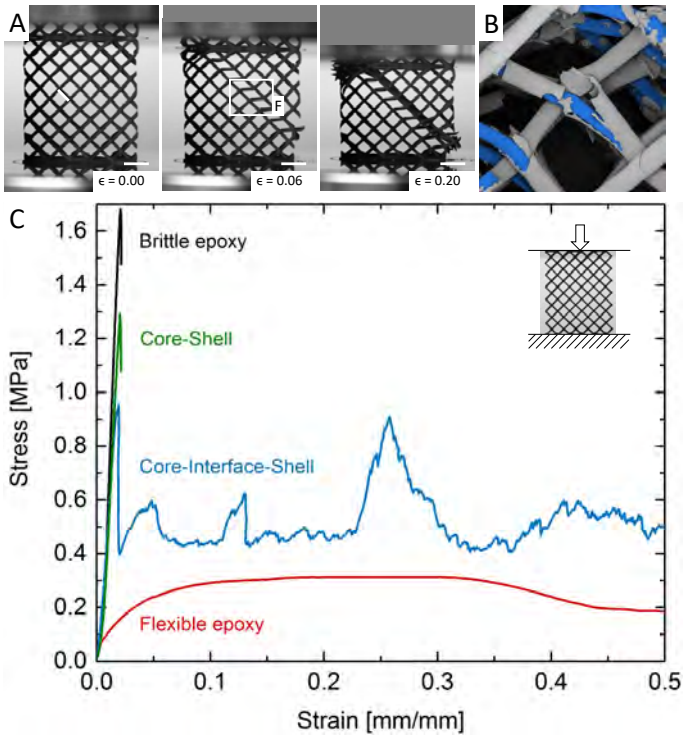

FIGURE 4.15: (a) optical images of a C-I-S lattice under different compression states that show a layer wise failure, typical for elastoplastic materials of this unit cell type [scale bars = 8 mm]. (c) stress-strain curves for the previously shown C-I-S lattice compared to lattices composed of brittle epoxy, flexible epoxy, and C-S struts, as shown in 4.14. (b) the interfacial layer stops crack propagation through the strut cores (false-colored blue), causing the shell to fracture into many pieces.

4.4 DISCUSSION

First, the design and fabrication of the printhead is discussed and conclusions are drawn on the enabling features. Then, the findings of the different experimental tests using the printhead are discussed. Namely, the core material, the individual struts, and complete lattice structures fabricated from these struts.

4.4.1 *Multicore-shell printhead design and fabrication*

The probably most important step toward fabricating the presented structures and validating the mechanisms is the development of the multicore-shell printhead, where particularly two features are critical to the outcome: the design and the fabrication.

As shown in Figure 4.3, the outer diameter in conventional core-shell printhead designs depends mainly on the number of material channels. Decoupling the number of input channels from the outer diameter is crucial for printing small-scale structures and enables architectures that are of practical use, rather than printing large prototypes as proofs of concept.

The retraction of the inner channels also increases the print quality and reduces the set-up time. Large gaps between the nozzle and filament, and an unequal filament length affects especially the start of the print (Figure 4.16). However, it is also linked to a large offset of the filament from the center of the nozzle once it exits the nozzle. The schematic shown in Figure 4.16a shows a horizontal nozzle set-up with a condition that also applies when the nozzle is vertical, due to pulling of the filament. During printing, this filament offset can negatively affect the print quality, particularly near curves and turns. The gaps in the new design are inside the nozzle and filled with material (Figure 4.16b). As the outer diameter of the nozzle is now identical to that of the filament, given that the velocity of the printhead is aligned with the extrusion speed, the filament of all channels is of equal length and no offset occurs between the filament axis and the nozzle axis.

As a result of these improvements, one printhead can be used to print almost arbitrary core-to-shell ratios and change these ratios on the fly, during printing. While this significantly reduces the turnover time of print jobs, it also enables additional design features. As such, the

ratios can be optimized to the specific, local requirements of the structure or material channels can be switched on and off, which might be important, for example, for active materials.

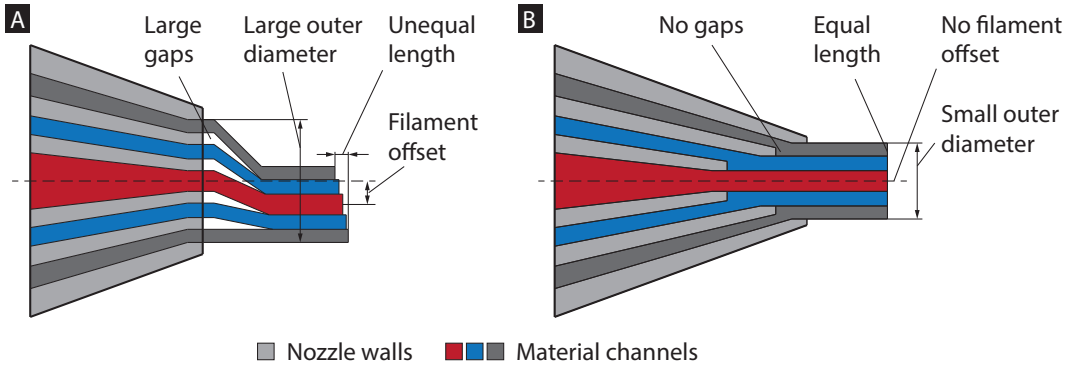

FIGURE 4.16: Conventional core-shell nozzle design (a) and improved design (b). The schematics show material exiting the nozzle of a printhead, forming a multicore-shell filament.

The other crucial advancement is moving from manual fabrication and assembly to 3D printing of the printheads. One big advantage is that the minimum wall thickness can be drastically reduced from that of available standard parts to the resolution of the 3D printing process. At the same time, the channel alignment can be as high as the resolution of the printer, potentially orders of magnitude higher than what can be achieved manually. 3D printing of nozzles also drastically reduces the production time, as they can now be produced in bulk. Aside from reducing costs, this has the significant advantage that nozzles are now available in abundance, abandoning the need for cleaning and reusing existing nozzles.

As for the design, digital fabrication of printheads enables features that were impossible before. These features can significantly reduce the dead volume inside the nozzles, which is important for expensive materials or materials that are only available in small quantities. The design freedom also enables channels of arbitrary cross-sections, such as circular, square, triangular, or corrugated.

It is needless to say that other printing technologies can be used for fabricating these and other printheads, such as two photon polymerization. Two photon polymerization can scale down the whole nozzle by orders of magnitude, reaching scales that cannot be achieved by manual fabrication. Combinations of different printing technologies are feasible and promise a significant contribution beyond what is shown in this work.

4.4.2 *Material optimization*

The curing agent ratio and addition of fillers have shown that the properties of epoxy resin can be tuned to specific requirements. As such, the optimized core material shows a maximized toughness for a failure strain just above the required strain of 0.24 (Figure 4.6c). The optimized material also possesses a high modulus and strength, which is important for the structural stability of the core upon failure of the shell, i.e. the expected load drop after the initial failure (Figure 1.9b) is minimized. A material failure strain higher than the maximum strain apparent in the structure would, due to the mutual exclusivity, yield lower stiffness and strength, hence toughness within the relevant strain range. The material would not be efficiently used, as it is not strained to its maximum. Therefore, if the specific load case is known, it is important to optimize the material at the maximum expected failure strain for maximum stiffness, strength, and toughness.

4.4.3 *Individual struts*

The qualitative results confirm the hypothesis that an interfacial layer is able to stop a crack from propagating. However, in terms of toughness, this does not necessarily mean that the C-I-S strut absorbs more energy.

In the absence of the interfacial layer, diffusion between the brittle and flexible epoxy inks within the printed C-S struts may give rise to an interfacial zone, in which there is a continuous transition in mechanical properties (Figure 4.11). The diffusion zone could affect crack propagation and induce toughening mechanisms, such crack deflection, that cannot be seen in the qualitative tests [206–208]. This potential increase in toughness is counterbalanced by the strong interfacial bonding between the brittle and flexible epoxy materials that clearly allows stress to be readily transferred from the shell to the core.

By contrast, the presence of an elastomeric interfacial layer in the C-I-S strut stops cracks from propagating (Figure 4.9, Figure 4.10), but introduces a compliant region between the two epoxy materials that reduces their overall stiffness. While the ideal interlayer does not bond to either the core or shell epoxy material, it provides structural stability and gives rise to a

high coefficient of friction with both the core and shell materials that lead to the above observations. Besides the added toughness of the core, which remains intact, additional toughening mechanisms are expected from the more complex crack propagation at d/D = 0.85 (Figure 4.10d). The creation of new surfaces, for example, through crack deflection and crack splitting, is a well known toughening mechanism, especially in particulate-filled media [39, 209, 210]. It remains therefore important to also compare the two core-shell types quantitatively.

In terms of toughness, the quantitative results show that the C-I-S struts perform significantly better than the brittle or C-S struts (Figure 4.12, Figure 4.13). This can be explained by the increase in failure strain, that is large compared to the reduction in stiffness and strength (Figure 4.12). Further, the shell of the C-I-S strut with d/D = 0.85 shows multiple small decreases associated with graceful failure (Figure 4.12). Under these conditions, the shell continues to retain stability even after multiple cracks form, which absorb additional energy [211]. Similar behavior is observed in natural composites such as bone [13, 212] and nacre, [213] as well as alumina-PMMA composites, [12] in which these composite systems perform better than the individual constituent materials, as also seen at the C-I-S struts (Figure 4.13 bottom).

4.4.4 *Lattice structures*

In the lattices, the C-I-S struts fail in a similar way to the individually tested struts, indicating that the same principles apply. Indeed, in both the qualitative and quantitative results, a similar behavior is observed, i.e. crack bridging and bifurcation as well as graceful failure (Figure 4.15). Further the C-I-S struts now add a diagonal failure layer to the lattices, followed by a failure of the inverse diagonal (Figure 4.15a). This behavior is typical for elastoplastic materials of this unit cell type and comes with a large increase in toughness when compared to the conventional single-material struts and C-S struts. Further, as already seen in Chapter 3, it shows that the improvement on the strut level affects the performance of the lattice in a similar manner.

4.5 CONCLUSIONS

In conclusion, architected lattices composed of multicore-shell struts are printed that simultaneously possess high stiffness and toughness. By creating multiple printable materials and tailored coaxial nozzles, it has been demonstrated that 3D structures with well-controlled strut composition and geometry can be designed and printed by multicore-shell direct ink writing. The presented approach could be readily extended to more complex strut designs and lattice geometries for use in structural applications that require simultaneous optimization of weight and mechanical performance.

4.6 SUMMARY

Direct ink writing has been chosen to fabricate core-shell type II, which hypothesizes that a flexible core in a strut can provide additional toughness upon failure of the brittle shell. A novel printhead is developed that allows printing of (interfacial) layers with thicknesses down to 34 ± 18 μm. Direct ink writing can also process actual, engineering materials and custom-built materials tuned to specific, mechanical properties.

The structures printed without an interfacial layer did not show an improvement when compared to conventional, single-material structures. In the structures with an interfacial layer, the core remains intact upon failure of the shell and continues to absorb energy. In addition, it has been found that a specific layer thickness can add additional, energy absorbing mechanisms that lead to a total increase in toughness of over 130%.

5

CORE-SHELL TYPE III: BRITTLE CORE, BRITTLE SHELL

Die Energie kann als Ursache für alle
Veränderungen in der Welt angesehen werden.
— Werner Karl Heisenberg

This chapter has been adapted from a manuscript under review:

Mueller, J., Raney, J. R., Kochmann, D. M. & Shea, K. Multicore-Shell Beams for Stiff and Tough Cellular Structures. *(Under review)*.

5.1 INTRODUCTION

High stiffness, high energy absorption, and low density are properties that are typically mutually exclusive, but often desired in a wide range of engineering applications [6, 12, 77]. Nature finds ways to combine these properties by growing complex, multi-scale architectures that are challenging to replicate synthetically [50, 214]. On the material level, a higher energy absorption can be reached with minimal sacrifice in stiffness by incorporating fillers into a matrix material to impact-phenomena like crack bridging or delamination [6, 39, 211, 215, 216]. More specialized processes, such as freeze casting, can reach even better property combinations through a well-controlled dispersion or higher filler ratios, which, for example, increase the crack length, hence the energy requirement, through deflection [22, 50, 217].

To improve the properties to beyond what is possible by material composition alone, geometric features are added by manipulating the spatial distribution. For example, removing material where it is not required or not as efficiently utilized as in other places increases the efficiency relative to the weight. This can also be done in bulk by spatially tessellating unit cells to create metamaterials with a periodic (micro-)structure, macroscopically behaving like a homogeneous material with tailorable effective properties. In cellular structures, those effective properties are typically defined by their cellular architecture and the properties of

the solid constituents [111]. With relation to energy absorption, cellular structures have been extensively covered both theoretically and experimentally [60, 72, 113, 152, 161, 218–220].

Historically, stochastic foams were the dominant type used for energy-absorbing applications [8, 221]. With the advent of advanced manufacturing, researchers started to take advantage of defined and often discrete architectures that can be tuned to specific requirements [104, 222, 223]. Herein, the mechanical behavior of a lattice structure is typically described by the unit cell type: stretching dominated cells with a high connectivity support stiffness and bending dominated cells with typically a low connectivity are used for energy absorption [68, 222–224]. The performance of unit cells can be further improved by optimizing strut geometry and base material composition [135, 149]. With the aim of increasing the stiffness for a given unit cell relative to its weight, a typical approach is to cover the struts with a stiff material while keeping their cores hollow [64, 72, 109, 111, 161, 162, 197].

When it comes to energy absorption, the material selection has traditionally been the main tuning parameter [223]. Efforts have been made on the processing side to create solutions to enable the processing of ductile materials such as aluminum [218, 222] and on the materials side to create tougher materials, for example through particle-reinforcement [39, 120, 211, 215, 225]. More recently, lightweight cellular architectures have been explored for energy absorption from nano to macroscales [113, 151, 159, 191, 199] as well as for improved fracture toughness [198, 226, 227]. Those approaches usually exploited optimized truss topology and architecture [113, 151, 159, 191, 198, 199, 226, 227] as well as small-scale size effects.

In this work, a new investigation route is taken and geometric features are added at the individual strut level, without changing the topology of the structure, by splitting the struts into multiple, coaxially aligned layers (Figure 5.1).

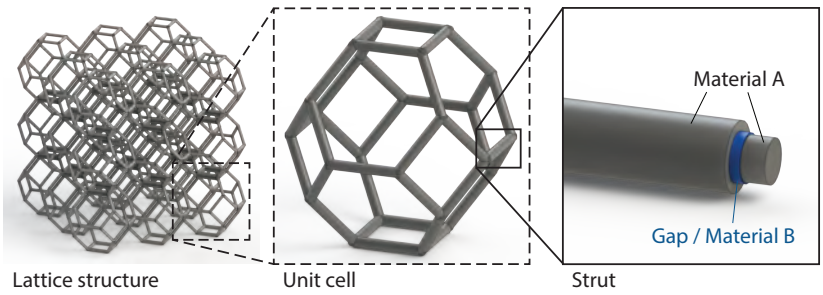

FIGURE 5.1: Lattice structures consist of multiple hierarchy levels, each of which affects the global response differently. The focus of this work is on the strut level. The struts are composed of a model material (Material A), which is separated into one or more coaxially aligned layers isolated by intersections (Gap / Material B).

By preventing bonding between layers, each layer in the strut fails individually when its respective maximum strain is reached. This leads to more benign failure of the strut over a range of strains rather than catastrophic failure when the maximum strain in the outermost layer is reached (Figure 5.2).

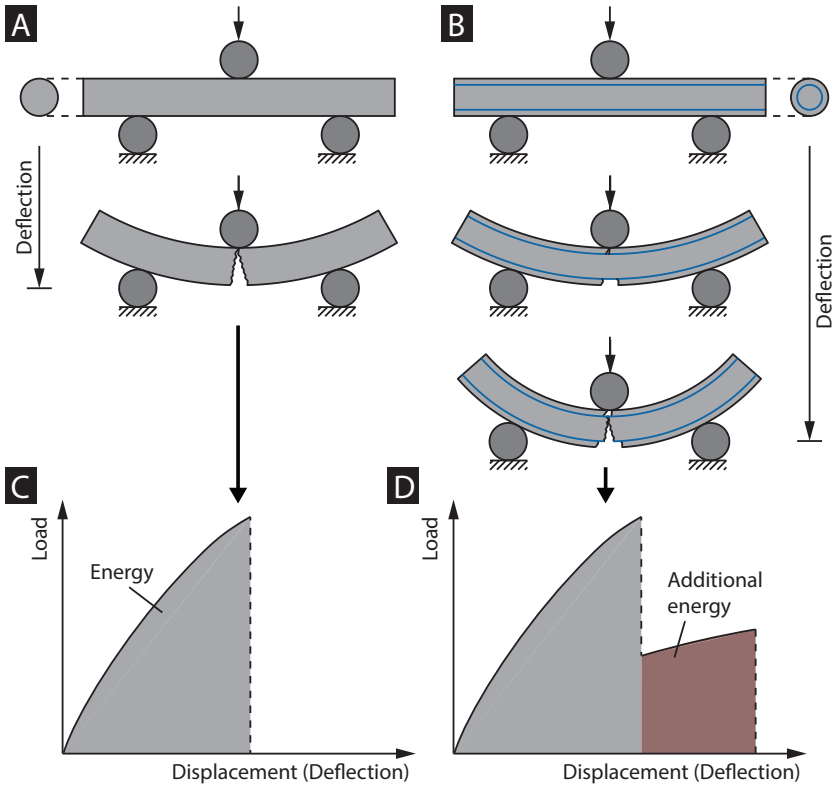

FIGURE 5.2: When compared to conventional struts (a), added gaps in the new design (b) allow each layer to fail when its respective failure strain is reached, rather when the failure strain in the outermost layer is reached leading to catastrophic failure (c). Hence, the total failure strain is increased (d), which results in an increase in absorbed energy when fracturing the structure.

Allowing the strut to fail over a range of strains greatly enhances the toughness of the strut. Despite the radial separation between layers, assuming the gap between layers remains negligible compared to the strut diameter and no significant slippage, the sum of the second moments of area and, hence, the stiffness of the strut, remains unaffected when compared to a conventional, monolithic strut. As some fabrication methods require a (interfacial) layer thickness greater than zero, the changes in energy absorption and stiffness are discussed when the distance between layers is allowed to increase, enabling the designer to find the best trade-off.

An analytical model is presented that computes the complete load-displacement response of rods and multi-layered struts under bending. Rather than making simplifying assumptions

about the constitutive behavior of the base material like linear elastic or elastic-perfectly-plastic as is typical [1, 157], the model is based on the full, experimentally-determined stress-strain curve. To this end, the model takes into account the deformation of the strut by integrating over the complete deflection history. Since the computational cost increases exponentially with the number of layers, mathematical optimization is applied and a detailed study on the role of the positions, numbers, and thicknesses of the gaps for different classes of engineering materials is presented. The model is validated through bending experiments on polymethyl methacrylate (PMMA) beams of different configurations.

5.2 METHODS

The analytical model relates the local stresses in the cross section to the global bending moment, M, as calculated from the free body diagram, where L is the length of the beam, to then calculate the force, F, for the given deflection (Figure 5.3a) [1].

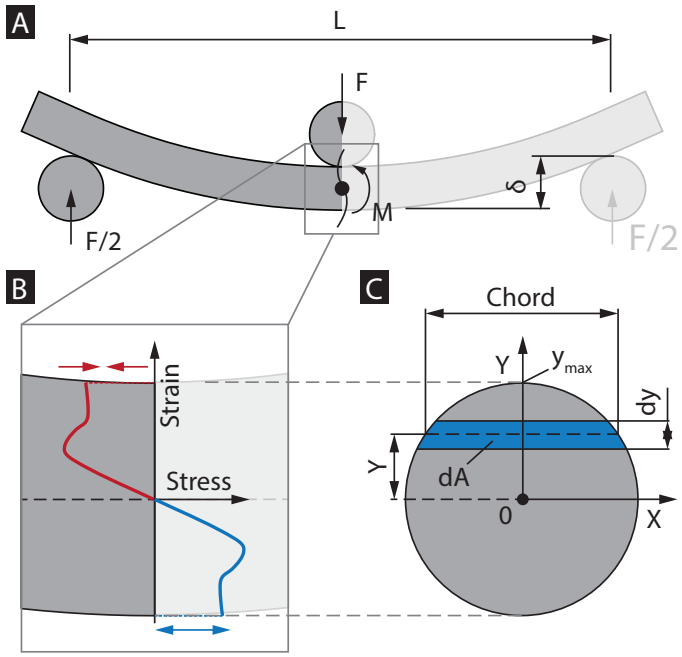

FIGURE 5.3: (a) shows a strut under bending, from which the global moment, M, is calculated. (b) using the stress-strain diagrams for the compression (red) and tension side (blue) of the neutral axis as inputs, the local forces for each vertical increment, dy, of the cross section can be calculated. (c) equating the sum of the local forces with the global forces for each deflection step, $d\delta$, the resulting bending load-displacement curve is calculated.

$$M = -\frac{FL}{4}. \tag{5.1}$$

As opposed to, e.g., the linear elastic assumption, the stresses in the model are not assumed to increase linearly away from the neutral axis to the bottom and top of the cross section. Instead, the nonlinear stress-strain relation of the base material is used directly, which can also distinguish between any tension/compression asymmetry on the two sides of the neutral axis (Figure 5.3b). By integrating the forces, dF, across the cross sectional area of the beam with their respective distances from the neutral axis, y, the moment is calculated. Since dF is equal to the product of the stress, $\sigma_{(y)}$, and area, dA, the stress distribution results in the total moment

$$M = \int_A y dF = \int_A y \sigma_{(y)} dA. \tag{5.2}$$

Due to the symmetry of the considered struts and the loading, the neutral axis is always in the center. As $\sigma_{(y)}$ is equal for every y, dA must only be calculated for each chord of the cross sectional circle. Describing the circular cross section as a function of the in-plane coordinates and a constant radius, $x^2 + y^2 = r^2$, the chord length, $c(y)$, can be expressed as a function of y (Figure 2c)

$$c_{(y)} = 2\sqrt{r^2 - y^2}. \tag{5.3}$$

Integrating the chord length over the height, as defined by two coordinates normal to the neutral axis, $y1$ and $y2$, dA is calculated as

$$dA = \int_{y_1}^{y_2} c_{(y)} dy. \tag{5.4}$$

In a similar manner, the area of the shells can be calculated by subtracting the chord of the inner circle from that of the outer circle. Combining Equation 5.2 and Equation 5.4, the moment is calculated as

$$M = \int_{-y_{max}}^{y_{max}} y \sigma_{(y)} c_{(y)} dy. \tag{5.5}$$

Replacing M with Equation 5.2 yields the flexural load-displacement curve as a function of the given stress-strain curve of the material,

$$F = \frac{4}{L} \int_{-y_{max}}^{y_{max}} y\sigma_{(y)} c_{(y)} dy. \tag{5.6}$$

The energy required to deform the strut, U, is represented by the area under the load-displacement curve, which is integrated over the deflection as

$$U = \int_0^{\delta_{max}} F d\delta = \frac{4}{L} \int_0^{\delta_{max}} \int_{-y_{max}}^{y_{max}} y\sigma_{(y,\delta)} c_{(y)} dy d\delta. \tag{5.7}$$

The overall modulus of the strut is calculated as

$$E_{tot} = \frac{I_1 E_1 + I_2 E_2 + \cdots + I_n E_n}{I_{tot}}, \tag{5.8}$$

with the total second moment of area, I_{tot}, of a circle being

$$I_{tot} = \frac{\pi}{4} \left(\frac{d}{2} \right)^4. \tag{5.9}$$

5.2.1 *Optimization*

The objective, $U(r_i)$, of the optimization is to maximize the energy required (Equation 5.7) when bending the strut by finding the optimized number of layers and their respective positions in the cross section, described by the outer radius, r_i, of the layers, i. The objective is subject to constraints given by the thickness of the interfacial layers, t_{gap}, and the minimum layer thickness, t_{min}, as dictated by the fabrication process, and the maximum radius, r_n (Figure 5.4). When there are multiple layers, the radius of each subsequent layer must not be smaller than its own radius (inequality constraint). The optimization parameters and conditions are summarized in Table 5.1.

Since the input stress-strain curve is given in the form of discrete, numerical data, which is not interpolated for reasons of accuracy, a large number of local maxima exist (Figure 5.8a, inset), limiting the choices of appropriate optimization algorithms. Further selection criteria are the constraint type (bound and inequality constraints) and variable type (discrete). A comparison of methods that both satisfy the criteria and are readily implemented resulted

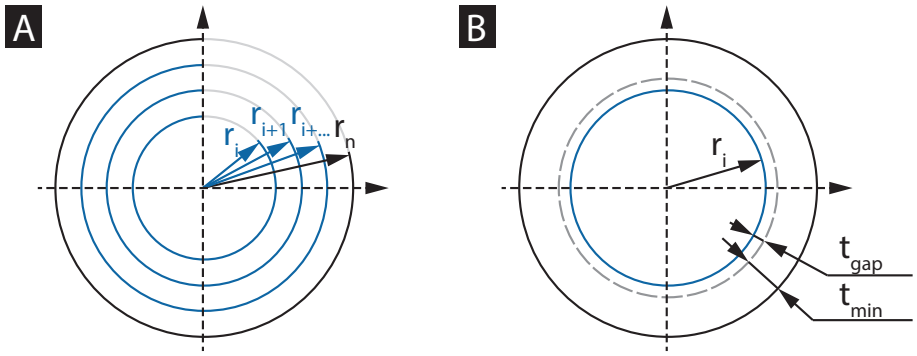

FIGURE 5.4: Definition of the layers radii (a). Using optimization, the required energy to break the strut can be maximized by approximating the optimal number of layers and their respective positions (b). Further, a gap of width t_{gap} with independent material properties can be implemented into the model to account for fabrication inaccuracies and tolerances.

Variables:

$$r_i = (r_1, r_2, \cdots, r_n)^T$$

where

$$i \in \mathrm{N}_0$$

Objective:

$$maxU(r_i)$$

(Equation 5.7)

Subject to:

Boundary conditions

$$t_{min} \leq r_i \leq r_n$$

Inequality conditions

$$r_{i-1} + t_{gap} \leq r_i$$

TABLE 5.1: Optimization parameters and conditions for single-material core-shell structures.

in Pattern Search [228] offering the best trade-off between accuracy and computational cost, which is therefore used throughout this work. The optimization results are verified against the manually generated solutions for the cases of one and two variables and are >99.9% accurate.

5.2.2 *Characterization*

To verify the accuracy of the model, three point bending tests are conducted on individual PMMA (PMMA XT, Amsler & Frey AG, Switzerland) struts. PMMA has an elastic modulus of 3.3 GPa, a failure strength of 70 MPa, and a failure strain of 5% [229]. Further, the transparency allows one to see the cracks and inner layers of the assemblies.

Conventional rods as well as two- and three-layered struts are tested. The two-layer struts are assembled at core-to-shell ratios of 0.5 (d1 = 4 mm, d2 = 8 mm) and 0.71 (d1 = 5 mm, d2 = 7 mm). The three-layer struts have a ratio of 0.5 and 0.7 with respect to the outer diameter, (d1 = 5 mm, d2 = 7 mm, d3 = 10 mm). As for the layered struts, all pairs of core diameter and inner shell diameter are identical, the gap distance is approximately zero.

The three point bending experiments are conducted on a Zwick/Roell Z005 universal testing machine equipped with a 5 kN load cell at a test speed of 20 mm/min. The test-rig is equipped with revolving rollers of diameter 6 mm and set to a span length of L = 60 mm.

5.3 RESULTS

First, the experimental results are presented and used to validate the numerical model. The model is then used to expand the design space within the PMMA material to analyze the effect of the core-to-shell ratio, number of gaps, and gap width. Finally, typical engineering materials are investigated with the model for applicability in the presented approach.

5.3.1 *Experimental validation of the model*

For the layered struts, the experimental results show a rapid crack propagation in the material that is stopped by the intersections, leading to a layer-wise failure (Figure 5.5a). Comparing the mechanical response of the two-layer rods to that of a conventional rod, i.e., a reference rod with the same cross section, but made out of a monolithic layer without gaps, the load-displacement curves are comparable up to the initial fracture, with identical moduli and strength values (Figure 5.5b,c).

Past that point, the conventional rod fails completely, whereas the core of the layered rod continues to sustain loads until its own fracture strain is reached. In the case of the 0.5 core-to-shell ratio, the load drop is relatively large, but the total fracture strain is increased by 95%, increasing the energy for complete fracture (measured as the area under the curve) by 20% (Figure 5.5b). For the larger ratio, the load drop is smaller while the fracture strain is increased by 60%. The energy required for fracture in this case is increased by over 50% (Figure 5.5c).

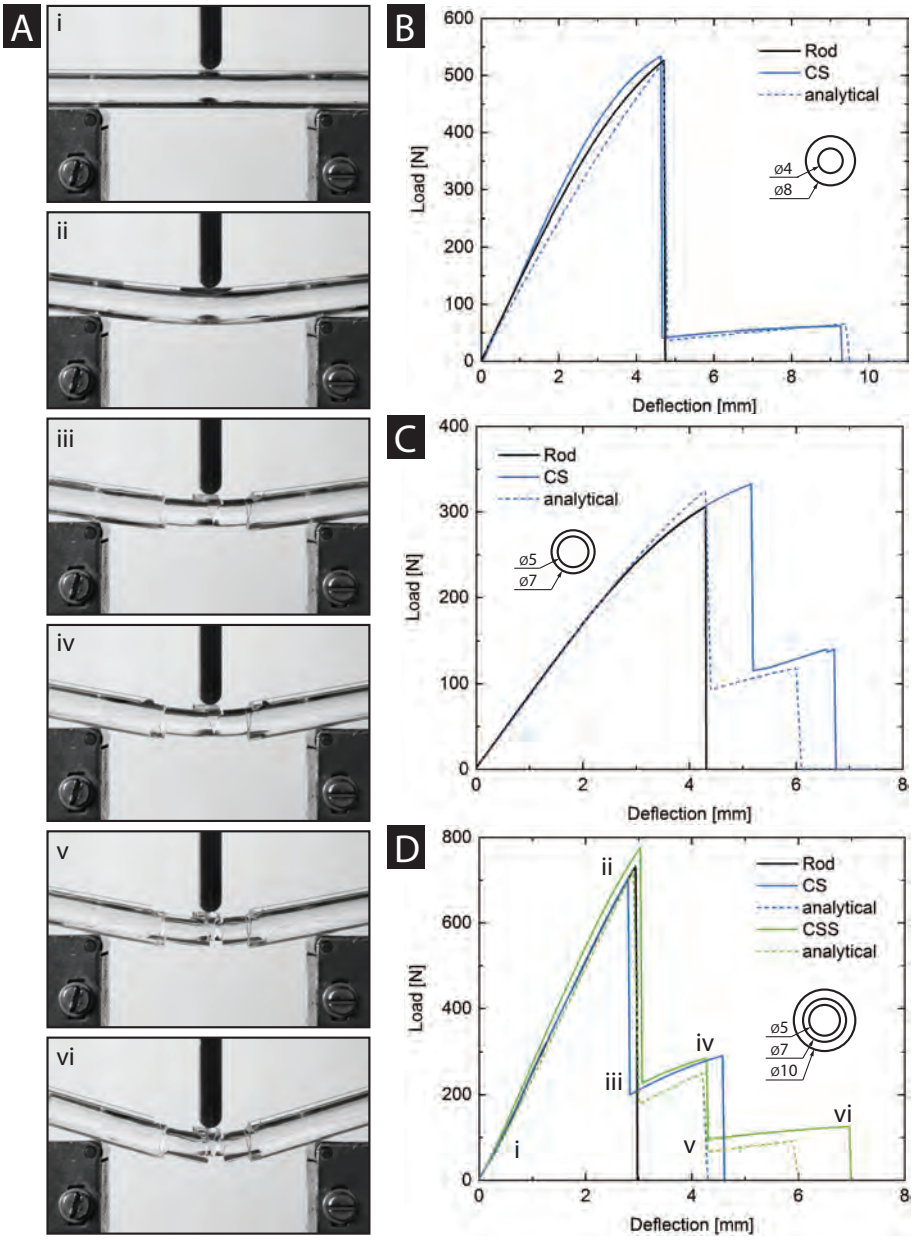

FIGURE 5.5: Compared to conventional, single-material rods, bending tests of the new design show a consecutive failure of the layers (a). The outer diameter of the rod is 10 mm. For a small core-to-shell ratio, the effective fracture strain is almost doubled, while the drop from the peak load is relatively high (b). For a larger ratio, the added failure strain is smaller, but the drop from the peak stress is smaller (c). While each case has its own advantages, both of them show a significant increase in the energy required to fracture the rod, with no sacrifice in strength and stiffness. Adding a third layer combines the advantages of the two-layer cases while further increasing the energy absorption (d). In all cases, the analytical model shows good agreement with the experimental results, with a tendency to underestimate the gained energy absorption and failure strain.

The three-layer strut fails in three steps and has a total increase in failure strain and energy absorption of 130% and 60%, respectively (Figure 5.5d). All tests show good agreement with the numerical results.

In addition to the numerical model, the experimentally tested specimens are simulated numerically with a commercially available, implicit FEM solver (Figure 5.6). Two symmetries (about the vertical axis in the beam cross section and about the beam midpoint) are added to reduce the computational time. The bottom nodes in contact with the bottom fixture are fixed in all degrees of freedom, and the top nodes of the top fixture in X and Y, while the latter are displaced vertically downward according to the imposed deflection. The dimensions are identical to the ones shown in Figure 5.5a,d, and the mesh size is set to 0.2 mm with C3D8R linear brick elements with reduced integration. The friction between the specimens and the steel fixtures is set to 0 as roll fixtures are used in the experimental set-up, and the friction coefficient between the different layers of the PMMA specimens is set to 0.5 [230]. The simulations are stopped before the emergence of cracks and analyzed visually (Figure 5.6) and quantitatively in terms of their load-displacement data (Figure 5.7).

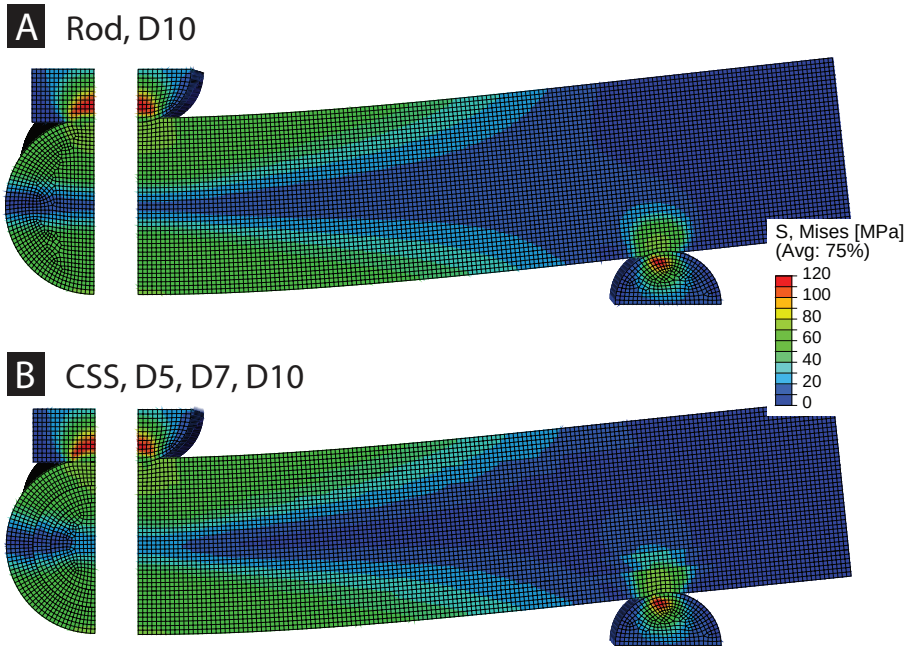

FIGURE 5.6: Cross sectional cuts of the specimens are shown for the rod-core-shell pair of outer diameter 10 mm. The intersection thickness is set to zero. The left pane shows the transverse plane and the right pane the longitudinal plane. The stresses are similar to the expected stresses from the analytical model and from the material data, and the addition of layers hardly affects the von Mises stress distribution.

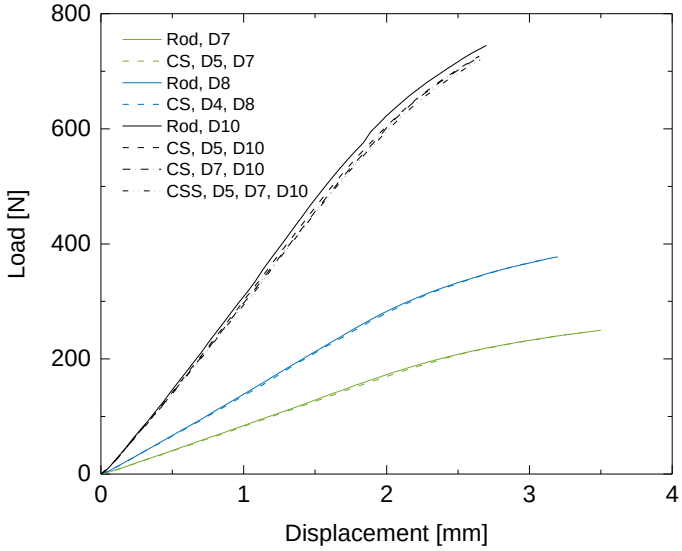

FIGURE 5.7: Load-displacement curves for the experimentally tested specimens are shown for the outer diameters of 7 mm (green), 8 mm (blue), and 10 mm (gray). The simulations are terminated before the emergence of cracks. For all pairs, the modulus is similar and only minor deviations are seen with increasing displacement.

5.3.2 *Effect of core-to-shell ratio, number of gaps, and gap width*

The numerical model allows further exploration of the design space by computing the results for all possible core-to-shell ratios in discrete steps (Figure 5.8).

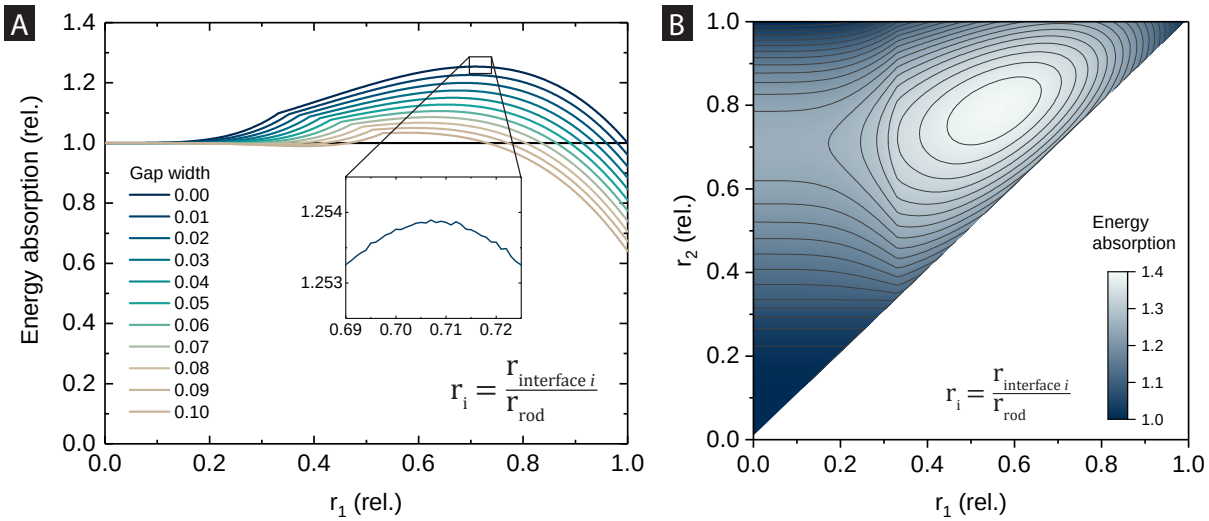

FIGURE 5.8: (a) sweeping the design space for the tested PMMA material with one intersection shows a possible increase in energy absorption of 25%, depending on the thickness of the gap. (b) in case of two gaps of zero width, the possible increase in energy absorption reaches 40%. The relative radii, r_i, are the ratio of the interface radius and the outer radius of the rod.

In the case of one intersection with no separation thickness, an increase in energy absorption relative to the conventional strut is observed at ratios starting from 0.2 (Figure 5.8a). The

relative increase grows until a maximum of 25% is reached at a ratio of 0.71, before it drops to the value of the conventional strut at a ratio of one. The model is also used to investigate the effect of a finite separation thickness. For this case, the worst-case scenario is assumed, in which the gap is not filled with a structural (load-bearing) material. With increasing gap size, the optimal core-to-shell diameter ratio decreases. When a gap is added at larger core-to-shell ratios, the relative energy absorption drops below one.

In the two-variable sweep with two gaps, the design space is increased and the additional variable allows one to further increase the maximum achievable energy absorption (Figure 5.8b). As before, if the gap width of both layers is zero and the ratio set to 0 or 1, the energy is not increased. This is also valid for more layers. The maximum for the two-variable system is reached at relative ratios of $r_1 = 0.58$ and $r_2 = 0.8$ for the first and second layer, respectively.

Optimization is used to explore numbers of gaps ranging from one to ten (Figure 5.9). The maximum achievable energy keeps increasing with added gaps for the case of zero gap width, eventually plateauing at an increase of 75%. The rise in energy absorption is relatively steep at the beginning and becomes smaller towards the end of the curve. For gap sizes larger than zero, maxima exist. The larger the gap width, the fewer layers are required to reach the maximum, and the smaller the maximum increase.

In terms of the effective modulus, no reduction is seen for zero gap width. For any gap width larger than zero, the modulus and hence the stiffness of the strut become smaller. For small thicknesses, the increase in energy absorption outweighs the decrease in the modulus, which is the opposite case for larger gap widths.

The gap positions indicate the (relative) diameters optimized for maximum energy absorption for each number of possible layers. It can be seen that, for larger gap widths, e.g. 0.30, and increasing numbers of gaps, small ratios between 0 and 0.2 are populated (Figure 5.9, bottom).

5.3.3 *Effect of material*

Next, different families of technologically relevant materials grouped into brittle, tough, and flexible are investigated. Setting the requirements to a span length between the supports,

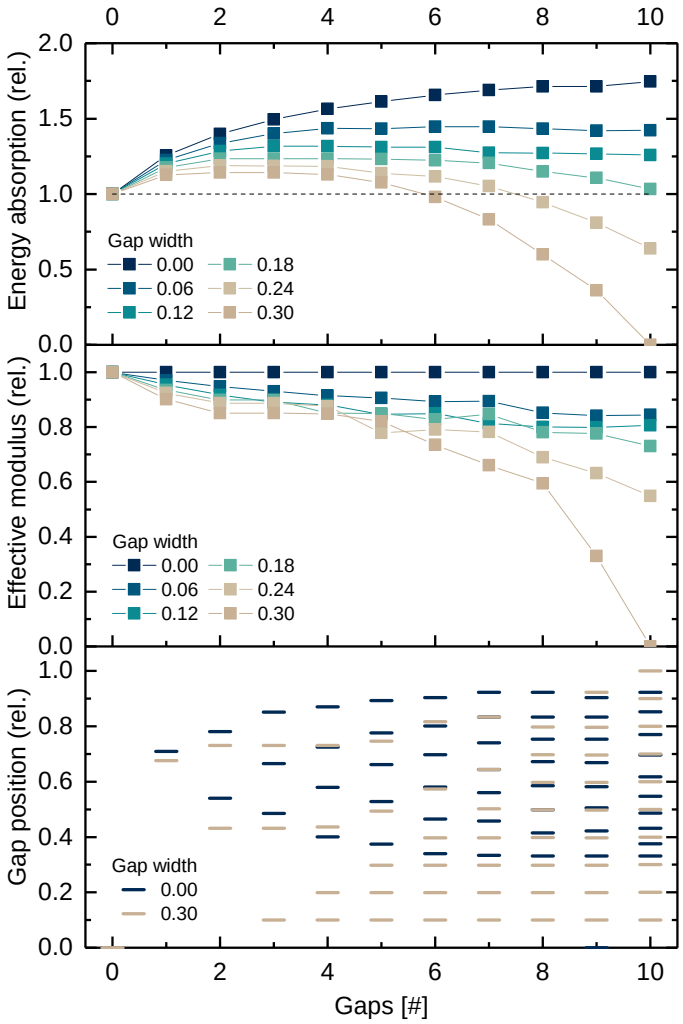

FIGURE 5.9: For three or more gaps, the computational cost quickly increases, making manual generation of all options infeasible. Optimization results show that thinner gaps are advantageous, and that more layers are generally better. An optimum exists for each gap width larger than zero. The results also show that small gaps reduce the modulus less than larger gaps, which eventually remove all the available material, yielding a modulus of zero. The optimized gap diameters (bottom) indicate saturation with an increasing number of gaps, as more of the lower and ineffective diameters/gap positions are populated.

diameter, and deflection that yield a maximum strain of 15%, common engineering materials with failure strains ranging from well below to above 15% are selected (Figure 5.10a).

The optimization results for zero gap width show that the fiber-reinforced epoxy (FR epoxy), which is the most brittle material of the available options, reaches the highest increase in relative energy absorption, approaching 70% (Figure 5.10b). No increase is seen for thermoplastic polyurethane (TPU), and intermediate values are reached for all other materials.

The relationship is further explored by fixing the material and varying the maximum required strains (Figure 5.11). As the strains are calculated by the span length, strut diameter, and deflection, the shown values represent realistic ranges for different combinations of the

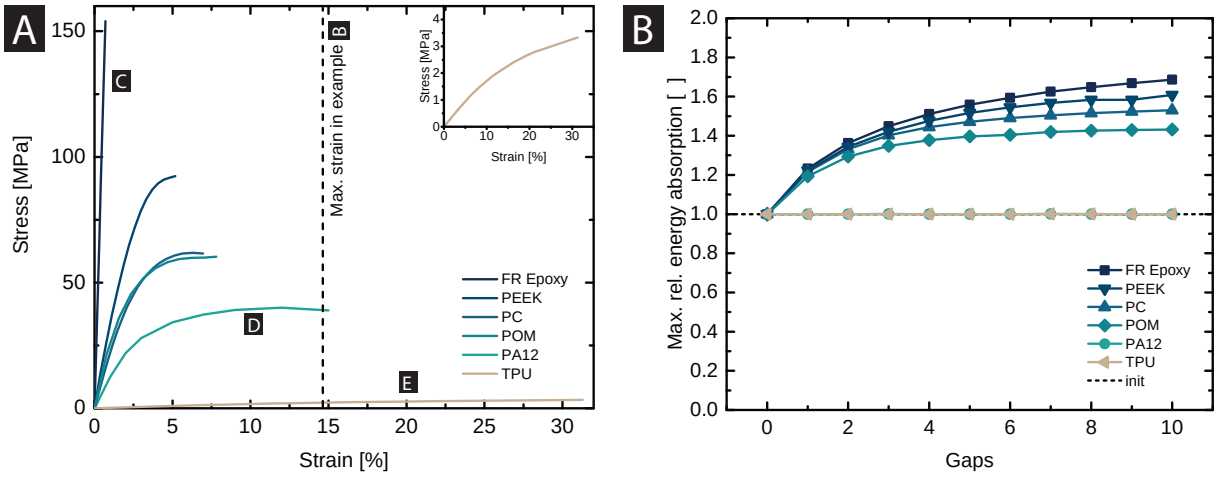

FIGURE 5.10: Implementing the model for a selection of typical engineering materials (a) shows that the maximum increase in energy absorption depends on the modulus, strength, and failure strain, which needs to be smaller than the bending strain reached in the strut (b). The material data is retrieved from [231].

properties. The brittle material, represented by the FR epoxy, does not show an interaction effect between the strain and gaps, suggesting that a further increase or decrease in strain will not affect the maximum reachable energy absorption (Figure 5.11a).

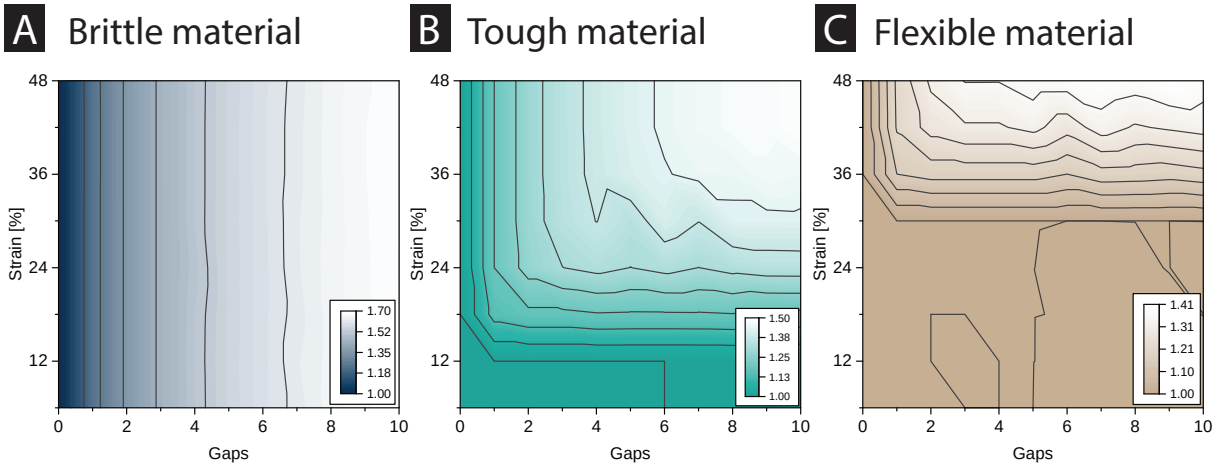

FIGURE 5.11: Brittle materials show an improvement at relatively small bending strains (a), while tough materials have a clear transition zone (b), which is shifted upwards for flexible materials (c). The brittle materials are represented by the FR epoxy, the tough materials by the PA12, and the flexible materials by TPU.

For the tough material, represented by Polyamide 12 (PA12), an interaction effect is seen at values higher than 15% strain, which equals the failure strain of the material. Below that value, the effect is similar to the previously discussed case of TPU where no fracture occurs (Figure 5.11b). Above 15% and below 42%, a transition region is observed where both an increase in gaps and strain yields a higher energy requirement. In the case of the flexible material, represented by the TPU, the trend shifts further up, displaying a transition zone

starting at 30% and going up to >48% (Figure 5.11c). Because the tested strain of 15% is below the transition, no improvement is seen in the example of Figure 5.10b.

5.4 DISCUSSION

First, the experimental results in combination with the model are discussed. The model is then expanded to investigate the effect of core-to-shell ratio, gap number, and gap width. Lastly, the effect of the material on the increase in toughness is discussed.

5.4.1 *Experimental validation of the model*

The experimental results show that a crack propagation can be stopped by the addition of an intersection, leading to the expected, layer-wise failure (Figure 5.5a). In the quantitative analysis, this is reflected by a load-displacement curve that continues past the initial failure, which is when conventional rods fracture completely. This property alone can already be used to add an advanced warning system through, for example, sensors to the structure that detect initial failure.

More importantly, the initial part of the curve, up to the first failure, does not differ from that of a conventional strut. Hence, any continuation of the curve adds toughness. The height and length of the continued curve depend on the core-to-shell ratio: the higher the ratio, the higher the load and the smaller the added fracture strain. This suggests that an optimal core-to-shell ratio exists.

When a second intersection is added, the load-displacement curve is increased further. Due to the fact that intersections do not alter the existing curve, the effect of additional interfacial layers (or toughness) can simply be added to the existing system. This suggests that a large number of intersections is better than a small number.

The experimental results have also been used to validate the model, which now allows investigating in detail the dependencies of added toughness on the core-to-shell ratio, number of layers, and interfacial layer thickness.

The slight underestimation of the model, in that it predicts less added toughness than observed in the experiments, is advantageous from a safety perspective, as the actual system will absorb more energy than predicted. Further, it shows that the computed values in this work can be considered absolute minimums and that the actual increases are by trend even higher.

In addition to the numerical model, the theory has been confirmed via finite element analysis (Figure 5.6). It reveals that the stresses are comparable to the ones expected from the material data and those of the analytical results. The addition of layers does not significantly affect the stress distribution, which confirms the hypothesis that they do not weaken the cross section. Further, there is no significant shear observed in any of the cross sections, which supports the use of Euler beam theory in the model. The analysis of the load-displacement curves shows similar moduli for all pairs of the same outer diameter (Figure 5.7). In addition, the curves overlap and only minor deviations are seen with increasing deflection.

5.4.2 *Effect of core-to-shell ratio, number of gaps, and gap width*

To maintain comparability, the same experimentally validated PMMA system is used to explore the design space for the variables core-to-shell ratio, number of interfacial layers, and interfacial layer thickness.

As hypothesized, an interfacial layer or gap of zero width cannot decrease the energy absorption of a strut, and an optimum exists (Figure 5.8a). For gap widths larger than zero, as potentially applicable in other fabrication processes, such as additive manufacturing, there is little effect at small core-to-shell ratios. This is due to the fourth-order dependency between strut stiffness and diameter. At large ratios, the gap results in a reduced outer strut diameter, rather than in a separation of the strut into two layers. Due to the fourth-order dependency, the same gap width now has a large negative effect on the stiffness, hence toughness of the strut. However, even for relatively large gap widths, the energy absorption capability of the strut can be significantly increased at the optimal core-to-shell ratio.

The case of two variables has been investigated for zero gap widths (Figure 5.8b) and shown that a maximum exists away from the axes, while the properties on the axes are identical to

the ones with one interface. This means that interaction effects exist. As discussed before, additional interfacial layers can be added to an existing system and further increase the toughness. However, if the goal is to achieve the maximum toughness for a given number of layers, the system needs to be recalculated as a whole when computing the optimal intersection layer positions. It further states that the addition of layers can only increase, but never decrease the energy absorption of a system with zero gap width.

While the generation of all possible solutions is straight forward and descriptive, it is also computationally expensive. In fact, the number of required calculations increases exponentially with the number interfacial layers, n, and incremental steps, k. The complexity is $O(k^n)$. Further, the step size is discrete, even a small step size cannot guarantee that the optimum is found, as it may lie in between two points. For those reasons combined, optimization has been used to explore the design space beyond two gaps (Figure 5.9).

As hypothesized, for zero gap width, the maximum achievable energy keeps increasing, until it eventually plateaus. This is due to the design space, i.e. the available options for additional layers, being reduced with increasing gap numbers. For gap widths larger than zero, an optimum must exist, as, at some point, the whole strut will consist of gaps only. The larger the gap width, the fewer layers are required to reach the maximum, and the smaller the maximum increase.

In terms of the effective modulus, no reduction is seen for zero gap width. This is interesting as it means that, theoretically, an infinite toughness can be achieved, without reducing the effective modulus. In practice, however, even the thinnest gap has a finite width.

For any gap width larger than zero, the modulus and hence the stiffness of the strut become smaller. For small thicknesses, the increase in energy absorption outweighs the decrease in the modulus, which is the opposite case for larger gap widths. In Figure 5.9 bottom, it is seen that, for larger gap widths, e.g. 0.30, and increasing numbers of gaps, small ratios between 0 and 0.2 are populated. This range has shown to be ineffective in terms of increasing energy absorption (Figure 5.8a), and can be used for unneeded layers, which would otherwise have a larger, negative effect. Eventually, this leads to a hollow strut where only a thin shell remains, the mechanism typically seen to maximize relative stiffness and strength in lattices [111, 113, 232].

5.4.3 *Effect of material*

The materials are chosen to represent typical engineering materials, ranging from some of the most brittle (FR epoxy), to ductile (PA12), to flexible (TPU) materials. The optimization results show that the more brittle the material, the higher the relative increase in energy absorption. This can be explained with the failure strain. If the failure strain of the material is equivalent to the maximum strain in the strut, the strut will not fail. Resultingly, because the strain decreases from the outside of the strut to the inside, the addition of interfacial layers will be of no effect. If the same strut is deformed more, the strain equivalent to the failure strain of the material will not be reached at the outside of the strut anymore, but further to the inside. Hence, the strut will fail. The strain or diameter range between the minimum diameter where the strut will fail and the maximum diameter of the strut is the space where interfacial layers can be added. Hence, the smaller the failure strain of the material, the larger the margin to increase the toughness for a given maximum strain in the strut. Reversely, if the failure strain is small, such that the equivalent diameter in the strut is ineffective in comparison to the outer diameter, a further increase is not expected. This becomes more obvious in Figure 5.11, where clear zones of inefficiency (small strains), transition, and plateauing (high strains) exist.

The principles developed also hold if one replaces the gaps with separation layers comprised of soft or even active materials, as long as they do not promote the propagation of cracks across layers. This would allow the design of multifunctional lattices while maximizing mechanical properties such as energy absorption and stiffness.

5.5 CONCLUSIONS

Through a relatively simple yet powerful architectural design principle, it has been shown how struts in cellular networks can be equipped with significantly higher fracture toughness without sacrificing stiffness and strength. Crack arrest mechanisms, commonly exploited in composite materials, are introduced at the individual-strut level resulting in a stepwise strut failure under loading that can also serve as an easy-to-detect, early-warning mechanism signaling the risk of complete failure. The shown example of circular beams serves as an example that can now be generalized and extended in various directions. The principle of

introducing geometric interfaces is scale independent and can be applied to other structures and geometries. The outcome is expected to find application in many areas, such as transportation, packaging, and sports equipment, to further improve the safety and efficiency of advanced materials systems.

5.6 SUMMARY

High stiffness, high fracture toughness, and low density are essential material properties for numerous engineering applications. As these properties are typically mutually exclusive, they are rarely found in nature and synthetic replications are unsuitable for lightweight lattice structures. In this work, a new, scale-independent architectural principle is presented to design struts in lattices that possess both high stiffness and toughness. The architected struts consist of multiple, coaxially aligned layers separated by interfaces that prevent cracks from propagating, hence absorbing more energy when fractured. Through analytical modeling and computational optimization, it is shown that the concept works best for brittle materials, and that a small interface thickness and a large number of layers is advantageous. The results are validated experimentally and show that the energy absorption and fracture strain can be increased by 100% when compared to conventional reference struts with no sacrifice in density or stiffness.

6

DESIGN GUIDELINES FOR CORE-SHELL STRUCTURES

Can one think that because we are engineers, beauty does not preoccupy us or that we do not try to build beautiful, as well as solid and long lasting structures? Aren't the genuine functions of strength always in keeping with unwritten conditions of harmony?

— Alexandre Gustave Eiffel

This chapter summarizes the key features of the three core-shell principles and discusses differences and potential applications. As such, design guidelines are developed to assist designers, engineers, and scientists in the selection process.

6.1 CHARACTERISTICS AND APPLICATIONS IN COMPARISON

Three different core-shell principles are presented, each of which is suitable for different load-cases. The principles differ mainly in terms of their activation mechanism, e.g. fracture or no fracture, performance, and manufacturability, from which different applications result. The focus of this work is on verifying the principles and comparing relative improvements to conventional systems, rather than maximizing absolute properties for specific material systems. This needs to be taken into account when comparing the presented values to literature, where often different materials or processes are used. In the following, the characteristics of the different core-shell types are summarized and compared.

6.1.1 *Core-shell type I: brittle core, flexible shell*

ACTIVATION MECHANISM The energy absorption or toughness of type I can be optimized for any strain before failure, where failure can be defined as the yield strength, rupture,

or other failure mechanisms at any other point on the stress-strain curve. No fracture toughness is added post rupture. This enables (quasi-)static and dynamic load cases, such as cyclic loading and impact.

PERFORMANCE For given load cases, the stiffness, strength, and energy absorption can be increased by factors ranging from 1.5 to over 42, when compared to the best available single-material option. The exact factor is highly dependent on the available materials. The failure strain remains the same and is not reduced.

MANUFACTURABILITY It is possible with modern multi-material 3D printers to fabricate complex lattice architectures with type I struts. Alternatively, some single-material printers allow fabrication of materials with different properties, for example, due to changes in laser intensity [144]. However, current 3D printers are limited in their resolution and introduce scaling effects [233]. Current 3D printers are also limited in their materials choice, for example, to UV curable materials, which limits the application space. As these limitations are a fundamental problem, not just in core-shell structures, it is expected that research will make quick progress, eventually allowing to fabricate these structures into complex architectures of arbitrary materials.

APPLICATIONS Type I struts suit all structures that are loaded one or more times and are most efficient when the structures are loaded to the optimized strain. If the structure is loaded beyond that point, it is at risk of plastic deformation or fracture. However, the maximum strain can often be predicted beforehand and adjusted for with a safety factor, as a strain below that point only marginally reduces the efficiency. This makes the principle highly interesting for areas such as

- aerospace and automotive, extending to damp vibrations, reduce fatigue, and increase safety and reliability.
- packaging, to create thinner layers of similar performance, hence cheaper and less environmentally impactful packagings.

- sports equipment, such as American football helmets, to increase the safety and reduce brain damage.

Type I is independent of size effects and, therefore, applicable at all scales.

6.1.2 *Core-shell type II: flexible core, brittle shell*

ACTIVATION MECHANISM The energy absorption or toughening mechanism sets in after fracture of the shell and can also be considered a fracture toughening mechanism. A minor reduction in stiffness and strength is outweigh by an increase in toughness and can be tuned to specific requirements.

PERFORMANCE In the tested system, the optimal strut demonstrated an increase in toughness of 130%, while the stiffness was reduced by 30%.

MANUFACTURABILITY Similarly to conventional direct ink writing, the developed system can print arbitrary materials, ranging from ceramics [84, 234], to polymers [84, 235], to metals [236, 237], providing vast freedom in the materials choice. In terms of complexity, direct ink writing enables the fabrication of decently complex lattices, such as 2.5D honeycombs and woodpiles. Research is currently underway to create more complex, cellular architectures through embedded direct ink writing and expected to close the gap between materials choice and complexity [91, 238].

APPLICATIONS In practice, type II structures are typically not expected to fail, but critical to safety when they do. This often applies to safety gear, such as motorcycle or skiing helmets (as opposed to, for example, American football helmets, which need to withstand multiple impacts). In safety gear, it is not only the energy absorption that counts, but also the energy absorption to peak stress ratio [77]. This ratio ensures that impact forces are damped and not fully transmitted through the structure onto the protected item. As in type II, the increase in toughness comes at a (small) decrease in stiffness and strength, the structures are well suited for such applications and can be tuned to the specific requirements.

6.1.3 *Core-shell type III: brittle core, brittle shell*

ACTIVATION MECHANISM Similarly to type II, the mechanisms of type III set in post fracture. Type III is suitable for structures that cannot compromise on stiffness and strength when it comes to increasing the (fracture) toughness.

PERFORMANCE For the system considered, increases in toughness or energy absorption of more than 100% are reached without sacrificing any stiffness or strength.

MANUFACTURABILITY For the principle to be most effective, a gap width of virtually zero is required, which is currently impossible to fabricate with 3D printing processes. However, research is underway, trying to close the gap between resolution and scale. It is, therefore, only a matter of time until such processes will be able to fabricate complex, type III-based lattice structures.

APPLICATIONS Similarly to type II, type III requires failure to be effective. However, as the mechanism is not expected to reduce stiffness or strength, it can be added to high performance structures regardless. The mechanism is most efficient for semi-brittle or brittle materials, scale-independent, and complementary to existing approaches. As the energy absorption is increased, the energy absorption to peak stress ratio goes down. However, as the strength is not reduced, there is more stress transmitted when compared to type II. The approach is, therefore, primarily interesting for application where the ratio does not matter as much, such as packaging material.

6.1.4 *Conclusions for designers, engineers, and scientists*

The most important difference for a designer is whether the application allows failure or not before the energy absorption mechanisms set-in (Figure 6.1). If failure is not allowed, the only option is type I. If failure is allowed, the choice is between type II and III, and depends mostly on the transmitted peak stress requirements. If the peak stress is irrelevant, type III can be

selected, as it offers favorable stiffness and strength values. If the peak stress matters, type II offers a superior performance as it slightly reduced the peak stress in order to introduce energy absorption mechanisms.

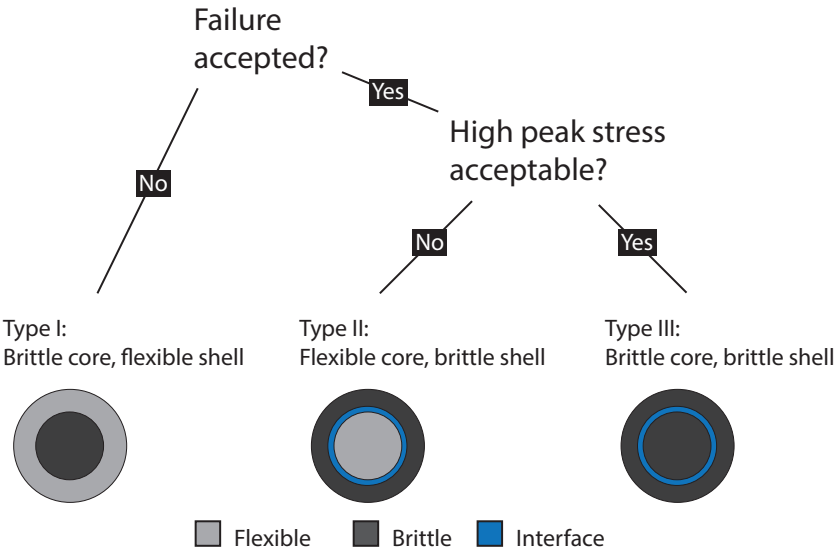

FIGURE 6.1: Example design decision tree. The first decision distinguishes between failure and no failure. If failure is accepted, one needs to decide between a high peak stress and high toughness, and a slightly lower peak stress and slightly lower toughness, each of which has different advantages and applications. Note that the schematics represent the simplest cases, i.e. minimum amount of layers for the mechanism to work.

Each core-shell type can be tuned within its group and overlaps between the mechanisms and applications exist. Besides the mentioned differences, additional differences exist that can be relevant when designing for core-shell struts.

6.2 COMBINATION OF DIFFERENT MECHANISMS

In addition to the individual mechanisms of the three cases, combinations are possible to increase the efficiency further (Table 6.1). As the processes used to fabricate each core-shell type are highly different from each other, the following statements are hypothetical and not validated experimentally.

	Type I	Type II	Type III
Type I	-	=	=
Type II	Combination (1)	-	=
Type III	Combination (2)	Combination (3)	-

TABLE 6.1: Possible combinations of the different core-shell strut types.

COMBINATION (1) considers type I and II (Table 6.1). As type I is not expected to fail, it does not make sense to incorporate type II into type I. However, incorporating type I into type II is possible and meaningful (Figure 6.2). So far, in type II, the core has been optimized for a specific strain, for which it maximizes stiffness and strength. As the strain in the core increases linearly from the neutral axis to the outside, the core can be equipped with the mechanism acting in type I. This would significantly increase the energy absorption of the strut and reduce the drop in load when the shell fails catastrophically.

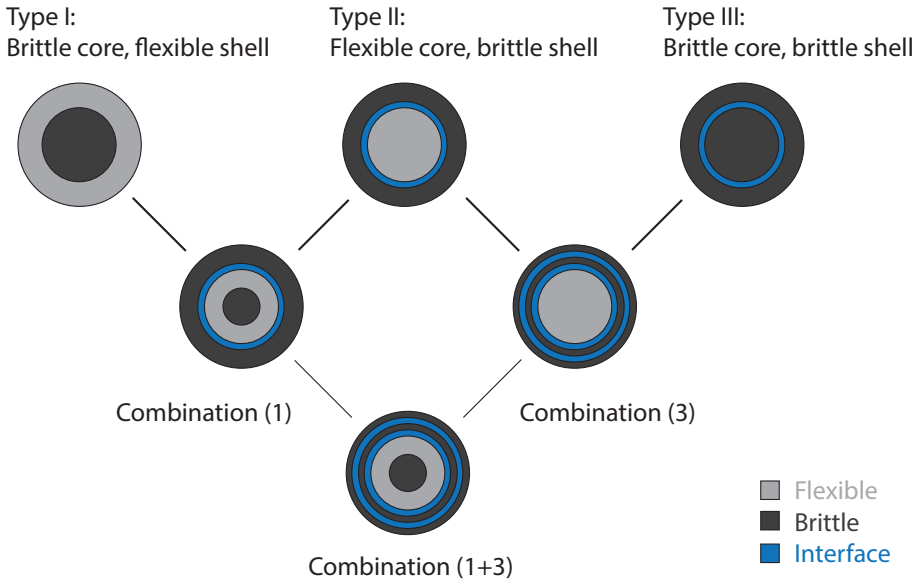

FIGURE 6.2: Feasible combinations of the mechanisms. Combination (1) enhances the core of type II with the mechanism of type I. Combination (3) improves the shell of type II with the mechanism of type III. Both approaches can be combined into Combination (1+3). Note that each schematic represents the simplest case, i.e. minimum amount of layers for the mechanism to work.

COMBINATION (2) considers type I and III (Table 6.1). Since type I is optimized such that all layers fail at the same, prescribed strain, intersections added to separate the layers would not make a difference or increase the energy absorption. The other way around, adding gradients to the separated layers of type III would allow to optimize each layer separately for a given load case, potentially increasing the energy absorption. However, this is contradictory with the finding that the more layers, the higher the increase in energy absorption, as this also means that the layers become thinner, making the effect of gradients obsolete. Combination (2) is therefore only meaningful under specific conditions.

COMBINATION (3) considers type II and III (Table 6.1). Integrating type II's principle in type III does not make sense physically. The other way around, it is possible to split either the core or the shell into radial layers. As the core is not expected to fracture, a layered core would not increase toughness. The shell, however, has shown a significant additional source of energy absorption when reaching a specific thickness. By adding additional, brittle layers to the shell of the existing type II core-shell system, it can be imagined that it would not only add the mechanism of type II, but combine it with the mechanism found in type III, further increasing the total energy absorption of the system.

In conclusion, the feasible and most promising combinations are Combinations (1) and (3). Combination (1) improves the core of type II with type I. Combination (3) improves the shell of type II with type III. It is therefore a logical consequence that Combinations (1) and (3) could be combined into Combination (1+3) to further improve the fracture toughness (Figure 6.2, bottom).

In addition to combining the presented approaches with each other, combinations with mechanisms presented in literature are possible, such as fiber-reinforced materials with different fiber contents in type I or hollow struts equipped with type III shells.

Aside from combining different mechanisms locally, they can also be combined in their applications in other ways. For example, when used as a cellular meta-material, a stiff strut of type III could be placed at the outside of a helmet. As this type transmits a higher peak stress than type II, type II could be placed as a center layer. The inner layer could be built from type I, which adds energy absorption, but has a relatively low peak stress when compared to the other types.

6.3 RELATIVE PERFORMANCE COMPARED TO LITERATURE

In a direct comparison with hollow struts, the added energy absorption in the core-shell struts scales approximately linearly with the added core material. This means that the properties relative to the density do not change significantly in either direction. However, a direct comparison to struts with hollow cores is not intended. Rather, both strut types, i.e. hollow struts and core-shell struts, compare to conventional solid struts and pursue different goals. The hol-

low struts decrease both stiffness/strength and density. As the density is reduced more than the stiffness/strength, the relative stiffness/strength increases [109–111]. The core-shell struts do not significantly change the density and increase the toughness, hence also the relative toughness property. Additionally, depending on the core-shell type, the stiffness/strength is either increased or roughly maintained.

Figure 6.3 shows an Ashby chart that compares compressive strength with relative energy per volume for different engineering materials, namely foams, elastomers, plastics, metals, and ceramics. The chart shows a general trend for the materials in that the compressive strength scales linearly with the energy per volume (slope = 1), i.e. the higher the compressive strength, the higher the energy absorption. Notable deviations are seen for non-technical ceramics, where the energy absorption increases more than the compressive strength.

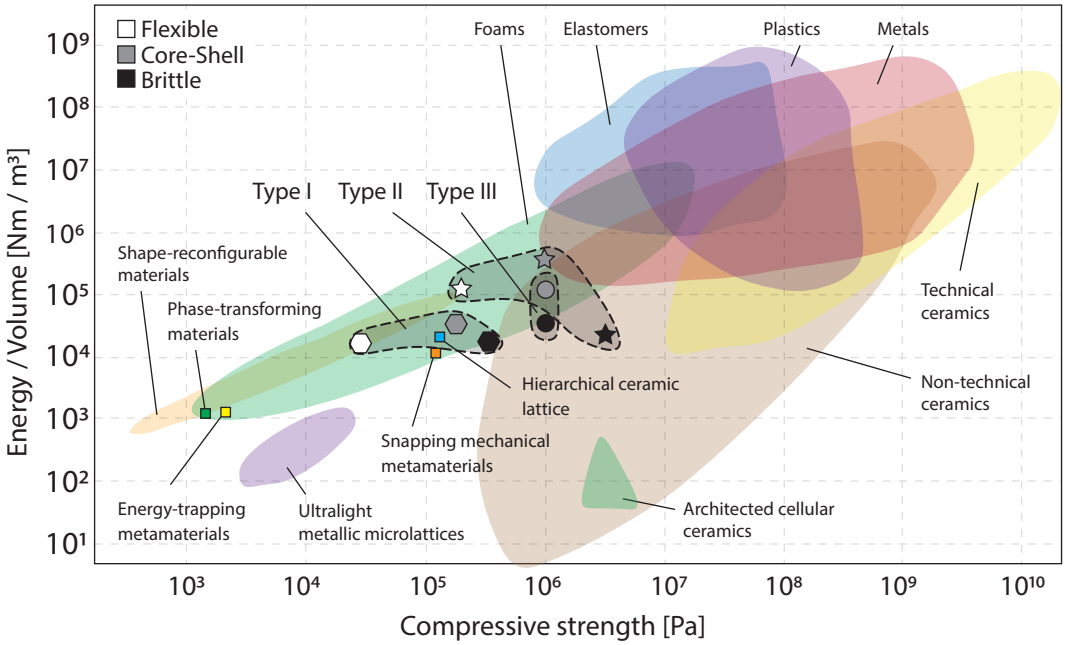

FIGURE 6.3: Ashby diagram for the compressive strength and energy per volume relationship of different materials, fitted with the experimental data from this work. The chart is adapted from Haghpanah *et al.* [239] and extended with additional data from the following sources. Shape-reconfigurable materials [239], phase-transforming materials [240], energy-trapping materials [241], ultralight metallic microlattices [72], snapping mechanical metamaterials, [242], hierarchical ceramic lattice [191], architected cellular ceramics [64]. The type III data is extrapolated from bending tests, assuming a relative density of 15%. Note that the materials of this work are chosen to validate the theoretical models. The areas can, therefore, significantly differ when different materials are used.

As different applications require different properties, all areas on the chart can be equally important. However, there are physical limits in that materials cannot have a low compressive strength and a high energy per volume at the same time (or vice versa). As these properties

might be advantageous for certain applications, researchers have been trying to fill empty areas with both improved, conventional materials and meta-materials [239]. Materials in the top left corner of the charts are considered optimal from an impact resistance perspective, as they absorb a lot of energy with little load transmitted to the underlying item [151, 239].

Foams have additional design variables, such as relative density and strut diameter. This allows to span a wide property range, from being the weakest materials to being stronger and more energy absorbing than certain ceramics, elastomers, metals and plastics (of which they are typically fabricated from). The chart is extended with data from recent research accomplishments, such as ultralight metallic microlattices [72], which fill a previously unoccupied space.

The chart also shows the data of the herein presented core-shell lattices. The data covers only the experimental results and does not contain the data generated with the numerical models. In the experiments, the focus was on the validation of the principles, rather than on achieving the highest, absolute values. The experiments are, therefore, conducted with materials that are available for the used process, and not with the optimal materials on the chart. It is, therefore, valid to state that areas even larger than the (gray) areas indicated can be occupied when different materials are used, making the approach highly versatile.

It is also important to mention that the Ashby chart shows only two properties – energy per volume and compressive strength. If a third property, such as density, was added, similarly looking materials or trends in this chart can look completely different. Besides filling empty spaces, it may therefore also be advantageous to fill already occupied spaces with alternatives to choose from. Showing the energy per volume versus the compressive strength provides, therefore, by no means a complete and comprehensive picture, and may only be considered as one of many possible examples, representing one specific scenario.

6.4 SUMMARY

The design guidelines highlight the differences in the application of the core-shell struts and are provided for designers, engineers, and scientists who intend to implement the presented principles. It is also shown how the performance could be further increased by combinations

of different mechanisms or different unit cells with different core-shell struts. With respect to literature, the findings already show significant improvements and, more importantly, the potential to transform the field of stiff, strong, and tough lightweight structures when applied to other engineering materials without the processing limitations faced in this work.

7

CONCLUSIONS AND OUTLOOK

> *But see that the imagination of nature is far, far greater than the imagination of man. No one who did not have some inkling of this through observations could ever have imagined such a marvel as nature is.*
>
> — Richard Phillips Feynman

Chapter 1 introduces three core-shell principles that are investigated in detail in Chapters 3 to 5. Chapter 6 discusses the principles in relation to each other and to literature, and develops design guidelines for using core-shell structures. For each principle, a suitable fabrication method is used. This chapter summarizes the main contributions and findings of the work with respect to the research question and hypotheses stated in Chapter 1. Conclusions are drawn for designers, engineers, and scientists, and an outlook is provided on the challenges and opportunities ahead.

7.1 PRINCIPAL FINDINGS AND CONTRIBUTIONS

The research question stated in Section 1.2.4,

> **Main research question:** *How can the toughness of cellular lightweight structures be increased without negatively affecting stiffness and strength?*

has been addressed by investigating the two main research hypotheses as follows.

> **Hypothesis H_1:** *The toughness of beams or struts can be increased through the addition of architectural and multi-material features without reducing stiffness and strength.*

Hypothesis H_1 is verified with Chapters 3, 4, and 5, each of which show that the improvement of the (micro-)structure through architectural or multi-material features can significantly

increase the toughness of individual beams or struts under bending. Specifically, the conventional, single-material struts are replaced with multi-material core-shell struts of three types. Core-shell type I replaces the inner part of the struts with a more brittle material of less failure strain. As the inner parts of the struts are strained less than the outer parts, this does not change the effective failure strain, but significantly increases the fracture toughness. Core-shell type II replaces the inner part of the struts with a more flexible material that is able to continue absorbing energy upon fracture of the shell. Core-shell type III adds interfaces between brittle material layers, which allows each layer to fail when its own failure strain is reached, rather than when the failure strain of the outermost layer is reached.

> **Hypothesis H_2:** *The toughness of cellular structures can be increased by increasing the toughness of their struts.*

In Chapter 3, the improved core-shell type I struts are implemented in a Voronoi unit cell and tested in a 3x3x3 lattice structure. Chapter 4 tests woodpile structures fabricated from improved core-shell type II struts. Both lattice types show a significant increase in toughness when compared to their conventional counterparts, verifying Hypothesis H_2.

In combination, the validation of Hypothesis H_1 and Hypothesis H_2 answers the research question. The toughness of cellular lightweight structures can be increased by changing the (micro-)structure of the struts. In particular, architectural features in the form of intersections are introduced, which prevent cracks from propagating (core-shell type II and III). Further, the material distribution in the struts is optimized for maximum energy absorption by replacing parts of the struts with more flexible (core-shell type II) or more brittle materials (core-shell type I). The addition of these features does not or only marginally decrease, and in some cases significantly increase the stiffness and strength of the struts and lattices.

Linking back to the expected contributions in Section 1.2.4, the main contributions and findings of this work are summarized as follows. A more detailed overview can be found in each of the respective chapters.

1. An in-depth analysis of interfaces and material mixing in the material jetting and direct ink writing processes. For material jetting, interfaces between similar and dissimilar materials, as well as the multi-material mixing process have been investigated. In direct ink writing, the analysis of interfaces between different materials revealed that diffusion

affects the boundary region and that diffusion can be prevented by adding a thin interfacial layer. Besides informing the next steps in this work, these findings will be a valuable source for everyone fabricating structural multi-material parts using these processes.

2. The design and development of a novel printhead that allows extrusion of multi-material, multicore-shell filaments, where the number of layers does not affect the minimum filament diameter. The versatile printhead can extrude filaments with different core-to-shell ratios and change these ratios on the fly while printing. Aside from enabling the fabrication, hence validation of core-shell type II, these nozzles are already used with minor adjustments in multiple research projects, for example, to fabricate ceramic core-shell foams [64], cell-laden core-shell tissue-constructs [243], and hollow spheres for high-throughput printing of open- and closed-cell foams [244].

3. The introduction of three size independent and generally applicable architectural paradigms for lattice struts and beams in a more general sense. When compared to the best conventional (single-material) option the paradigms can significantly

   a) increase stiffness, strength, and toughness before failure occurs (core-shell type I).

   b) increase failure strain and toughness after rupture, while only marginally decreasing the stiffness and strength (core-shell type II).

   c) increase failure strain and toughness after rupture without decreasing stiffness and strength (core-shell type III).

   In addition, a design framework is presented that allows users to quickly identify the appropriate core-shell type for their application. These architectural paradigms present a major leap towards the application of high-performance structures in actual products and are expected to significantly contribute to the field of structural engineering in a broad sense.

4. The discovery of a material and geometry combination that enhances the toughness and strength in lattice struts beyond what is introduced by the architectural principles only.

7.2 CHALLENGES AND OPPORTUNITIES

Several challenges and opportunities for the core-shell mechanisms are found during the course of the project. Further investigation of the following topics is expected to provide a deeper understanding and likely to enhance the presented findings.

7.2.1 *Nodal effects*

Independent of whether conventional or core-shell struts are used, nodes are critical features of lattice structures that substantially affect the global properties. Specifically, in bending dominated unit cell architectures, the nodes often act as stress concentrations that initiate failure [245, 246].

When designing lattices with core-shell struts, one can either leave the nodes as they are, i.e. only replace the struts, or take into account the strut composition in the nodal design. Resultingly, the core-shell struts provide the potential for further improvement, but not negatively affect the mechanical performance of a lattice.

7.2.2 *Increasing the material space*

The core-shell struts consist of carrying layers and interfacial layers, each of which has specific requirements on the material properties.

CARRYING LAYER Current limitations in fabrication techniques have not yet allowed expansion of the presented, architectural principles to all material classes and combinations. While this is not necessary to prove the concepts, it would enable maximization of the properties in an absolute manner. Enabling technologies are in development and soon expected to be able to process arbitrary materials into arbitrary shapes. With this, even higher properties than the ones presented can be achieved, likely filling empty areas on the Ashby plot (Figure 6.3). In particular, technical ceramics are a promising class, as they provide enormous strength with relatively little toughness. It has been shown recently that ceramics can be 3D printed

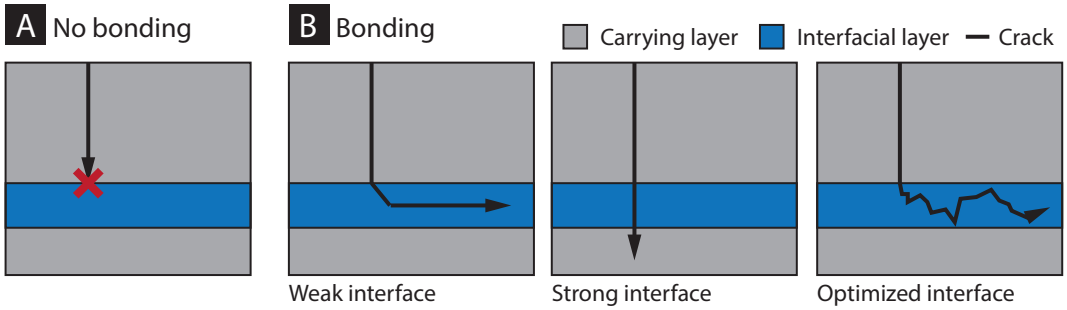

FIGURE 7.1: Interfacial layer options. (a) An interfacial layer material that does not bond to either material can stop a crack from propagating through the layers. (b) If the interfacial material bonds, two scenarios exist. When the material is weak, the crack propagates through the interfacial layer with ease, but does not propagate into other carrying layers. If the material is strong, it can transfer the crack through the layers. An optimum needs to be found that does not transfer the crack, but resists its propagation.

into complex structures with outstanding, mechanical properties [64, 197]. Applying, for example, core-shell type III, would not reduce the stiffness or strength of these structures, but greatly increase the toughness (Figure 6.3).

INTERFACIAL LAYER The exact role of the interfacial layer depends on the core-shell type, dimensions, and other parameters. In core-shell type II, a silicone material is used to separate the uncured layers during the curing process. In type III, the interfacial layers are formed with air, i.e. no material between the (cured) layers. The interfacial layer materials can be further optimized and there are two approaches.

Approach one partially or completely prevents bonding with either of the neighboring layers. This is sufficient to prevent cracks from propagating and creating stress concentrations (Figure 7.1a). Hence, the material can be tuned to similar properties as the other layers, e.g. stiff and strong, which minimizes or eliminates the weakening effect. However, finding such materials has proven to be extremely difficult as not only the mechanical, but also the processing parameters are important. For example, polytetrafluoroethylene (PTFE, commonly referred to as Teflon) requires a completely different process and processing parameters than those used for epoxy.

Approach two allows bonding (Figure 7.1b). Here, it can be distinguished between two extremes. If the interface properties are much weaker than those of the carrying layers, the crack will only propagate within the gap material and not be transferred (left). If the interfacial layer material properties are identical to those of the carrying layers, the crack will propagate

through the layers, not distinguishing between interfacial and carrying layer (center). The difficulty consists in finding the fine line between the two cases. A material is required that is just about weak enough to not transfer cracks between layers, but strong enough to substantially hinder the crack from propagating within the interfacial layer (right).

Depending on the process, additional requirements on the interfacial layer apply, such as preventing diffusion between the different material layers. As the interfacial layers in this work are designed to be as small as possible to minimize the weakening effect, a change in the interfacial layer material is not expected to significantly change the outcome in absolute terms. However, it shows that further investigation and, in particular, progress in technology can achieve even better properties than the ones reported.

7.2.3 *Interactions between struts, unit cells, and lattices*

Strong interaction effects between the strut, unit cell, and lattice levels are expected, and can be exploited to improve the properties of the overall system further.

STRUT-LATTICE INTERACTION For example, if a product requires a defined stiffness with a specific energy absorption, conventionally, a combination of unit cell and material is selected that provides these properties. The approach presented herein can significantly increase both the stiffness and energy absorption of the system, without adding weight. Consequently, the safety factors are much larger than required, which allows the designer to reduce the build volume, weight, or relative density of the structure. In another example, a designer might have a given volume with the task to maximize the energy absorption within this volume. Traditionally, the designer would select a combination of unit cell and material that provides the best trade-off among stiffness, strength, and fracture strain. With the presented approach either or all of these properties increase, adding significant energy absorption to the system. In addition, the increased fracture strain would allow the designer to select a more stretching dominated unit cell that adds even more energy absorption to the system.

STRUT-UNIT CELL AND UNIT CELL-LATTICE INTERACTION Besides using one strut type for the whole lattice, they can be individually adjusted. This is particularly effective for defined load cases, such as helmets, where the impact occurs always orthogonally to the surface. This allows the unit cell to be composed of multiple different strut types or configurations, each optimized for the local load case. Similarly, the unit cell type can be locally fitted to the global load case of the structure, which might prioritize high stiffness in one part and high energy absorption in another. Simply replacing conventional struts with (different) optimized struts will alter the global response of the structure. This needs to be taken into account, especially if a) the requirements are more complex than simply maximizing the energy absorption, and b) the real optimum needs to be found.

VARYING PROPERTIES ALONG THE STRUT In Chapter 3 it has been shown that the composition of the strut can be changed on the fly, i.e. along the longitudinal direction of the struts. This is also the case for the other core-shell types and can increase the complexity, but also performance, of the system even further. In particular, the aforementioned nodes are critical and can significantly affect the behavior of a lattice structure, especially when it is a mechanism that only gains stiffness with fixed nodes [68]. Making use of gradient struts allows tailoring of the nodal behavior locally and globally, for example, by making the struts stiffer and stronger near the nodes.

7.2.4 *Moving beyond mechanical properties*

Core-shell architectures are not new and have been used in a variety of applications, such as 3D printed strain sensors [204, 235] and vascular networks [247, 248]. In this work, only structural materials have been considered. However, the versatility of the proposed printhead design offers great potential for numerous additions and applications. In particular, functional materials are of interest, which can be implemented into mechanical structures. Examples include conductive materials for sensing, shape-memory materials for actuation, and uncured materials for self-healing.

7.3 SUMMARY AND CONCLUSIONS

Although the quest for stiffer and stronger materials continues, these materials have little to no use as structural materials without appropriate fracture resistance. The attainment of toughness is, therefore, a vital requirement for most structural materials. Unfortunately, these properties are typically mutually exclusive. It is the materials with lower strength and, hence, higher toughness that are used in most safety-critical applications, where a premature or catastrophic fracture is unacceptable. For these reasons, the development of stiff, strong and tough materials has traditionally been an exercise in compromise.

The work presented herein has shown that the general rule of mutual exclusivity among stiffness, strength, and toughness can be overcome. In some cases, the achieved toughness even exceeds the toughness of the base materials used, a phenomenon rarely found in nature. This is enabled by the introduction of features that fully utilize the processed material or hinder crack propagation.

As opposed to existing approaches, the presented principles are tailored to lattice structures, adding a lightweight aspect to the system – another property that is typically mutually exclusive with most mechanical properties. However, the principles can also be applied to structures other than lattice structures where crack propagation is a problem, or where volumes of identical materials are unequally strained.

The presented principles are independent of scale and material. This makes them widely applicable and highly complementary to existing approaches. For example, lattices fabricated from highly optimized, fiber-reinforced plastics can be equipped with the mechanisms to form synergy effects.

Of course, there are also limitations, mostly dictated by current fabrication constraints. While some of them have been overcome in the course of this work, continuing advancements in technology are expected to make the structures available to a wide audience in the near future.

In conclusion, the work presents a major step towards the applicability of stiff, strong, and tough lightweight structures and has the potential to revolutionize the field, not only in an academic, but also industrial and consumer setting.

BIBLIOGRAPHY

1. Hibbeler, R. C. *Mechanics of materials* Ninth edition, xvii, 879 pages (Prentice Hall, Boston, 2014).
2. Boresi, A. P., Schmidt, R. J. & Sidebottom, O. M. *Advanced mechanics of materials* (Wiley New York, 1993).
3. Ashby, M. F. & Cebon, D. Materials selection in mechanical design. *Le Journal de Physique IV* **3** (1993).
4. Rosler, J., Harders, H. & Baker, M. *Mechanical behaviour of engineering materials* 2007.
5. Blackman, B., Kinloch, A., Lee, J. S., Taylor, A., Agarwal, R., Schueneman, G. & Sprenger, S. The fracture and fatigue behaviour of nano-modified epoxy polymers. *Journal of Materials Science* **42**, 7049 (2007).
6. Bouville, F., Maire, E., Meille, S., Van de Moortele, B., Stevenson, A. J. & Deville, S. Strong, tough and stiff bioinspired ceramics from brittle constituents. *Nature materials* **13**, 508 (2014).
7. Pippan, R. & Hohenwarter, A. The importance of fracture toughness in ultrafine and nanocrystalline bulk materials. *Materials research letters* **4**, 127 (2016).
8. Lu, G. & Yu, T. *Energy absorption of structures and materials* (Elsevier, 2003).
9. Bonderer, L. J., Studart, A. R. & Gauckler, L. J. Bioinspired design and assembly of platelet reinforced polymer films. *Science* **319**, 1069 (2008).
10. Wegst, U. G., Bai, H., Saiz, E., Tomsia, A. P. & Ritchie, R. O. Bioinspired structural materials. *Nature materials* **14**, 23 (2015).
11. Zou, Y., Ma, H. & Spolenak, R. Ultrastrong ductile and stable high-entropy alloys at small scales. *Nature communications* **6** (2015).
12. Ritchie, R. O. The conflicts between strength and toughness. *Nature materials* **10**, 817 (2011).

13. Munch, E., Launey, M. E., Alsem, D. H., Saiz, E., Tomsia, A. P. & Ritchie, R. O. Tough, bio-inspired hybrid materials. *Science* **322**, 1516 (2008).

14. Launey, M. E., Buehler, M. J. & Ritchie, R. O. On the mechanistic origins of toughness in bone. *Annual review of materials research* **40**, 25 (2010).

15. Barthelat, F. & Mirkhalaf, M. The quest for stiff, strong and tough hybrid materials: an exhaustive exploration. *Journal of The Royal Society Interface* **10**, 20130711 (2013).

16. Wei, Y., Li, Y., Zhu, L., Liu, Y., Lei, X., Wang, G., Wu, Y., Mi, Z., Liu, J., Wang, H., *et al.* Evading the strength–ductility trade-off dilemma in steel through gradient hierarchical nanotwins. *Nature communications* **5** (2014).

17. Li, Z., Pradeep, K. G., Deng, Y., Raabe, D. & Tasan, C. C. Metastable high-entropy dual-phase alloys overcome the strength–ductility trade-off. *Nature* **534**, 227 (2016).

18. Wang, Y. M., Voisin, T., McKeown, J. T., Ye, J., Calta, N. P., Li, Z., Zeng, Z., Zhang, Y., Chen, W., Roehling, T. T., *et al.* Additively manufactured hierarchical stainless steels with high strength and ductility. *Nature Materials* (2017).

19. Ramberg, W. & Osgood, W. R. Description of stress-strain curves by three parameters (1943).

20. Ritchie, R. O., Knott, J. F. & Rice, J. On the relationship between critical tensile stress and fracture toughness in mild steel. *Journal of the Mechanics and Physics of Solids* **21**, 395 (1973).

21. Larson, B. *NDT Education Resource Center* `https://www.nde-ed.org/EducationResources/CommunityCollege/Materials/Mechanical/Toughness.htm` (2017).

22. Studart, A. R. Towards high-performance bioinspired composites. *Advanced Materials* **24**, 5024 (2012).

23. Spolenak, R., Gorb, S., Gao, H. & Arzt, E. Effects of contact shape on the scaling of biological attachments. *Proceedings of the Royal Society of London A: Mathematical, Physical and Engineering Sciences* **461**, 305 (2005).

24. Gruber, P. A., Boehm, J., Onuseit, F., Wanner, A., Spolenak, R. & Arzt, E. Size effects on yield strength and strain hardening for ultra-thin Cu films with and without passivation: A study by synchrotron and bulge test techniques. *Acta Materialia* **56**, 2318 (2008).

25. Chai, H., Lee, J. J.-W., Constantino, P. J., Lucas, P. W. & Lawn, B. R. Remarkable resilience of teeth. *Proceedings of the National Academy of Sciences* **106**, 7289 (2009).

26. Studart, A. R., Filser, F., Kocher, P., Lüthy, H. & Gauckler, L. J. Mechanical and fracture behavior of veneer–framework composites for all-ceramic dental bridges. *dental materials* **23**, 115 (2007).

27. Bertram, J. & Gosline, J. Fracture toughness design in horse hoof keratin. *Journal of Experimental Biology* **125**, 29 (1986).

28. Porter, M. M. & McKittrick, J. It's tough to be strong: Advances. *Am. Ceram. Soc. Bull* **93**, 18 (2014).

29. Weaver, J. C., Aizenberg, J., Fantner, G. E., Kisailus, D., Woesz, A., Allen, P., Fields, K., Porter, M. J., Zok, F. W., Hansma, P. K., *et al.* Hierarchical assembly of the siliceous skeletal lattice of the hexactinellid sponge Euplectella aspergillum. *Journal of structural biology* **158**, 93 (2007).

30. Sypeck, D. J. Cellular truss core sandwich structures. *Applied Composite Materials* **12**, 229 (2005).

31. Bonser, R. H. The mechanical properties of feather keratin. *Journal of Zoology* **239**, 477 (1996).

32. Creager, S. B. & Porter, M. E. Stiff and tough: a comparative study on the tensile properties of shark skin. *Zoology* (2017).

33. Vincent, J. F. & Owers, P. Mechanical design of hedgehog spines and porcupine quills. *Journal of Zoology* **210**, 55 (1986).

34. Evans, F. G. *Mechanical properties of bone* **881** (Charles C. Thomas Publisher, 1973).

35. Rho, J.-Y., Kuhn-Spearing, L. & Zioupos, P. Mechanical properties and the hierarchical structure of bone. *Medical engineering & physics* **20**, 92 (1998).

36. Weiner, S. & Wagner, H. D. The material bone: structure-mechanical function relations. *Annual Review of Materials Science* **28**, 271 (1998).

37. Zioupos, P. & Currey, J. Changes in the stiffness, strength, and toughness of human cortical bone with age. *Bone* **22**, 57 (1998).

38. MacGregor, J. G. *Reinforced concrete: Mechanics and design* (1992).

39. Kinloch, A. J. *Fracture behaviour of polymers* (Springer Science & Business Media, 2013).

40. Balaguru, P. N. & Shah, S. P. *Fiber-reinforced cement composites* (1992).

41. Soutis, C. Carbon fiber reinforced plastics in aircraft construction. *Materials Science and Engineering: A* **412**, 171 (2005).

42. Dirk, H.-J. L., Ward, C. & Potter, K. D. The engineering aspects of automated prepreg layup: History, present and future. *Composites Part B: Engineering* **43**, 997 (2012).

43. Askeland, D., Fulay, P. & Wright, W. *The science and engineering of materials* (Nelson Education, 2011).

44. Kamat, S., Su, X., Ballarini, R. & Heuer, A. Structural basis for the fracture toughness of the shell of the conch Strombus gigas. *Nature* **405**, 1036 (2000).

45. Mayer, G. New classes of tough composite materials - Lessons from natural rigid biological systems. *Materials Science and Engineering: C* **26**, 1261 (2006).

46. Barthelat, F. & Espinosa, H. An experimental investigation of deformation and fracture of nacre–mother of pearl. *Experimental mechanics* **47**, 311 (2007).

47. Wang, R., Suo, Z., Evans, A., Yao, N. & Aksay, I. Deformation mechanisms in nacre. *Journal of Materials Research* **16**, 2485 (2001).

48. Wang, R., Wen, H., Cui, F., Zhang, H. & Li, H. Observations of damage morphologies in nacre during deformation and fracture. *Journal of materials science* **30**, 2299 (1995).

49. Deville, S., Saiz, E. & Tomsia, A. P. Freeze casting of hydroxyapatite scaffolds for bone tissue engineering. *Biomaterials* **27**, 5480 (2006).

50. Deville, S., Saiz, E., Nalla, R. K. & Tomsia, A. P. Freezing as a path to build complex composites. *Science* **311**, 515 (2006).

51. Meyers, M. A., McKittrick, J. & Chen, P.-Y. Structural biological materials: critical mechanics-materials connections. *science* **339**, 773 (2013).

52. Jaglinski, T., Kochmann, D., Stone, D. & Lakes, R. Composite materials with viscoelastic stiffness greater than diamond. *Science* **315**, 620 (2007).

53. Marsh, K. & Bugusu, B. Food packaging - roles, materials, and environmental issues. *Journal of food science* **72** (2007).

54. Cole, G. & Sherman, A. Light weight materials for automotive applications. *Materials characterization* **35**, 3 (1995).

55. Katz, J. Aerodynamics of race cars. *Annu. Rev. Fluid Mech.* **38**, 27 (2006).

56. Wegst, U. & Ashby, M. The mechanical efficiency of natural materials. *Philosophical Magazine* **84**, 2167 (2004).

57. Gibson, L. J., Ashby, M. F. & Harley, B. A. *Cellular materials in nature and medicine* (Cambridge University Press, 2010).

58. Röthlisberger, A., Häberli, S., Spolenak, R. & Dunand, D. C. Synthesis, structure and mechanical properties of ice-templated tungsten foams. *Journal of Materials Research* **31**, 753 (2016).

59. Hamm, C. E., Merkel, R., Springer, O., Jurkojc, P., Maier, C., Prechtel, K. & Smetacek, V. Architecture and material properties of diatom shells provide effective mechanical protection. *Nature* **421**, 841 (2003).

60. Ashby, M. The properties of foams and lattices. *Philosophical Transactions of the Royal Society of London A: Mathematical, Physical and Engineering Sciences* **364**, 15 (2006).

61. Mills, N. *Polymer foams handbook: engineering and biomechanics applications and design guide* (Butterworth-Heinemann, 2007).

62. Almirall, A., Larrecq, G., Delgado, J., Martınez, S., Planell, J. & Ginebra, M. Fabrication of low temperature macroporous hydroxyapatite scaffolds by foaming and hydrolysis of an α-TCP paste. *Biomaterials* **25**, 3671 (2004).

63. Kim, H.-W., Lee, S.-Y., Bae, C.-J., Noh, Y.-J., Kim, H.-E., Kim, H.-M. & Ko, J. S. Porous ZrO 2 bone scaffold coated with hydroxyapatite with fluorapatite intermediate layer. *Biomaterials* **24**, 3277 (2003).

64. Muth, J. T., Dixon, P. G., Woish, L., Gibson, L. J. & Lewis, J. A. Architected cellular ceramics with tailored stiffness via direct foam writing. *Proceedings of the National Academy of Sciences*, 201616769 (2017).

65. Glicksman, L. R. & Torpey, M. Factors governing heat transfer through closed cell foam insulation. *Journal of Thermal Insulation* **12**, 257 (1989).

66. Taslicukur, Z., Balaban, C. & Kuskonmaz, N. Production of ceramic foam filters for molten metal filtration using expanded polystyrene. *Journal of the European Ceramic Society* **27**, 637 (2007).

67. Egan, P. F., Gonella, V. C., Engensperger, M., Ferguson, S. J. & Shea, K. Computationally designed lattices with tuned properties for tissue engineering using 3D printing. *PloS one* **12**, e0182902 (2017).

68. Deshpande, V., Ashby, M. & Fleck, N. Foam topology: bending versus stretching dominated architectures. *Acta Materialia* **49**, 1035 (2001).

69. Pellegrino, S. & Calladine, C. R. Matrix analysis of statically and kinematically indeterminate frameworks. *International Journal of Solids and Structures* **22**, 409 (1986).

70. Deshpande, V. S., Fleck, N. A. & Ashby, M. F. Effective properties of the octet-truss lattice material. *Journal of the Mechanics and Physics of Solids* **49**, 1747 (2001).

71. Desmoulins, A., Zelhofer, A. J. & Kochmann, D. M. Auxeticity in truss networks and the role of bending versus stretching deformation. *Smart Materials and Structures* **25**, 054003 (2016).

72. Schaedler, T. A., Jacobsen, A. J., Torrents, A., Sorensen, A. E., Lian, J., Greer, J. R., Valdevit, L. & Carter, W. B. Ultralight metallic microlattices. *Science* **334**, 962 (2011).

73. Greer, J. R. Materials by design: using architecture and nanomaterial size effects to attain unexplored properties. *Bridge* **45**, 37 (2015).

74. Maggi, A., Li, H. & Greer, J. R. Three-dimensional nano-architected scaffolds with tunable stiffness for efficient bone tissue growth. *Acta biomaterialia* **63**, 294 (2017).

75. Kochmann, D. M. & Bertoldi, K. Exploiting Microstructural Instabilities in Solids and Structures: From Metamaterials to Structural Transitions. *Applied Mechanics Reviews* **69**, 050801 (2017).

76. Masuda, H. & Fukuda, K. Ordered metal nanohole arrays made by a two-step replication of honeycomb structures of anodic alumina. *science* **268**, 1466 (1995).

77. Gibson, L. J. & Ashby, M. F. *Cellular solids: structure and properties* (Cambridge university press, 1999).

78. Vaezi, M., Seitz, H. & Yang, S. A review on 3D micro-additive manufacturing technologies. *The International Journal of Advanced Manufacturing Technology* **67**, 1721 (2013).

79. Sachs, E., Cima, M. & Cornie, J. Three-dimensional printing: rapid tooling and prototypes directly from a CAD model. *CIRP Annals-Manufacturing Technology* **39**, 201 (1990).

80. Agarwala, M., Bourell, D., Beaman, J., Marcus, H. & Barlow, J. Direct selective laser sintering of metals. *Rapid Prototyping Journal* **1**, 26 (1995).

81. Gibson, I., Rosen, D. W. & Stucker, B. *Additive manufacturing technologies* (Springer, 2010).

82. Crump, S. *Fused deposition modeling (FDM): putting rapid back in prototyping* in *Proc. 2nd Int. Conf. on Rapid Prototyping* (1991), 358.

83. Lewis, J. A. Direct ink writing of 3D functional materials. *Advanced Functional Materials* **16**, 2193 (2006).

84. Lewis, J. A., Smay, J. E., Stuecker, J. & Cesarano, J. Direct ink writing of three-dimensional ceramic structures. *Journal of the American Ceramic Society* **89**, 3599 (2006).

85. Abernathy, R., Babiarz, A. J., Barendt, N. A., Ciardella, R., Cooper Jr, J. E., Espenschied, K. S., Fiske, E., Giusti, C. L., Jenkins, P. R., Lewis, A., *et al. Viscous material noncontact jetting system* US Patent 8,257,779. 2012.

86. Jacobs, P. F. *Rapid prototyping & manufacturing: fundamentals of stereolithography* (Society of Manufacturing Engineers, 1992).

87. Maruo, S., Nakamura, O. & Kawata, S. Three-dimensional microfabrication with two-photon-absorbed photopolymerization. *Optics letters* **22**, 132 (1997).

88. Skylar-Scott, M. A., Liu, M.-C., Wu, Y., Dixit, A. & Yanik, M. F. Guided Homing of Cells in Multi-Photon Microfabricated Bioscaffolds. *Advanced healthcare materials* **5**, 1233 (2016).

89. Lombardi, J. L., Popovich, D. & Artz, G. J. *Water soluble rapid prototyping support and mold material* US Patent 6,070,107. 2000.

90. Priedeman Jr, W. R. & Brosch, A. L. *Soluble material and process for three-dimensional modeling* US Patent 6,790,403. 2004.

91. Skylar-Scott, M. A., Gunasekaran, S. & Lewis, J. A. Laser-assisted direct ink writing of planar and 3D metal architectures. *Proceedings of the National Academy of Sciences* **113**, 6137 (2016).

92. Eichenhofer, M., Wong, J. C. & Ermanni, P. Continuous lattice fabrication of ultra-lightweight composite structures. *Additive Manufacturing* **18**, 48 (2017).

93. Dilworth, P. & Bogue, M. *Hand-held three-dimensional drawing device* US Patent 9,102,098. 2015.

94. Frazier, W. E. Metal additive manufacturing: a review. *Journal of Materials Engineering and Performance* **23**, 1917 (2014).

95. Kruth, J.-P., Leu, M.-C. & Nakagawa, T. Progress in additive manufacturing and rapid prototyping. *CIRP Annals-Manufacturing Technology* **47**, 525 (1998).

96. Mueller, J. & Shea, K. *The Effect of Build Orientation on the Mechanical Properties in Inkjet 3D Printing* in *International Solid Freeform Fabrication (SFF) Symposium* (2015), 983.

97. Mueller, J., Shea, K. & Daraio, C. Mechanical properties of parts fabricated with inkjet 3D printing through efficient experimental design. *Materials & Design* **86**, 902 (2015).

98. Mueller, J., Kim, S. E., Shea, K. & Daraio, C. *Tensile Properties of Inkjet 3D Printed Parts: Critical Process Parameters and Their Efficient Analysis* in *Proceedings of the ASME 2015 International Design Engineering Technical Conferences and Computers and Information in Engineering Conference* (2015), 1.

99. Kruth, J.-P., Wang, X., Laoui, T. & Froyen, L. Lasers and materials in selective laser sintering. *Assembly Automation* **23**, 357 (2003).

100. Beaman, J. J. & Deckard, C. R. *Selective laser sintering with assisted powder handling* US Patent 4,938,816. 1990.

101. Japson, L. *Intial development of a multi-material selective laser sintering process (M^ 2SLS)* in *Proc. 8th Europ. Conf. on RPM* (1999), 367.

102. Cumpston, B. H., Ananthavel, S. P., Barlow, S., Dyer, D. L., Ehrlich, J. E., Erskine, L. L., Heikal, A. A., Kuebler, S. M., Lee, I.-Y. S., McCord-Maughon, D., *et al.* Two-photon polymerization initiators for three-dimensional optical data storage and microfabrication. *Nature* **398**, 51 (1999).

103. Lim, S., Buswell, R. A., Le, T. T., Austin, S. A., Gibb, A. G. & Thorpe, T. Developments in construction-scale additive manufacturing processes. *Automation in construction* **21**, 262 (2012).

104. Zheng, X., Smith, W., Jackson, J., Moran, B., Cui, H., Chen, D., Ye, J., Fang, N., Rodriguez, N., Weisgraber, T. & Spadaccini, C. Multiscale metallic metamaterials. *Nature Materials* (2016).

105. Hansen, C. J., Saksena, R., Kolesky, D. B., Vericella, J. J., Kranz, S. J., Muldowney, G. P., Christensen, K. T. & Lewis, J. A. High Throughput Printing via Microvascular Multinozzle Arrays. *Advanced Materials* **25**, 96 (2013).

106. Hirt, L., Reiser, A., Spolenak, R. & Zambelli, T. Additive manufacturing of metal structures at the micrometer scale. *Advanced Materials* **29** (2017).

107. Wohlers, T. *Wohlers report 2016* (Wohlers Associates, Inc, 2016).

108. Meza, L. R., Phlipot, G. P., Portela, C. M., Maggi, A., Montemayor, L. C., Comella, A., Kochmann, D. M. & Greer, J. R. Reexamining the mechanical property space of three-dimensional lattice architectures. *Acta Materialia* **140**, 424 (2017).

109. Jang, D., Meza, L. R., Greer, F. & Greer, J. R. Fabrication and deformation of three-dimensional hollow ceramic nanostructures. *Nature materials* **12**, 893 (2013).

110. Meza, L. R. & Greer, J. R. Mechanical characterization of hollow ceramic nanolattices. *Journal of Materials Science* **49**, 2496 (2014).

111. Zheng, X., Lee, H., Weisgraber, T. H., Shusteff, M., DeOtte, J., Duoss, E. B., Kuntz, J. D., Biener, M. M., Ge, Q., Jackson, J. A., Kucheyev, S. O., Fang, N. X. & Spadaccini, C. M. Ultralight, ultrastiff mechanical metamaterials. *Science* **344**, 1373 (2014).

112. Bauer, J., Hengsbach, S., Tesari, I., Schwaiger, R. & Kraft, O. High-strength cellular ceramic composites with 3D microarchitecture. *Proceedings of the National Academy of Sciences* **111**, 2453 (2014).

113. Meza, L. R., Das, S. & Greer, J. R. Strong, lightweight, and recoverable three-dimensional ceramic nanolattices. *Science* **345**, 1322 (2014).

114. Greer, J. R. & De Hosson, J. T. M. Plasticity in small-sized metallic systems: Intrinsic versus extrinsic size effect. *Progress in Materials Science* **56**, 654 (2011).

115. Gu, X. W., Wu, Z., Zhang, Y.-W., Srolovitz, D. J. & Greer, J. R. Microstructure versus flaw: mechanisms of failure and strength in nanostructures. *Nano letters* **13**, 5703 (2013).

116. Chen, D., Jang, D., Guan, K., An, Q., Goddard III, W. & Greer, J. Nanometallic glasses: size reduction brings ductility, surface state drives its extent. *Nano letters* **13**, 4462 (2013).

117. Rys, J., Valdevit, L., Schaedler, T. A., Jacobsen, A. J., Carter, W. B. & Greer, J. R. Fabrication and Deformation of Metallic Glass Micro-Lattices. *Advanced Engineering Materials* **16**, 889 (2014).

118. Hofmann, D. C., Suh, J.-Y., Wiest, A., Duan, G., Lind, M.-L., Demetriou, M. D. & Johnson, W. L. Designing metallic glass matrix composites with high toughness and tensile ductility. *Nature* **451**, 1085 (2008).

119. Evans, A. G. Perspective on the development of high-toughness ceramics. *Journal of the American Ceramic society* **73**, 187 (1990).

120. Compton, B. G. & Lewis, J. A. 3D printing of lightweight cellular composites. *Advanced Materials* **26**, 5930 (2014).

121. Sun, J. & Bhushan, B. Hierarchical structure and mechanical properties of nacre: a review. *Rsc Advances* **2**, 7617 (2012).

122. Mohsenizadeh, M., Gasbarri, F., Munther, M., Beheshti, A. & Davami, K. Additively-manufactured lightweight Metamaterials for energy absorption. *Materials & Design* **139**, 521 (2018).

123. Ha, C. S., Lakes, R. S. & Plesha, M. E. Design, Fabrication, and Analysis of Lattice Exhibiting Energy Absorption via Snap-through Behavior. *Materials & Design* (2018).

124. Libanori, R., Erb, R. M., Reiser, A., Le Ferrand, H., Süess, M. J., Spolenak, R. & Studart, A. R. Stretchable heterogeneous composites with extreme mechanical gradients. *Nature communications* **3**, 1265 (2012).

125. Kandemir, A. C., Ramakrishna, S. N., Erdem, D., Courty, D. & Spolenak, R. Gradient nanocomposite printing by dip pen nanolithography. *Composites Science and Technology* **138**, 186 (2017).

126. Wegst, U. G. Bending efficiency through property gradients in bamboo, palm, and wood-based composites. *Journal of the mechanical behavior of biomedical materials* **4**, 744 (2011).

127. Kumar, S. & de Tejada Alvarez, A. *Modeling and Experimental Evaluation of Geometrically Graded Multi-Material Single-Lap Joints* in *56th AIAA/ASCE/AHS/ASC Structures, Structural Dynamics, and Materials Conference* (2015), 1885.

128. Tilbrook, M., Rutgers, L., Moon, R. J. & Hoffman, M. *Fracture and fatigue crack propagation in graded composites* in *Materials Science Forum* **492** (Trans Tech Publ), 573.

129. Hardin, J. O., Ober, T. J., Valentine, A. D. & Lewis, J. A. Microfluidic printheads for multimaterial 3D printing of viscoelastic inks. *Advanced materials* **27**, 3279 (2015).

130. Calvert, P. Inkjet printing for materials and devices. *Chemistry of materials* **13**, 3299 (2001).

131. Stratasys Ltd. *Stratasys 3D Printing and Additive Manufacturing* http://www.stratasys.com (2016).

132. Barclift, M. W. & Williams, C. B. *Examining variability in the mechanical properties of parts manufactured via polyjet direct 3D printing* in *International Solid Freeform Fabrication Symposium, August* (2012), 6.

133. Cazon, A., Morer, P. & Matey, L. PolyJet technology for product prototyping: Tensile strength and surface roughness properties. *Proceedings of the Institution of Mechanical Engineers, Part B: Journal of Engineering Manufacture* **228**, 1664 (2014).

134. Kesy, A. & Kotlinski, J. Mechanical properties of parts produced by using polymer jetting technology. *Archives of civil and mechanical engineering* **10**, 37 (2010).

135. Stankovic, T., Mueller, J., Egan, P. & Shea, K. A Generalized Optimality Criteria Method for Optimization of Additively Manufactured Multimaterial Lattice Structures. *Journal of Mechanical Design* **137**, 111405 (2015).

136. Rozvany, G. I. *Structural design via optimality criteria: the Prager approach to structural optimization* (Springer Science & Business Media, 2012).

137. Stankovic, T., Mueller, J. & Shea, K. *Optimization for Anisotropy in Additively Manufactured Lattice Structures* in *ASME Computers and Information in Engineering Conference* (ASME).

138. Bass, L. B., Meisel, M. & Williams, C. B. *Exploring Variability in Material Properties of Multi-Material Jetting Parts* in *Proceedings of the 26th Annual International Solid Freeform Fabrication (SFF) Symposium, Austin, Texas, USA* (2016), 993.

139. Bass, L., Bass, L., Meisel, N. A., Meisel, N. A., Williams, C. B. & Williams, C. B. Exploring variability of orientation and aging effects in material properties of multi-material jetting parts. *Rapid Prototyping Journal* **22**, 826 (2016).

140. Vu, I., Bass, L. B., Meisel, M. & Williams, C. B. *Characterization of Multi-Material Interfaces in PolyJet Additive Manufacturing* in *Proceedings of the 26th Annual International Solid Freeform Fabrication (SFF) Symposium, Austin, Texas, USA* (2015), 959.

141. Lin, E., Li, Y., Ortiz, C. & Boyce, M. C. 3D printed, bio-inspired prototypes and analytical models for structured suture interfaces with geometrically-tuned deformation and failure behavior. *Journal of the Mechanics and Physics of Solids* **73**, 166 (2014).

142. Moore, J. P. & Williams, C. B. *Fatigue characterization of 3D printed elastomer material* in *19th Annual International Solid Freeform Fabrication Symposium, Austin, TX* (2012), 641.

143. Oliver, W. C. & Pharr, G. M. An improved technique for determining hardness and elastic modulus using load and displacement sensing indentation experiments. *Journal of materials research* **7**, 1564 (1992).

144. Kruth, J.-P., Mercelis, P., Van Vaerenbergh, J., Froyen, L. & Rombouts, M. Binding mechanisms in selective laser sintering and selective laser melting. *Rapid prototyping journal* **11**, 26 (2005).

145. Jones, R. M. *Mechanics of composite materials* (McGraw-Hill New York, 1975).

146. Mallick, P. K. *Fiber-reinforced composites: materials, manufacturing, and design* (CRC press, 2007).

147. Libonati, F., Gu, G. X., Qin, Z., Vergani, L. & Buehler, M. J. Bone-Inspired Materials by Design: Toughness Amplification Observed Using 3D Printing and Testing. *Advanced Engineering Materials* (2016).

148. Gao, H., Ji, B., Jaeger, I. L., Arzt, E. & Fratzl, P. Materials become insensitive to flaws at nanoscale: lessons from nature. *Proceedings of the national Academy of Sciences* **100**, 5597 (2003).

149. Stankovic, T., Mueller, J. & Shea, K. The Effect of Anisotropy on the Optimization of Additively Manufactured Lattice Structures. *Additive Manufacturing* (2017).

150. Lumpe, T., Mueller, J. & Shea, K. Tensile Strength of Multi-Material Interfaces in 3D Printed Parts (in preparation).

151. Evans, A. G., He, M., Deshpande, V. S., Hutchinson, J. W., Jacobsen, A. J. & Carter, W. B. Concepts for enhanced energy absorption using hollow micro-lattices. *International Journal of Impact Engineering* **37**, 947 (2010).

152. Hammetter, C. I., Rinaldi, R. G. & Zok, F. W. Pyramidal lattice structures for high strength and energy absorption. *Journal of Applied Mechanics* **80**, 041015 (2013).

153. Rosen, D. W. Computer-aided design for additive manufacturing of cellular structures. *Computer-Aided Design and Applications* **4**, 585 (2007).

154. Chu, J., Engelbrecht, S., Graf, G. & Rosen, D. W. A comparison of synthesis methods for cellular structures with application to additive manufacturing. *Rapid Prototyping Journal* **16**, 275 (2010).

155. Ajdari, A., Nayeb-Hashemi, H. & Vaziri, A. Dynamic crushing and energy absorption of regular, irregular and functionally graded cellular structures. *International Journal of Solids and Structures* **48**, 506 (2011).

156. Evans, A. G., Hutchinson, J. W., Fleck, N. A., Ashby, M. & Wadley, H. The topological design of multifunctional cellular metals. *Progress in Materials Science* **46**, 309 (2001).

157. Dias da Silva, V. *Mechanics and strength of materials* Online (Springer, Berlin, 2006).

158. Mueller, J. & Shea, K. Multi-Material Multicore-Shell Struts for Maximized Energy Absorption in Cellular Lightweight Structures (under review).

159. Liu, Y., Schaedler, T. A., Jacobsen, A. J. & Chen, X. Quasi-static energy absorption of hollow microlattice structures. *Composites Part B: Engineering* **67**, 39 (2014).

160. Montemayor, L. & Greer, J. Mechanical Response of Hollow Metallic Nanolattices: Combining Structural and Material Size Effects. *Journal of Applied Mechanics* **82**, 071012 (2015).

161. Queheillalt, D. T. & Wadley, H. N. Pyramidal lattice truss structures with hollow trusses. *Materials Science and Engineering: A* **397**, 132 (2005).

162. Queheillalt, D. T. & Wadley, H. N. Cellular metal lattices with hollow trusses. *Acta Materialia* **53**, 303 (2005).

163. Mueller, J., Raney, J., Kochmann, D. & Shea, K. Multicore-Shell Beams for Stiff and Tough Cellular Structures (under review).

164. Herbert, H. in *Forschungsarbeiten auf dem Gebiete des Ingenieurwesens* 39 (Springer, 1910).

165. Mullin, J. V. & Knoell, A. C. Materials Research and Standards. **10**, 16 (1970).

166. On Mechanical Properties, A. S. D. 1. *Standard test methods for flexural properties of unreinforced and reinforced plastics and electrical insulating materials* in (2007).

167. Zweben, C., Smith, W. & Wardle, M. *Test methods for fiber tensile strength, composite flexural modulus, and properties of fabric-reinforced laminates* in *Composite Materials: Testing and Design (Fifth Conference)* (1979).

168. Fertis, D. G. Basic Theories and Principles of Nonlinear Beam Deformations. *Nonlinear Structural Engineering: With Unique Theories and Methods to Solve Effectively Complex Nonlinear Problems*, 1 (2006).

169. Neal, B. G. *The plastic methods of structural analysis* (Wiley, 1963).

170. Chen, L. An integral approach for large deflection cantilever beams. *International Journal of Non-Linear Mechanics* **45**, 301 (2010).

171. Allen, H. Stiffness and strength of two glass-fiber reinforced cement laminates. *Journal of Composite Materials* **5**, 194 (1971).

172. Aveston, J., Mercer, R. & Sillwood, J. *Composites - Standards, Testing and Design* in *Conference Proceedings, National Physical Laboratory* (1974), 93.

173. Laws, V. Derivation of the tensile stress-strain curve from bending data. *Journal of Materials Science* **16**, 1299 (1981).

174. Mayville, R. & Finnie, I. Uniaxial stress-strain curves from a bending test. *Experimental Mechanics* **22**, 197 (1982).

175. Urriolagoitia-Sosa, G., Durodola, J. & Fellows, N. *Determination of tensile and compressive stress strain curves from bend tests* in *Applied Mechanics and Materials* **1** (2004), 133.

176. Urriolagoitia-Sosa, G., Durodola, J., Lopez-Castro, A. & Fellows, N. A method for the simultaneous derivation of tensile and compressive behaviour of materials under Bauschinger effect using bend tests. *Proceedings of the Institution of Mechanical Engineers, Part C: Journal of Mechanical Engineering Science* **220**, 1509 (2006).

177. Dado, M. & Al-Sadder, S. A new technique for large deflection analysis of non-prismatic cantilever beams. *Mechanics Research Communications* **32**, 692 (2005).

178. Bisshopp, K. & Drucker, D. Large deflection of cantilever beams. *Quarterly of Applied Mathematics* **3**, 272 (1945).

179. Ohtsuki, A. & Ellyin, F. Analytical Approach to Large Deformation Problems of Frame Structures. *JSME International Journal Series A Solid Mechanics and Material Engineering* **44**, 89 (2001).

180. Beléndez, T., Neipp, C. & Beléndez, A. Large and small deflections of a cantilever beam. *European Journal of Physics* **23**, 371 (2002).

181. Ang, M. H., Wei, W. & Teck-Seng, L. *On the estimation of the large deflection of a cantilever beam* in *Industrial Electronics, Control, and Instrumentation, 1993. Proceedings of the IECON'93., International Conference on* (1993), 1604.

182. Magnusson, A., Ristinmaa, M. & Ljung, C. Behaviour of the extensible elastica solution. *International Journal of Solids and Structures* **38**, 8441 (2001).

183. Lee, K. Post-buckling of uniform cantilever column under a combined load. *International Journal of Non-Linear Mechanics* **36**, 813 (2001).

184. Golley, B. The solution of open and closed elasticas using intrinsic coordinate finite elements. *Computer methods in applied mechanics and engineering* **146**, 127 (1997).

185. Kooi, B. & Kuipers, M. A unilateral contact problem with the heavy elastica. *International journal of non-linear mechanics* **19**, 309 (1984).

186. Gere, J. M. & Timoshenko, S. P. *Mechanics of materials PWS* 1990.

187. Feynman, R. P., Leighton, R. B. & Sands, M. *The Feynman Lectures on Physics: Mainly Mechanics, Radiation, and Heat: The Electromagnetic Field. 6. Printing.(Optryk Af 1. Edition 1964)* (Addison-Wesley, 1989).

188. Vu-Khanh, T. & De Charentenay, F. Mechanics and mechanisms of impact fracture in semi-ductile polymers. *Polymer Engineering & Science* **25**, 841 (1985).

189. Watson, D. F. Computing the n-dimensional Delaunay tessellation with application to Voronoi polytopes. *The computer journal* **24**, 167 (1981).

190. Duoss, E. B., Weisgraber, T. H., Hearon, K., Zhu, C., Small, W., Metz, T. R., Vericella, J. J., Barth, H. D., Kuntz, J. D. & Maxwell, R. S. Three dimensional printing of elastomeric, cellular architectures with negative stiffness. *Advanced Functional Materials* **24**, 4905 (2014).

191. Meza, L. R., Zelhofer, A. J., Clarke, N., Mateos, A. J., Kochmann, D. M. & Greer, J. R. Resilient 3D hierarchical architected metamaterials. *Proceedings of the National Academy of Sciences* **112**, 11502 (2015).

192. Truby, R. L. & Lewis, J. A. Printing soft matter in three dimensions. *Nature* **540**, 371 (2016).

193. Fratzl, P., Gupta, H., Paschalis, E. & Roschger, P. Structure and mechanical quality of the collagen-mineral nano-composite in bone. *Journal of materials chemistry* **14**, 2115 (2004).

194. Bendsoe, M. P. & Sigmund, O. *Topology optimization: theory, methods, and applications* (Springer Science & Business Media, 2013).

195. Ashby, M. F., Evans, T., Fleck, N. A., Hutchinson, J., Wadley, H. & Gibson, L. *Metal foams: a design guide* (Elsevier, 2000).

196. Smay, J. E., Cesarano, J. & Lewis, J. A. Colloidal inks for directed assembly of 3-D periodic structures. *Langmuir* **18**, 5429 (2002).

197. Minas, C., Carnelli, D., Tervoort, E. & Studart, A. R. 3D Printing of Emulsions and Foams into Hierarchical Porous Ceramics. *Advanced Materials* **28**, 9993 (2016).

198. O'Masta, M., Dong, L., St-Pierre, L., Wadley, H. & Deshpande, V. The fracture toughness of octet-truss lattices. *Journal of the Mechanics and Physics of Solids* **98**, 271 (2017).

199. Tancogne-Dejean, T., Spierings, A. B. & Mohr, D. Additively-manufactured metallic micro-lattice materials for high specific energy absorption under static and dynamic loading. *Acta Materialia* **116**, 14 (2016).

200. Jackson, A., Vincent, J. & Turner, R. The mechanical design of nacre. *Proceedings of the Royal Society of London B: Biological Sciences* **234**, 415 (1988).

201. Dawson, M. A. & Gibson, L. J. Optimization of cylindrical shells with compliant cores. *International journal of solids and structures* **44**, 1145 (2007).

202. Egan, P. F., Ferguson, S. J. & Shea, K. Design of Hierarchical Three-Dimensional Printed Scaffolds Considering Mechanical and Biological Factors for Bone Tissue Engineering. *Journal of Mechanical Design* **139**, 061401 (2017).

203. Giannakopoulos, G., Masania, K. & Taylor, A. Toughening of epoxy using core-shell particles. *Journal of Materials Science* **46**, 327 (2011).

204. Frutiger, A., Muth, J. T., Vogt, D. M., Menguc, Y., Campo, A., Valentine, A. D., Walsh, C. J. & Lewis, J. A. Capacitive soft strain sensors via multicore-shell fiber printing. *Advanced Materials* **27**, 2440 (2015).

205. Garcia Santamaria, F., Xu, M., Lousse, V., Fan, S., Braun, P. V. & Lewis, J. A. A germanium inverse woodpile structure with a large photonic band gap. *Advanced Materials* **19**, 1567 (2007).

206. Tippur, H. & Rosakis, A. Quasi-static and dynamic crack growth along bimaterial interfaces: a note on crack-tip field measurements using coherent gradient sensing. *Experimental Mechanics* **31**, 243 (1991).

207. Fratzl, P., Gupta, H. S., Fischer, F. D. & Kolednik, O. Hindered crack propagation in materials with periodically varying Young's modulus - lessons from biological materials. *Advanced Materials* **19**, 2657 (2007).

208. Ming-Yuan, H. & Hutchinson, J. W. Crack deflection at an interface between dissimilar elastic materials. *International Journal of Solids and Structures* **25**, 1053 (1989).

209. Faber, K. T. & Evans, A. G. Crack deflection processes - I. Theory. *Acta Metallurgica* **31**, 565 (1983).

210. Faber, K. T. & Evans, A. G. Crack deflection processes - II. Experiment. *Acta Metallurgica* **31**, 577 (1983).

211. Johnsen, B., Kinloch, A., Mohammed, R., Taylor, A. & Sprenger, S. Toughening mechanisms of nanoparticle-modified epoxy polymers. *Polymer* **48**, 530 (2007).

212. Hing, K. A. Bone repair in the twenty-first century: biology, chemistry or engineering? *Philosophical Transactions of the Royal Society of London A: Mathematical, Physical and Engineering Sciences* **362**, 2821 (2004).

213. Meyers, M. A., Chen, P.-Y., Lin, A. Y.-M. & Seki, Y. Biological materials: structure and mechanical properties. *Progress in Materials Science* **53**, 1 (2008).

214. Monn, M. A., Weaver, J. C., Zhang, T., Aizenberg, J. & Kesari, H. New functional insights into the internal architecture of the laminated anchor spicules of Euplectella aspergillum. *Proceedings of the National Academy of Sciences* **112**, 4976 (2015).

215. Kinloch, A. & Taylor, A. Mechanical and fracture properties of epoxy/inorganic micro- and nano-composites. *Journal of Materials Science Letters* **22**, 1439 (2003).

216. Gojny, F., Wichmann, M., Köpke, U., Fiedler, B. & Schulte, K. Carbon nanotube-reinforced epoxy-composites: enhanced stiffness and fracture toughness at low nanotube content. *Composites science and technology* **64**, 2363 (2004).

217. Deville, S. Freeze casting of porous ceramics: a review of current achievements and issues. *Advanced Engineering Materials* **10**, 155 (2008).

218. Kooistra, G. W., Deshpande, V. S. & Wadley, H. N. Compressive behavior of age hardenable tetrahedral lattice truss structures made from aluminium. *Acta Materialia* **52**, 4229 (2004).

219. McKown, S., Shen, Y., Brookes, W., Sutcliffe, C., Cantwell, W., Langdon, G., Nurick, G. & Theobald, M. The quasi-static and blast loading response of lattice structures. *International Journal of Impact Engineering* **35**, 795 (2008).

220. Shen, Y., McKown, S., Tsopanos, S., Sutcliffe, C., Mines, R. & Cantwell, W. The mechanical properties of sandwich structures based on metal lattice architectures. *Journal of Sandwich Structures & Materials* **12**, 159 (2010).

221. Avalle, M., Belingardi, G. & Montanini, R. Characterization of polymeric structural foams under compressive impact loading by means of energy-absorption diagram. *International Journal of Impact Engineering* **25**, 455 (2001).

222. Baumeister, J., Banhart, J. & Weber, M. Aluminium foams for transport industry. *Materials & design* **18**, 217 (1997).

223. Banhart, J. Manufacture, characterisation and application of cellular metals and metal foams. *Progress in materials science* **46**, 559 (2001).

224. Fleck, N., Deshpande, V. & Ashby, M. *Micro-architectured materials: past, present and future* in *Proceedings of the Royal Society of London A: Mathematical, Physical and Engineering Sciences* **466** (The Royal Society), 2495.

225. Ajayan, P. M., Schadler, L. S., Giannaris, C. & Rubio, A. Single-walled carbon nanotube - polymer composites: strength and weakness. *Advanced materials* **12**, 750 (2000).

226. Romijn, N. E. & Fleck, N. A. The fracture toughness of planar lattices: imperfection sensitivity. *Journal of the Mechanics and Physics of Solids* **55**, 2538 (2007).

227. Tankasala, H., Deshpande, V. & Fleck, N. 2013 Koiter Medal Paper: Crack-Tip Fields and Toughness of Two-Dimensional Elastoplastic Lattices. *Journal of Applied Mechanics* **82**, 091004 (2015).

228. Hooke, R. & Jeeves, T. A. "Direct Search" Solution of Numerical and Statistical Problems. *Journal of the ACM (JACM)* **8**, 212 (1961).

229. Amsler & Frey AG. *PMMA XT - Acrylglas extrudiert* `http://shop.amsler-frey.ch/downloads/datenblaetter/td_pmma_xt.pdf` (2016).

230. Archard, J. F. Elastic Deformation and the Laws of Friction. *Proceedings of the Royal Society of London. Series A. Mathematical and Physical Sciences* **243**, 190 (1957).

231. CampusPlastics. *CAMPUS - a material information system for the plastics industry* `http://www.campusplastics.com` (2017).

232. Zhu, C., Han, T. Y.-J., Duoss, E. B., Golobic, A. M., Kuntz, J. D., Spadaccini, C. M. & Worsley, M. A. Highly compressible 3D periodic graphene aerogel microlattices. *Nature communications* **6**, 6962 (2015).

233. Mueller, J. & Shea, K. Buckling, Build orientation, and Scaling Effects in 3D Printed Lattice Structures (under review).

234. Lewis, J. A. Colloidal processing of ceramics. *Journal of the American Ceramic Society* **83**, 2341 (2000).

235. Muth, J. T., Vogt, D. M., Truby, R. L., Menguc, Y., Kolesky, D. B., Wood, R. J. & Lewis, J. A. Embedded 3D printing of strain sensors within highly stretchable elastomers. *Advanced Materials* **26**, 6307 (2014).

236. Ahn, B. Y., Duoss, E. B., Motala, M. J., Guo, X., Park, S.-I., Xiong, Y., Yoon, J., Nuzzo, R. G., Rogers, J. A. & Lewis, J. A. Omnidirectional printing of flexible, stretchable, and spanning silver microelectrodes. *Science* **323**, 1590 (2009).

237. Boley, J. W., Chaudhary, K., Ober, T. J., Khorasaninejad, M., Chen, W. T., Hanson, E., Kulkarni, A., Oh, J., Kim, J., Aagesen, L. K., *et al.* High-Operating-Temperature Direct Ink Writing of Mesoscale Eutectic Architectures. *Advanced Materials* **29** (2017).

238. Wehner, M., Truby, R. L., Fitzgerald, D. J., Mosadegh, B., Whitesides, G. M., Lewis, J. A. & Wood, R. J. An integrated design and fabrication strategy for entirely soft, autonomous robots. *Nature* **536**, 451 (2016).

239. Haghpanah, B., Salari-Sharif, L., Pourrajab, P., Hopkins, J. & Valdevit, L. Multistable Shape-Reconfigurable Architected Materials. *Advanced Materials* **28**, 7915 (2016).

240. Restrepo, D., Mankame, N. D. & Zavattieri, P. D. Phase transforming cellular materials. *Extreme Mechanics Letters* **4**, 52 (2015).

241. Shan, S., Kang, S. H., Raney, J. R., Wang, P., Fang, L., Candido, F., Lewis, J. A. & Bertoldi, K. Multistable architected materials for trapping elastic strain energy. *Advanced Materials* **27**, 4296 (2015).

242. Rafsanjani, A., Akbarzadeh, A. & Pasini, D. Snapping mechanical metamaterials under tension. *Advanced Materials* **27**, 5931 (2015).

243. Kroll, K. et al. TBD (in preparation).

244. Visser, C.W. et al. Locally tailored foams via direct polymer bubble printing (in preparation).

245. La Magna, R., Waimer, F. & Knippers, J. Nature-inspired generation scheme for shell structures (2012).

246. Portela, C., Greer, J. & Kochmann, D. Effects of node geometry on the stiffness scaling of non-slender three-dimensional lattice architectures (in preparation).

247. Jia, W., Gungor-Ozkerim, P. S., Zhang, Y. S., Yue, K., Zhu, K., Liu, W., Pi, Q., Byambaa, B., Dokmeci, M. R., Shin, S. R., *et al.* Direct 3D bioprinting of perfusable vascular constructs using a blend bioink. *Biomaterials* **106**, 58 (2016).

248. Yu, Y., Zhang, Y., Martin, J. A. & Ozbolat, I. T. Evaluation of cell viability and functionality in vessel-like bioprintable cell-laden tubular channels. *Journal of biomechanical engineering* **135**, 091011 (2013).